An Experimental Investigation of Turbulent Flow Characteristics Beneath a Simulated Ice Jam

by

Hoda Pahlavan

A Thesis submitted to the Faculty of Graduate Studies of
The University of Manitoba
in partial fulfillment of the requirements of the degree of

Master of Science

Department of Civil Engineering
University of Manitoba
Winnipeg, Manitoba
Canada

Abstract

Ice jams have caused serious hazards such as floods in northern countries. Despite several studies focused on river ice jams, a lack of research has been identified in the existing literature to analyze impacts of an ice jam on turbulent flow characteristics. Thus, this research attempts to address this knowledge gap. A better comprehension of flow features beneath an ice jam will help river ice engineers to reduce economic, environmental, and ecological damages.

Technical difficulties and safety concerns limit data collection in ice jam field studies. Therefore, a physical model of a river ice jam was constructed in the Hydraulics Research & Testing Facility at the University of Manitoba. Two scenarios were proposed to simulate an ice jam. The first scenario was to use a basic model with constant upstream and downstream water depth. The second scenario was developed as an extension of the first scenario, with a modified setup to allow the upstream water depth to be greater than the downstream water depth. This was done to increase similarity with the real ice jam in nature and improve the results. For the second scenario, different roughness ratios of channel bed to ice jam were defined. Experiments were conducted to quantify the turbulent flow characteristics including streamwise velocity and streamwise turbulence intensity distribution beneath the ice jam. The flow velocities were measured at different locations beneath the ice jam using an acoustic Doppler velocimeter. The turbulence intensities and bed shear stresses were calculated using the measured velocities.

The results indicated that the flow velocity and turbulence intensity were a function of the streamwise location beneath the ice jam as well as the roughness of the bed and ice jam. Significant changes were observed in the velocity and turbulence intensity profiles where the boundaries were fully rough, which could influence an ice jam formation, sediment concentration and water quality, as well as river bed deformation. It is believed that the results from this research will improve our fundamental understanding of flow beneath an ice jam, and can be used for validation of subsequent ice jam numerical models.

Acknowledgments

I would like to take this opportunity to express my sincerest thanks to my supervisor, Dr. Shawn Clark, for his motivation, academic support, and guidance through this work. Without his support, this work would not have been possibly done. It was my honor to conduct research under his supervision which ended to conference papers and presentations. I appreciate Dr. Mark Tachie and Dr. Karen Dow for their valuable comments and guidance.

I would like to express my appreciation to the Natural Science and Engineering Research Council of Canada, Manitoba Hydro, and University of Manitoba for great support of this research.

I kindly acknowledge Alex Wall, Mitchel Peters, Lucas Wazney, and my colleagues for their valuable contributions and help through this research. I would also like to thank my dear friends in Winnipeg for the happy time we had together.

Lastly, I would like to thank my family, and in particular my husband for his encouragement and supports throughout my life.

Dedication

To my dear parents, and my beloved spouse!

Table of Contents

List of Tables

List of Figures

Chapter 1: INTRODUCTION

1.1 Motivation

River ice jams have been an important issue for most northern countries, especially in Canada (Beltaos, 1995; Beltaos and Burrell, 2002). In cold regions, most of the rivers face freeze-up and break-up phenomena for days to months. During freeze-up and break-up, accumulation of ice pieces by congestion or obstacles can lead to the creation of ice jams. As a result, the water depth abruptly increases, and severe floods may happen. For example, in 1950, the Bow River flooding in Alberta was due to a freeze-up jam (Beltaos, 1995). As an example of significant amount of staging, the water level of the Nelson River in northern Manitoba was observed to increase up to 12 meters because of massive freeze-up jams (Beltaos, 1995). Ice jams have potential for economic, environmental and ecological damages. For instance, a report showed that the annual damages of ice-jam events to the

physical infrastructure in Canada and the United States could reach up to CAN$60 million and US$100 million, respectively (Beltaos, 2008). Beltaos (2008) stated that "Manitoba Hydro has spent millions (in CAN$) to accommodate the impact of ice on the planning, design and construction of major capital works, and spends over CAN$500,000 annually to monitor and mitigate ice problems."

To eliminate or mitigate ice jam consequences, a better understanding ice jam formation and its effect on flow characteristics including flow velocity and turbulence intensity can be effective. This understanding can be used to improve and enhance the prediction capabilities of present numerical models to forecast floods caused by an ice jam. More accurate water level predictions during ice jamming would help to reduce or control the damages to near-river infrastructure such as hydropower generating stations, houses and commercial properties.

Several types of research have been conducted to determine the mechanism of ice jam formation, growth, thickening, etc. However, reviewing the literature indicated there is limited research that has investigated the turbulent flow characteristics under ice jams because safety concerns prevent detailed flow measurements beneath an ice jam in the field. To help bridge this knowledge gap, this research aims to quantify the turbulent flow characteristics beneath a simulated ice jam in a laboratory. In general, a physical model helps to simplify a natural phenomenon; the characteristics of simulated phenomena can then be studied in detail. Also, it is possible to keep consistency between tests by preserving the same conditions for all tests. Therefore, an experimental analysis to determine the behavior of turbulent flow beneath an ice jam was proposed. It is anticipated that these results and future experimental work will improve our fundamental understanding of flow beneath an ice jam, and can be used for validation of subsequent ice jam numerical models.

1.2 Objectives

The goal of this experimental research is to investigate flow velocity, turbulence intensity, and bed shear stress variations at different streamwise locations beneath a simulated ice jam using an acoustic Doppler velocimeter. Also, the effect of various roughness ratios of the bed to ice jam on the flow velocity and turbulence intensity profiles, as well as bed shear stress distribution is evaluated. The research objectives are listed as follows:

- Measure and analyze streamwise velocity profile at different streamwise locations under the ice jam with varying roughness ratio of the bed to ice jam.
- Determine the variations of the magnitude and location of the maximum velocity at various streamwise locations under the ice jam with varying roughness ratio of bed to ice jam.
- Examine the effect of the ice jam on the bed shear stress along the ice jam to assess the scour potential and sediment transport under an ice jam.
- Quantify the turbulent flow characteristics at different streamwise locations beneath the ice jam.

1.3 Thesis Organization

This thesis consists of five chapters. Chapter 1 introduces the motivation and importance of the research, as well as research objectives. Chapter 2 reviews ice jam formation and the factors that impact formation, different types of ice jams, and presents a history of ice jam occurrences in the world. The background information on the hydraulic characteristics of open and full ice-covered channels flow is also presented including flow velocity, turbulence

intensity, and shear stress distribution. Then, the existing literature on ice jams is classified and the research gaps are highlighted. Chapter 3 describes the physical model setup and instrumentation as well as testing procedure and data collection during the experimental work. The results and analysis of the experimental outcomes are elaborated in Chapter 4. Chapter 5 summarizes the findings of this research and outlines possible extensions for future studies.

Chapter 2: LITERATURE REVIEW

This chapter will first introduce the types of ice jams and the factors that influence their formation. Then, some severe ice jams that happened around the world will be introduced. Afterward, the flow characteristics of open and fully ice-covered channels including streamwise velocity distribution, turbulence intensities and shear stress will be presented. Finally, the current literature on ice jams is reviewed.

2.1 Ice Jam Formation

In general, ice jams form when moving ice pieces become arrested at a particular location such as upstream of a large intact ice sheet, at an artificial obstruction (e.g., bridge piers), at river bends, and at natural constrictions including those caused by border ice formation. The severity of an ice jam is a function of different factors including river

discharge, width and slope of a channel, hydraulic resistance, strength characteristics of an ice jam, ice volume, and water temperature and heat transfer.

Ice jams can be classified based on three criteria including season, a state of evolution, and the condition of the jam toe. Based on the season, there are two types of ice jams: freeze-up and break-up jams. A set of comprehensive studies about the freeze-up and break-up of ice jams were accomplished by Beltoas in 1995 and 2008. Freeze-up jams form during the cold weather which occurs in late fall or early winter. In contrast, break-up jams form with positive or slightly negative air temperature which usually happens in spring. Surface and equilibrium jam are some types of ice jams based on its evolution. A surface jam appears as a single layer of ice floes due to the low flow velocity at the edge of a floating obstacle. An equilibrium ice jam forms when the upstream ice supply is steady and continuous for a long period of time. If the toe of the jam touches a channel bed, a grounded jam will be formed. This study is focused on an equilibrium ice jam which can be either considered as freeze-up or break-up jam. Different parts of an equilibrium jam as discussed in Beltaos, 2008 and 1995 are described in detail as follows.

An equilibrium ice jam is comprised of three regions: upstream transition, equilibrium reach, and downstream transition as shown in Figure 2-1 (Beltaos, 2008). In the upstream transition, incoming ice pieces are added to the ice jam, thereby increasing its total length. The jam thickness in the upstream transition region increases with downstream distance. In the equilibrium region, incoming ice pieces increase the jam length rather than the jam thickness due to a balance in resisting and driving forces on the ice cover; hence, the jam thickness remains constant in this region. The water surface and channel bed slope are equal in this region. In the downstream transition, the jam thickness increases with flow direction

depending on various factors such as channel slope, flow velocity, incoming ice volume, channel bed morphology, roughness under the intact ice cover, etc. In this region, the jam thickness grows until it meets with the lowest water depth at the toe of the jam. This region consists of two parts: an upper toe region (UTR) and a lower toe region (LTR). Unlike the equilibrium region, the water surface slope is steeper than the channel bed slope in the downstream transition region.

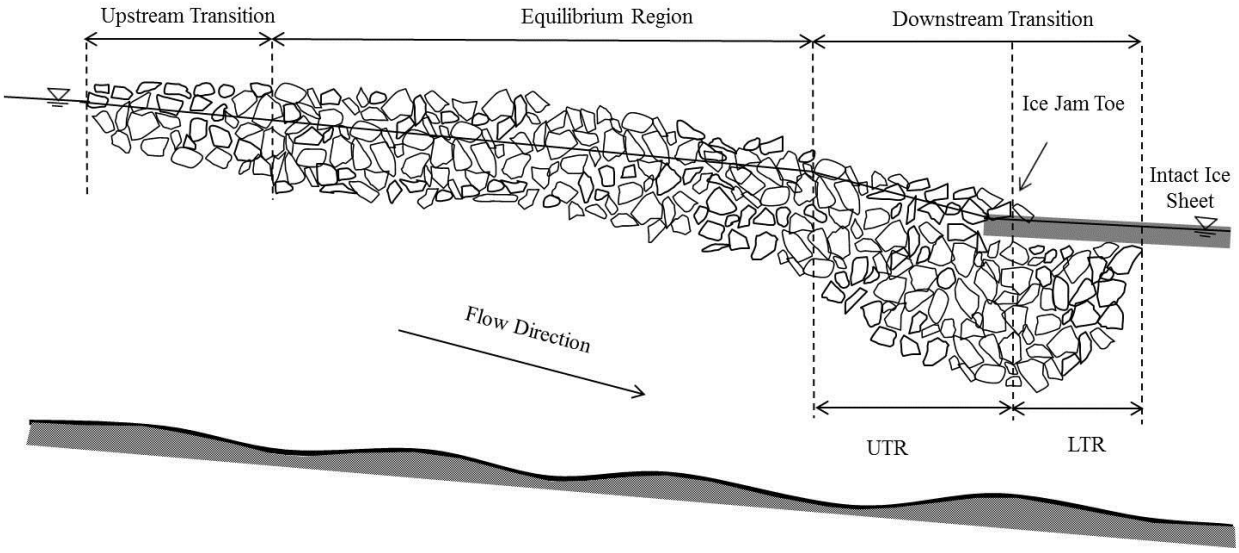

Figure 2-1: Schematic side view of an equilibrium ice jam (adapted from Beltaos, 2008).

2.2 Ice Jam History

In northern countries, river ice jams are an important issue due to the potential for economic, environmental, and ecological damage (Beltaos, 2008). Several extreme floods have been reported around the world due to ice jams. For example, in Asia, severe floods due to ice jams happened in the north part of China, on the Heilongjiang River, in 1985 and also, in Russia, on the Lena River, in 1998. In Europe, Iceland (Eliasson, 1994), Finland

(Kuusisto, 1994), Norway (Kilingtveit, 1994), and Sweden (Bengtsson, 1994) are examples of countries which experienced such events (Beltaos, 1995). Also, many ice jam events have occurred in the north part of the United States. Montana (MT), New York (NY) and Wisconsin (WI) are the states that had more significant ice jam events compared to other states in the US. Canada, in particular, has experienced extreme flood events caused by river ice jams (Beltaos, 1995; Beltaos and Burrell, 2002). The Dauphin River, the Nelson River, and mouth of the Red River in Manitoba are examples of rivers that are prone to such events. Some severe floods in Canada due to river ice jams are summarized in Table 2-1.

Table 2-1: River ice jams events in Canada (Beltaos, 1995).

	Location	River	Date
Atlantic Canada	Nova Scotia	Salmon	1988
	New Brunswick	St. John	1970
Central Canada	Quebec	St. Lawrence	1886
	Quebec	Francois	1989
	Quebec	Yamaska	1991
	Quebec	Chaudiere	-
	Ontario	Niagara	1938
Prairies	Manitoba	Swan	1989
	Alberta	Bow	1950
	Manitoba	Nelson	-
Western and Northern Canada	British Colombia	Liard	1989
	British Colombia	Fort Simpson	1989

2.3 Open Channel Flow

In general, flow in natural channels like rivers and creeks, as well as in artificial channels such as irrigation canals, flumes and wastewater channels are referred to as open channel flow since the water surface always contacts atmospheric pressure. Flow in most open channels is turbulent and the Reynolds number in such channels typically exceeds 12,500 (French, 1985). In turbulent flow, the water particles move in irregular paths which can lead to relatively high energy dissipation. The dimensionless Reynolds number is defined as the ratio of the inertial forces to the viscous forces. In turbulent flow, the inertia forces dominate the viscous forces. Therefore, the Reynolds number is used as criteria to show the level of turbulence of the flow.

2.3.1 Velocity Distribution

In an open channel, the velocity distribution usually varies across the channel section due to the existence of the free surface and friction along the boundaries (Chow, 1959). In such a channel the flow velocity is low near the solid boundaries and increases gradually further from the boundary. The velocity gradient is severe near the boundary; however the gradient is mild beyond the boundary layer.

The maximum velocity in open channels may occur at or near the free surface depending on some parameters including flow velocity, flow depth, and channel roughness (Chow, 1959). Chow (1959) pointed out “In a broad, rapid and shallow stream or in a very smooth channel, the maximum velocity may often be found at the free surface.” However, in general, the maximum velocity is located at 5 to 25 percent of total flow depth below the free surface (Chow, 1959) due to secondary currents which frequently exist in all types of channels

(Henderson, 1966; Nezu and Nakagawa, 1993). The secondary currents are rotational movement of fluid particles perpendicular to the streamwise flow direction. The secondary currents are due to channel geometry and lateral variation in boundary roughness. The secondary current velocity is approximately equal to 5 percent of the streamwise velocity (Nezu and Nakagawa, 1993). By knowing the location of the maximum vertical velocity in open channels, the strength of the secondary currents can be determined (Henderson, 1966).

There are several methods to determine the average velocity magnitude in open channels such as the Manning equation and the two-point method. The Manning equation is the most common prediction method to estimate the average velocity in uniform open channel flow. It has been proven that the Manning equation is most reliable in practice and extremely popular in most Western countries (Henderson, 1966) and also has vast application in the hydraulic design of open channels. The Manning equation is represented as follows:

$$V_{avg} = \frac{k}{n} R^{2/3} S^{1/2} \qquad \text{Equation 2-1}$$

where, V_{avg} is the mean velocity, k is equal to 1 in SI units and 1.49 in imperial units, R is the hydraulic radius which is ratio of cross sectional area to wetted perimeter of the cross section ($R=A/P$), S is the channel slope, and n is the Manning's roughness coefficient. The Manning's roughness coefficient which is representative of the resistance to flow in a channel has been experimentally determined for common channel bed materials. The value of the Manning's roughness coefficient is affected by various parameters such as surface roughness of the wetted channel perimeter, channel alignment, channel geometry, existence

of obstructions in the channel, and flow rate (Chow, 1959; Pritchard, 2011). The channel discharge can be calculated by knowing the flow velocity (V_{avg}) multiplied by the cross sectional area of the channel (*A*).

The two-point method is one of the more applicable methods to estimate the mean velocity in open channels. In this method, the average of the flow velocity at a depth of 0.2 and 0.8 of the total flow depth are measured. The average between the two measurements is considered as the mean velocity for a particular vertical profile in a channel (Equation 2-2).

$$V = \frac{v_{0.2d} + v_{0.8d}}{2} \qquad \text{Equation 2-2}$$

Determination of a general formulation to predict the velocity distribution in open channels with different characteristics is complicated, stemming from the effects of some factors such as boundary roughness, and natural or irregular cross sections. However, the logarithmic law (log-law) and power law are well-known methods to describe velocity profiles of open channel flows. Description of each method is presented as follows.

The logarithmic law

The flow field in open channels is divided into two layers: the inner layer and the outer layer. The inner layer corresponds to 15% to 20% of the total flow depth ($y/h < 0.15$-0.2) and the outer layer is for the remainder of the flow depth ($0.15\text{-}0.2 \leq y/h \leq 1$) in which *y* is the distance from the channel bed and *h* is the total flow depth (Nezu and Nakagawa, 1993;

Kırkgoz, 1989). In the inner layer, viscous and turbulent shear stresses are very important (Sturm, 2001) and two characteristic scales including velocity scale (u_*) and length scale (ν/u_*) are considered in this region in which u_* is the friction velocity and ν is the fluid kinematic viscosity (Balachandar et al., 2002). In the outer region, the importance of the viscous forces becomes negligible.

The velocity distribution in the inner layer can be predicted by the law of the wall. The inner region itself is divided into three layers including the viscous-sublayer, the buffer layer, and the fully turbulent layer (Nezu and Nakagawa, 1993; Kırkgöz, 1989). The viscous-sublayer is located very close to the wall and the viscous forces are much important in this region (Sturm, 2001). The law of the wall in the viscous-sublayer is presented as follows:

$$U^+ = y^+ \qquad \text{Equation 2-3}$$

where,

$$y^+ = \frac{yu_*}{\nu}, \qquad U^+ = \frac{U}{u_*} \qquad \text{Equation 2-4}$$

U is mean streemwise velocity. The law of the wall in the fully turbulent layer, in which both viscous and turbulent shear stresses are important, is known as the "logarithmic law" which is presented as follows:

$$U^+ = \frac{1}{K}\ln(y^+) + C \qquad \text{Equation 2-5}$$

in which, K is the von Karman constant and C is the integral constant. In this research, the value of 0.41 and 5 will use for K and C, respectively (Coles, 1956). The Equation 2-5 is used for smooth channels; for rough channels the roughness shift (ΔB) must be considered. Therefore, the logarithmic law for rough open channels is as follow:

$$U^+ = \frac{1}{K}ln(y^+) + C - \Delta B \qquad \text{Equation 2-6}$$

Keulegan (1938) mentioned that in open channels, the logarithmic law can be considered for velocity distribution over the whole depth of flow. Sturm (2001) stated that the logarithmic law can be applied over nearly the full depth of flow except in cases of increasing or decreasing pressure gradients. There is no simple formula for the buffer layer which is located between the viscous-sublayer and the fully turbulent layer (Nezu and Nakagawa, 1993). Most of the turbulent energy is produced and dissipated in the buffer layer (Balachandar et al., 2002).

In the outer layer, the average velocity distribution has a deviation from the logarithmic law. To show this deviation, the logarithmic law was extended by adding the wake function

(Balachandar et al., 2002). The new equation is named the velocity-defect law or log-wake law which is presented as follows:

$$U^+ = \frac{1}{K}\ln(y^+) + C + w\left(\frac{y}{h}\right) \qquad \text{Equation 2-7}$$

in which, $w\left(\frac{y}{h}\right)$ is a wake function. Several empirical formulas have been proposed for the wake function; but, the wake function that was obtained by Coles (1956) appears to be the most acceptable extension of the logarithmic law (Nezu and Nakagawa, 1993).

The Power law

The power law is an experimental formula which is applied to describe the velocity distribution in open channel flows (Cheng, 2007). The power law for uniform flows in a wide open channel is as follows:

$$\frac{U}{U_{max}} = \left(\frac{y}{h}\right)^{1/m} \qquad \text{Equation 2-8}$$

where, U is the mean streamwise velocity, U_{max} is the maximum streamwise flow velocity, h is the flow depth, y is a distance from the channel bed to the measured point, and $1/m$ is the power-law index (exponent). Different values have been proposed for the index for instance, Cheng (2007) stated that " Prandtl suggested that the one-seventh power law (m = 7) can be

used for turbulent flows over a smooth boundary to approximate the velocity profiles in boundary layer flows for low Reynolds numbers."

2.3.2 Turbulence Intensities

Turbulent flow fluctuations can be described by turbulence intensities which are the root mean square of the difference between instantaneous velocity and time average of the instantaneous velocity (Nezu and Nakagawa, 1993). Turbulence intensities in three dimensions are theoretically calculated from the following equations:

$$u_{rms} = \sqrt{\overline{(u-U)^2}} \qquad \text{Equation 2- 9}$$

$$v_{rms} = \sqrt{\overline{(v-V)^2}} \qquad \text{Equation 2- 10}$$

$$w_{rms} = \sqrt{\overline{(w-W)^2}} \qquad \text{Equation 2- 11}$$

where u_{rms} , v_{rms} and w_{rms} are turbulence intensities; *u*, *v*, and *w* are instantaneous velocities, and *U*, *V*, and *W* are the average of the instantaneous velocities, in flow direction, vertical direction, and lateral direction, respectively. Despite the aforementioned theoretical equations, semi- empirical exponential equations were obtained by Nezu and Nakagawa (1993) to calculate the all three components of turbulence intensities. In these equations, the constants of the exponential functions are independent of the Reynolds number and Froude number. The equations are represented as follows:

$$\frac{u_{rms}}{u_*} = 2.3\, exp\left(-\frac{y}{h}\right) \quad \text{Equation 2-12}$$

$$\frac{v_{rms}}{u_*} = 1.27\, exp\left(-\frac{y}{h}\right) \quad \text{Equation 2-13}$$

$$\frac{w_{rms}}{u_*} = 1.63\, exp\left(-\frac{y}{h}\right) \quad \text{Equation 2-14}$$

The exponential equations indicate that the turbulence intensities have a decreasing trend with increasing normalized flow depth (*y/h*) so that the turbulence intensities have a maximum value near the solid boundary and minimum value near the free surface. Moreover, a general relationship among the turbulence intensities is $u_{rms} > w_{rms} > v_{rms}$ (Nezu and Nakagawa, 1993).

2.3.3 Shear Stress

Due to the water movement in a channel, a force which is known as shear or drag force, is applied to solid boundaries. The shear force in open channels occurs on the wetted perimeter which is the channel bed and sidewalls. In order to approximate the flow resistance in open channels, boundary shear stress, which is a ratio of the shear force to the unit wetted area, can be used. The boundary shear stress can be divided into bed shear stress and sidewalls shear stress. Regarding application, the bed shear stress is used to estimate the sediment transport rate of a river bed, and the sidewalls shear stress may be used to determine riverbanks erosion rate. The mean boundary shear stress over the entire cross-section for uniform open channel flows can be calculated with the following equation (Chow, 1959):

$$\bar{\tau}_{bdy} = \gamma RS \qquad \text{Equation 2-15}$$

where, $\bar{\tau}_{bdy}$ is the mean boundary shear stress, and γ is specific weight of water. It is worth mentioning that the boundary shear stress is not uniformly distributed over the wetted perimeter of an open channel. The boundary shear stress distribution is a function of cross-sectional shape, the boundary roughness, and the existence of secondary flows (Khodashenas et al., 2008; Nezu and Nakagawa, 1993). Several attempts have been made to determine the distribution of the boundary shear stress in an open channel (Khodashenas et al., 2008; Knight et al., 1984; Ghosh and Roy, 1970; Yang and Lim, 2005). For example, Knight et al. (1984) carried out some experimental works to specify the spanwise distribution of bed shear stress in smooth rectangular open channels. Their findings indicated that the bed shear stress has a symmetric distribution with respect to the center of the cross section. The bed shear stress has minimum values in the corner of the channel, two mild peaks near the sidewalls, and maximum value in the center of the channel. By increasing distance from the side walls, the bed shear stress increases rapidly from its minimum values in the corners to attain the mild peaks. Then, it grows to reach its maximum value in the center of the channel. To provide a boundary shear stress distribution over the entire cross-section of an open channel, it is required to measure the friction velocity values at different points on the boundary across the channel. By knowing the local value of the friction velocity, the local boundary shear stress can be obtained using the following equation:

$$\tau_b = \rho u_*^2 \qquad \text{Equation 2-16}$$

where, τ_b is the local boundary shear stress and ρ is the flow density. There are different methods to calculate the friction velocity, but the logarithmic law is perhaps the most well-known and practical of them. In this method, the friction velocity is defined using the Clauser plotting technique in which the vertical distribution of streamwise velocity near the boundary is fitted to the logarithmic law by changing the friction velocity as a fitting parameter.

The variation of the shear stress over the flow depth is linear as shown in Figure 2-2. The maximum shear stress occurs on the bed where the flow velocity is minimal. Conversely, the minimum shear stress happens at the free flow surface where the flow velocity is maximal.

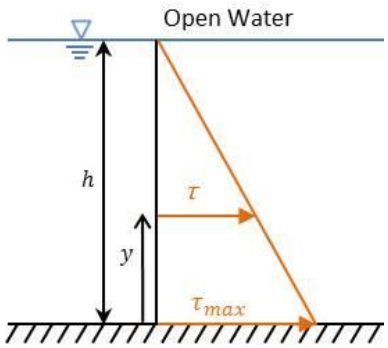

Figure 2-2: The vertical distribution of shear stress over the flow depth in an open channel

Vertical distribution of the shear stress over the flow depth can be obtained using the following equation:

$$\tau = \mu\frac{du}{dy} - \rho\overline{u'v'} \qquad \text{Equation 2-17}$$

where, τ is the shear stress either on the channel bed or at a measurement point over the flow depth, μ is the dynamic fluid viscosity, $\frac{du}{dy}$ is the mean streamwise velocity gradient, and $\overline{u'v'}$ is the Reynolds shear stress. The first and second parameter on the right-hand side of Equation 2-17 refers to the laminar component and turbulent components, respectively. The laminar component is important near the solid boundary while the turbulent component is dominant away from the solid boundary.

2.4 Effect of Continuous Ice Cover on Channel Flow

In northern environments, river channels are ice-covered for a portion of the year. The flow characteristics of an ice-covered channel differ markedly from that of open channel flow, due to the presence of an additional solid boundary at the free surface of the flow. For instance, the added top boundary increases flow depth, wetted perimeter and flow resistance.

2.4.1 Velocity Distribution

The imposition of an additional upper boundary from an ice cover can significantly change the velocity distribution in a river. These differences are exemplified by comparing vertical distributions of streamwise velocity for the two conditions, as shown in Figure 2-3 (Teal et al., 1994). It can be seen that the existence of the ice cover forces the location of the maximum velocity to a lower depth.

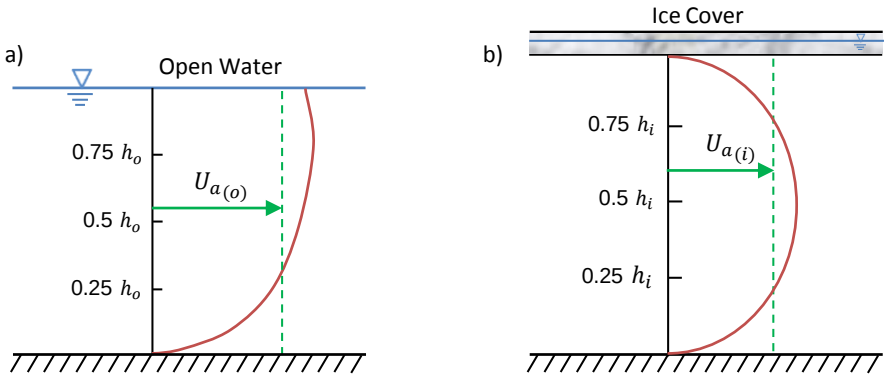

Figure 2-3: Velocity distribution in a) open channel and b) ice-covered channel (adapted from Teal et al., 1994).

The location of the maximum velocity depends on the roughness ratio of the ice cover and channel bed (Lau, 1982; Gogus and Tatinclaux, 1981). In other words, the maximum velocity tends to recede from the rough boundary and locate near the smooth boundary when one boundary is rougher than another one so the velocity profile becomes asymmetric. Moreover, if the roughness of the channel bed is equal to the roughness of the ice cover, the maximum velocity occurs at local mid-flow depth, and then the velocity profile is symmetric. In nature, the roughness of the ice cover and river bed are unequal for most of the ice-covered channels; therefore, the velocity distributions are usually asymmetric in such channels.

Commonly, the "two-layer hypothesis" has been used in description of the velocity distributions and analysis of flow in ice-covered straight channels (Ashton, 1986; Tatinclaux and Gogus, 1983; Parthasarathy and Muste, 1994; Hanjalic and Launder, 1972; Zufelt and Ettema, 1997; Uzuner, 1975; Gogus and Tatinclaux, 1981); however, the two-layer hypothesis is not appropriate to analyse the flow details in curved ice-covered channels (Urroz and Ettema, 1994). Based on the two-layer hypothesis, the flow field under an ice

cover is divided into two regions: the bed-affected region and the ice-affected region as shown in Figure 2-4. Note that in Figure 2-4, the subscripts *b* and *i* refer to variables of the bed- and ice- affected regions, respectively. The bed-affected region, as its name implies, is affected by the channel bed roughness and similarly, the ice-affected region by the ice cover roughness. The velocity distribution in the each region is approximately similar to that of open channels. It is assumed that the velocity profile of the bed- and ice-affected regions intersect each other at the location of maximum velocity (Ashton, 1986; Yamaguchi and Hirayama, 1990; Tsai and Ettema, 1996; Sui et al., 2010). There are contradictory assumptions about the coincidence of the plane of maximum velocity and zero shear stress. For example, some researchers (Gogus and Tatinclaux, 1981; Hanjalic and Launder, 1972) stated that the maximum velocity plane does not coincide with the zero shear stress in fully developed turbulent asymmetric flows.

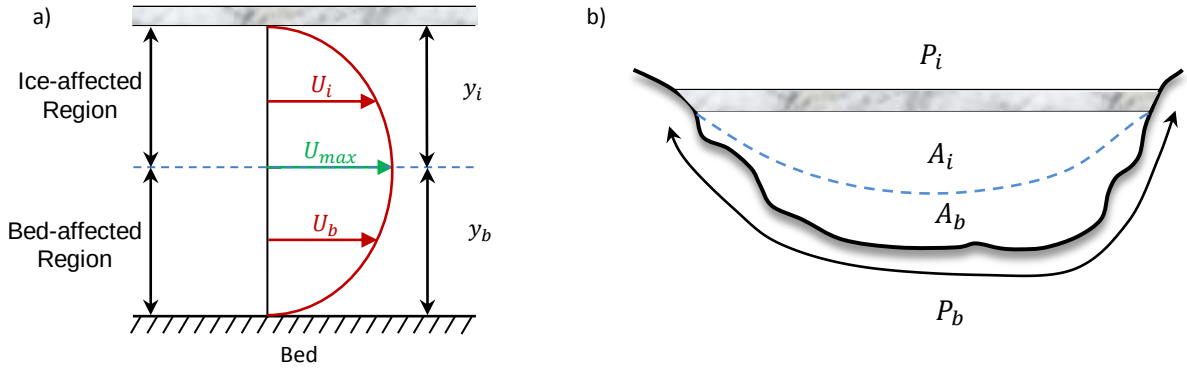

Figure 2-4: The two –layer hypothesis in ice-covered channels, (adapted from Ashton, 1986).

Investigations indicated that the vertical distribution of streamwise velocity in the bed- and ice-affected region follow either the logarithmic law or power law. However, there are

various claims and discussions about the best distribution. Some researchers declared the logarithmic law is valid in both the bed- and ice-affected region to show the velocity distribution (Calkins et al., 1980; Dolgopolova, 1998; Yamaguchi and Hirayama, 1990). For instance, Yamaguchi and Hirayama (1990) performed three-year field measurements during winter in several rivers in Hokkaido, Japan, under various ice cover and bed roughness conditions to gauge flow velocity beneath the ice cover. Their findings showed the vertical distributions of streamwise velocity in both the bed- and ice-affected region fit well to the logarithmic law. However, they figured out that the calculated maximum velocity using the logarithmic law was slightly higher than the measured one. Lau (1982) indicated that the logarithmic law was not very well applied for the entire bed- and ice-affected flow region. According to Lau's detection, the logarithmic distribution was valid for 60% of the flow depth closest to the ice and bed boundary in the each flow region. For the remaining 40% of the flow depth in the each region, which are close to the location of the maximum velocity, there was a deviation from the logarithmic distribution.

Furthermore, application of the power law was examined by different investigators to demonstrate the vertical profile of streamwise velocity in ice-covered channels. Dolgopolova (1998) used the power law for her field data which were collected from Moskava River, in Moscow, Russia. The results showed the field data fit well to the power law in the bed- and ice-affected area. Also, Tsai and Ettema (1994) accepted the two power law was a good estimation for ice-covered channel flows with asymmetric two boundaries roughness. In order to utilize the power law over the entire local flow depth, Teal et al. (1994) extended the power-law statement which was expressed by Tsai and Ettema (1994). They used several river data including Mississipi at Altkin, Floyd at James, Brule near Fence, and Chippewa

near Bruce as well as some experimental data to evaluate the accuracy of the extended two power law in ice-covered channels. Their results indicated the two power law which depends on the flow depth and the bed and ice cover roughness, is well fitted to the velocity profile under the ice covers. The two power law based on Teal et al. (1994) in the ice-covered channels is as follows:

$$u = K_0(\frac{y}{h})^{1/m_b}(1-\frac{y}{h})^{1/m_i} \qquad \text{Equation 2-18}$$

where, K_0 is a constant for a given flow rate, and m_b & m_i are the bed and ice cover roughness, respectively.

The Manning formula is also applicable for ice-covered channel flows to calculate the average streamwise velocity; but, the composite roughness (n_c) is used for the Manning's roughness coefficient. This is because of the additional boundary at the flow surface, results in added roughness from the undersurface of the ice cover. The composite roughness can be determined using different analytical methods such as average n method, the alpha method, Larsen method and Sabaneev method; the Sabaneev method is the most common approach in the literature (Ashton, 1986). The composite roughness based on the Sabaneev method can be estimated using the following equation:

$$\frac{n_c}{n_b} = \left(\frac{1 + (n_i/n_b)^{3/2}}{2} \right)^{2/3} \quad \text{Equation 2-19}$$

where, n_c is the composite roughness, n_b is the bed roughness, and n_i is roughness of the ice cover.

Validation of the two-point method in ice-covered channels was confirmed by some researchers, whereas others did not agree about the accuracy of the two-point method in ice-covered channels. The two-point method was recommended to utilize for estimation of mean streamwise velocity in ice-covered channels with the adjustment coefficient of 0.98 in order to obtain the more precise mean velocity (Teal et al., 1994; Lau, 1982; Yamaguchi and Hirayama, 1990). Healy et al. (2002) conducted the experimental works at the rectangular flume with 30.5m length, 1.22m width and 0.91m height and used a flexible rubber mat with 12m length and rough underside as a simulated the floating ice cover. They recommended the two-point method was applicable for unsteady flow under a floating ice cover as well as steady flow. Nevertheless, field measurements in the United States showed the two-point method was not suitable to predict the mean velocity in the ice-covered channels (Walker, 1994).

2.4.2 Turbulence Intensities

The existence of the ice cover in channels can also modify the turbulence intensity distributions in ice-covered channels compared to open channels. Dolgopolova (1994) stated that the average of the turbulence intensities for flow in ice-covered channels was much higher than that for open channels.

In ice-covered channels, the dimensionless turbulence intensities decrease with increasing distance from the channel bed to reach their minimum value, and then begin to increase towards the ice cover. Therefore, the maximum local turbulence intensities occur near the boundaries, and minimum local ones happen near the plane of zero shear stress (Parthasarathy and Muste, 1994; Robert and Tran, 2012). It is noticeable that the roughness ratio between the channel bed and ice cover influence the turbulence intensities distribution. Accordingly, as the boundary roughness increases, the turbulence intensities enhance. Hence, the shape of the turbulence intensities will approximately be symmetric if the roughness of the channel bed and ice cover is equal; otherwise, the shape is asymmetric.

Some research indicated that the exponential equations which have been used to estimate the turbulence intensities in open channels can be applied with a good approximation to those in ice-covered channels in bed- and ice-affected regions (Parthasarathy and Muste, 1994; Sukhodolov et al., 1999).

2.4.3 Shear Stress

The boundary shear stress in ice-covered channels is divided into the shear at the bed and channel banks, and the shear stress at the underside of an ice cover. The boundary shear stress distribution can be analyzed using the two-layer hypothesis in ice-covered channels (Zufelt and Ettema, 1997; Gerard, 1981). The average boundary shear stress and local shear stress in the ice- and bed-affected region can be estimated using the same equations as used for open channels. Literature review indicated that the boundary shear stress distribution across the ice-covered channels is markedly different from that of open channels. For example, experimental research of Leutheusser (1963) and Knight et al. (1984) indicated that

the bed shear stress distribution over a cross section of the covered channel had a minimum value and two peak values. The minimum value was observed at the center of the cross section while, the peak values were approximately occurred at the half distance from each channel sidewall towards the cross-section center.

The longitudinal shear stress distribution over the flow depth is linear in an ice-covered channel. In other words, in the bed-affected region, the shear stress is at a maximum at the channel bed, and linearly decreases to zero near the location of maximum velocity. This also is true for the ice-affected region. Figure 2-5 shows the vertical distribution of shear stress throughout the flow depth under an ice cover with an assumption of equal boundaries roughness. The zero shear stress plane is displaced depending on the roughness of the ice cover and channel bed. In asymmetric ice-covered channels, the plane of zero shear stress is not coincident with the maximum velocity plane and is located near the smoother boundary (Hanjalic and Launder, 1972; Parthasarathy and Muste, 1994). Conversely, in symmetric covered channels, the plane of zero shear stress coincides with the maximum velocity plane (Parthasarathy and Muste, 1994).

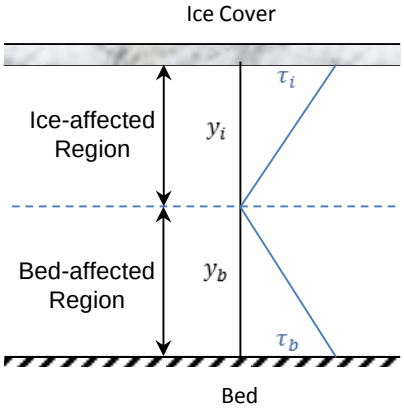

Figure 2-5: The distribution of longitudinal shear stress over the flow depth in an ice-covered channel.

2.5 Review Ice Jams Studies

Several theoretical and experimental studies have been conducted to investigate ice jam formation and development (Pariset and Hauser, 1961; Zufelt and Ettema, 1997; Hicks and Bonneville, 1998; Tatinclaux and Lee, 1978; Healy and Hicks; 2006; Kawai et al., 1997; Urroz and Ettema, 1994; Zufelt and Sun, 1988). For example, Tatinclaux and Lee (1978) experimentally modeled the initiation of an ice jam using a symmetrical partial surface blockage as an obstruction, as well as real and artificial ice pieces as ice floes. They investigated effects of the obstruction and material features of the modeled ice pieces on the formation and development of the ice jam.

Effects of ice jams on morphology and bedform of channels have been investigated by several researchers (Wuebben, 1988; Ettema and Daly, 2004; Mercer and Cooper, 1977). Wuebben (1988), for instance, conducted experiments to examine scour patterns beneath an ice jam on a movable sand bed. He modeled the upstream transition and equilibrium region of the ice jam using a floating plywood box of uniform thickness with a sloped leading edge. The jam was located behind a simulated intact ice cover using styrofoam. However, the downstream transition of the jam was not completely modeled. The streamwise flow velocity profiles at different locations beneath the jam were shown; however, details were limited. The results demonstrated that scour was a function of the jam thickness and that the maximum scour potential was located at the thickest portion of the jam.

Field investigations of river ice jams have been undertaken across Canada (Beltaos and Moody, 1986; Beltaos et. al., 1996; Prowse, 1986; Kowalczyk and Hicks, 2003; She et. al., 2009). For instance, Beltaos and Moody (1986) measured thickness of a break-up ice jam on the Thames River, Ontario, to improve understanding of a breakup ice jam configuration. She

et. al. (2009) monitored break-up ice jam events on the Athabasca River at Fort McMurray, Alberta in order to analyze the process of the ice jam formation and release. Furthermore, several numerical models have been developed to predict the formation of river ice jams (Beltaos, 1993; Shen, 2002; Carson et. al., 2011; Kolerski, Huang, and Shen, 2016). As an example, Kolerski et al. (2016) extended a two-dimensional numerical model for break-up jams to examine development of an ice jam toe configuration.

To sum up, considerable knowledge and advancement have been obtained by the extensive studies about ice jam events; however, there are limited field and experimental data in the literature regarding flow characteristics beneath an ice jam.

Chapter 3: METHODOLOGY

The present research was performed in the Hydraulics Research & Testing Facility (HRTF) at the University of Manitoba. The experimental facility consisted of a flume with adjustable discharge and tail water level. The flow velocity was measured using an acoustic Doppler velocimeter (ADV).

3.1 Experimental Facility

The experiments were conducted in a straight rectangular flume 14 m long, 1.22 m wide, and 0.6 m deep (Figure 3-1a). The flume bed had a fixed slope of 0.0025 for all runs. High density overlay (HDO) plywood was used for construction of the flume bed and sidewalls. There was a large head tank (3.68 m long and 2.43 m wide) at the upstream end of the flume. The floor and sidewalls of the head tank were built from HDO plywood sheets as well. A flow straightener consisting of several rows of PVC pipes (0.14 m diameter, 0.25 m long)

surrounded by two wire mesh screens was located in the upstream head tank to condition the flow. In order to convey the flow smoothly to the flow straightener, polyethylene sheets in an arc shape were installed inside of the head tank, before the PVC pipes. To reduce recirculation effects, a projecting inlet with the same dimensions as the flume was placed immediately downstream of the flow straightener (Figure 3-1b). The water level in the flume was manually controlled by a gate acting as a weir at the downstream end of the flume (Figure 3-1c).

The flow recirculation was as follows: the water was extracted from a large underground reservoir through a 60 horsepower pump to an elevated constant head tank. Afterward, the water was conveyed to the flume by a 350 mm diameter PVC pipe into the head tank, where it then entered the flume. Lastly, the water was collected at the end of the flume by floor drainage channels and returned to the large underground reservoir.

a)

b)

c)

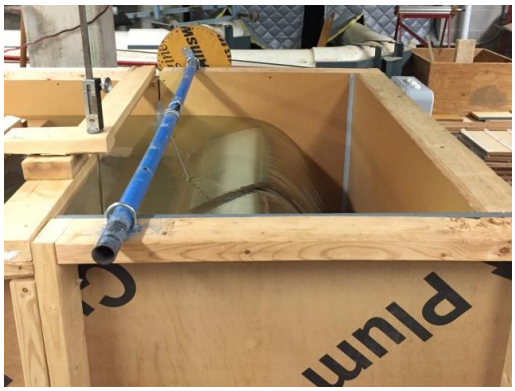

Figure 3-1: a) Flume model at the laboratory, b) flume projecting inlet, c) downstream end of the flume.

3.2 Physical Model Design and Construction

Initially, discrete artificial ice pieces were used to model an ice jam. For this purpose, the model ice pieces were cut from polyethylene sheets that had a specific gravity approximately the same as natural ice pieces. Zufelt and Ettema (1996) presented good information about types and properties of different materials for physical modeling of ice cover. The ice pieces

were a mixture of various sizes with a square shape (Figure 3-2). However, due to the laboratory facility limitation and excessive complexity associated with experiments conducted with discrete ice pieces, the ice jam was modeled as a solid jam using solid wood sheets instead of the discrete artificial ice pieces.

Figure 3-2: The artificial ice pieces.

A solid ice jam was constructed from HDO plywood sheets (2.44 m long, 1.22 m wide, 0.019 m thick). Starting at the upstream 4.88 m length of HDO was used to construct the equilibrium region (EQR) of the ice jam. Next, the downstream transition region of the jam consisted of two sections of HDO with lengths of 1.8 m and 0.64 m, set at a downward slope of 5º (UTR) and an upward slope of 14º (LTR), respectively (Figure 3-3). These slopes were selected as a compromise between the available field measurements and the physical limitations of the flume length and instrumentation. A downstream intact sheet (DIS) of ice was constructed using 5.88 m length of HDO.

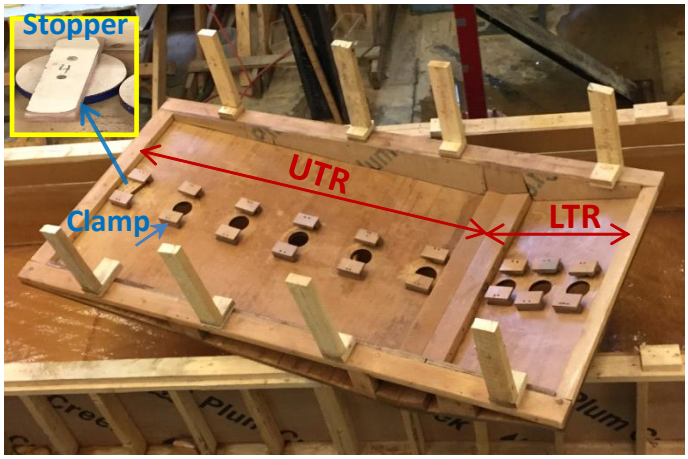

Figure 3-3: Downstream transition region of the modeled ice jam.

In this study, all the measurements were conducted along the centerline of the flume to minimize secondary flow effects. Therefore, fifteen holes which were cut along the centerline of the jam in order to facilitate water velocity measurement with an ADV were selected. Three holes were placed in the EQR at 1.06 m spacing, six holes in the UTR at 0.3 m spacing, three holes in the LTR at 0.15 m spacing, and three holes in the DIS at spacing 0.64 m and 0.54 m (Figure 3-4). For each hole, a HDO plywood stopper was prepared so that it was fixed by two clamps and aligned to the underside of the ice cover to block the holes when they were not in use (Figure 3-3).

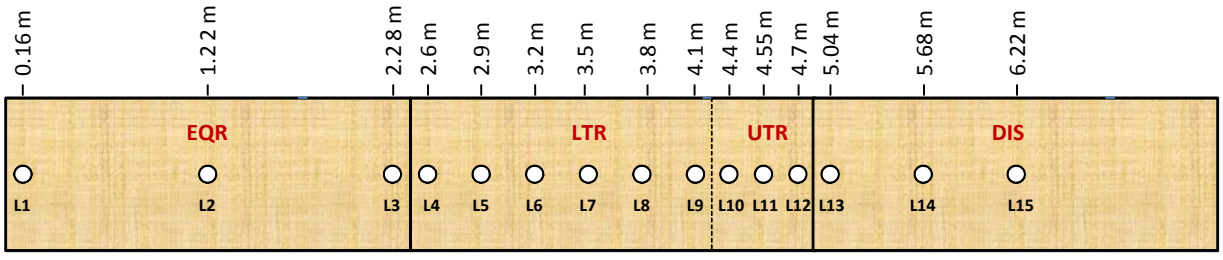

Figure 3-4: The simulated ice jam plan view with measurement locations.

To make a rough bed and rough ice jam, acrylic ribs (1.2 m long, 1.3 cm wide and 1.3 cm thick) were glued on the flume bed and screwed to the under surface of the modeled ice jam (Figure 3-5). The ribs were uniformly spaced 13 cm apart, perpendicular to the flow direction. In this case, the thickness to spacing ratio of the ribs was 0.1. The space between each rib was selected to maximize the effects of the roughness elements on the flow (Leonardi et al., 2003). The roughness elements were used for all sections of the equilibrium jam, while the DIS was left as smooth HDO to resemble a smooth intact ice cover that could typically be found near the entrance to a lake. Note that an intact ice cover grows by thermal processes (initially start with border ice) while an ice jam becomes larger over a period of time by the addition of discrete ice pieces.

a)

b)

c)

Figure 3-5: a) Downstream transition, b) upstream of the rough jam, and c) rough flume bed.

3.3 Setup of ice jam physical model

Before installation of the ice jam in the flume, the edges of the cover and holes as well as the wooden baffles were coated with a waterproof liquid to prevent water penetration into the cover and baffles. Several wooden legs were used to fix the ice jam to the flume sidewalls; six legs per sheet for the EQR and DIS, and eight legs for the downstream transition region of the jam. The legs for the EQR and DIS were located at upstream, downstream, and middle of the each sheet. The middle legs prevented the sheet from bending. Installation of the ice jam was started at the upstream end of the flume when there was no water in the flume. The first sheet of the EQR at a specific height from the flume bed was attached to the flume sidewalls by the legs. When the sheet was leveled, the second sheet was installed. In the same way, the remaining parts of the jam were installed in the flume. The individual sheets were connected to each other along the length of the flume using joint plates to make a stable ice jam. The installed ice jam in the flume is presented in Figure 3-6.

a)

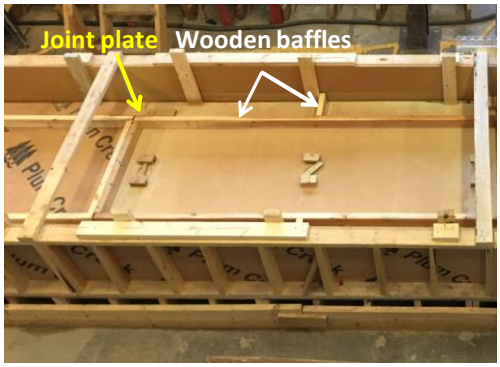

b)

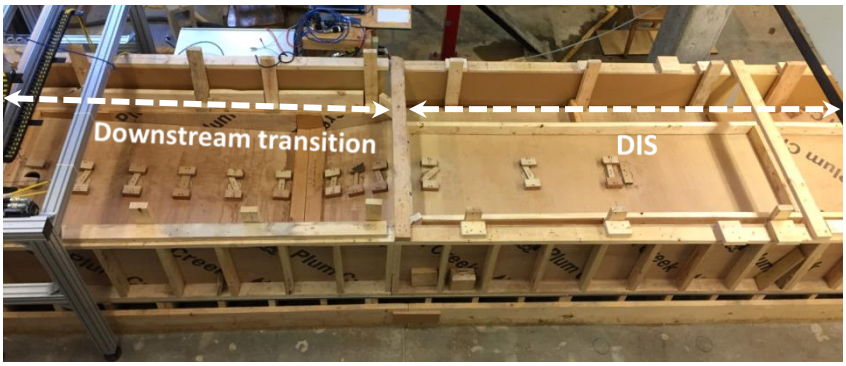

Figure 3-6: The installed ice jam in the laboratory, a) EQR and b) downstream transition and DIS.

Two scenarios were considered for the modeled ice jam. For the first scenario, it was assumed that the DIS and the EQR had an equal elevation of 26 cm from the flume bed. In this case, the UTR had a downward slope of 5º and the LTR had an upward slope of 14º. The side view of this experimental setup is shown in Figure 3-7a. Usually in nature, the upstream end of an ice jam is located at a higher elevation than the downstream end. Therefore, the second scenario was developed to construct a physical model of an ice jam more similar to a real ice jam. The base assumption in the second scenario was a height difference between the DIS and EQR. Hence, the DIS was located 5 cm lower than the EQR (Figure 3-7b). The EQR and the DIS were located at height of 30 cm and 25 cm from the flume bed, respectively. In this condition,

the slope of the UTR increased to 6º compared to that of in the first scenario while the LTR slope decreased to 13º relative to the first scenario. It was required that there should be enough room between the toe of the jam and the bed (h_{toe}) to measure velocity at a sufficient number of points to accurately capture velocity profiles. Based on the requirements for the h_{toe} and selected UTR angle, the elevation of the different parts of the jam from the bed was determined.

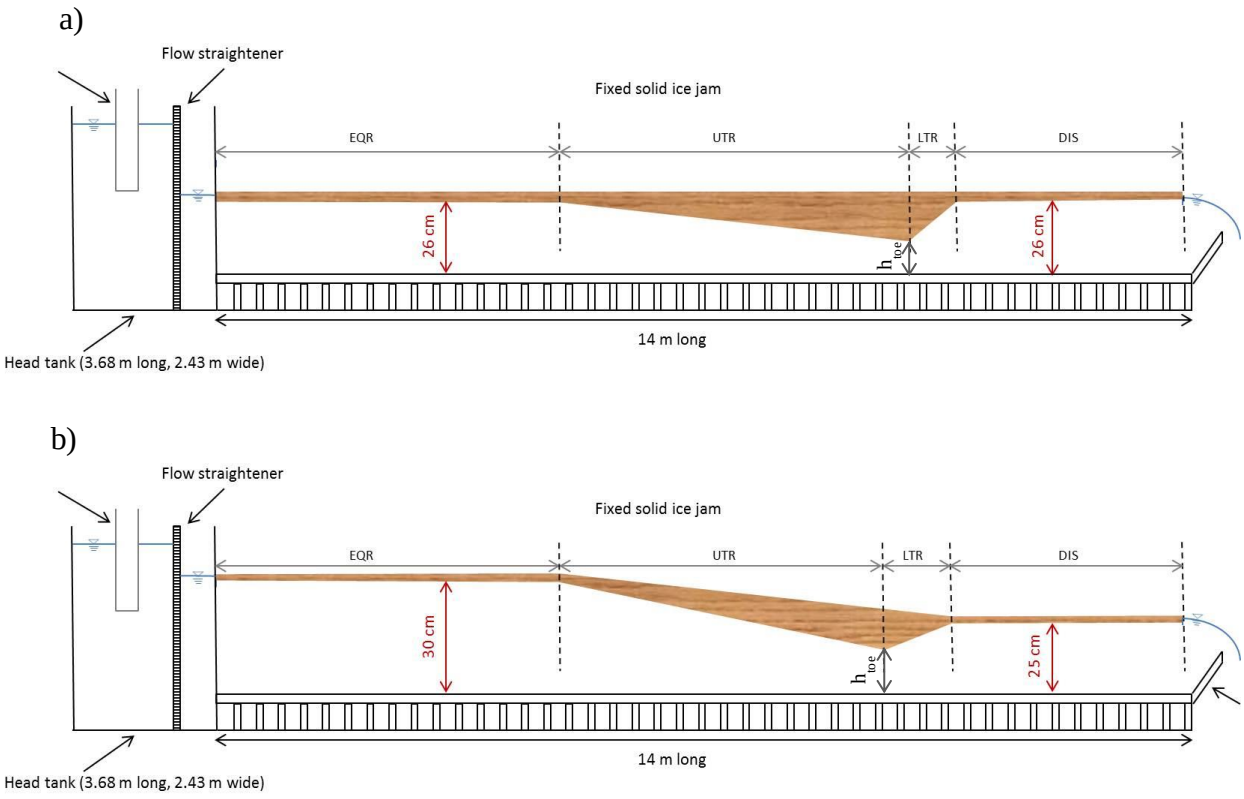

Figure 3-7: Schematic longitudinal profile view of the experimental setup, a) scenario 1 and b) scenario 2.

3.4 Instrumentation

A down-looking Nortek Vectrino profiler ADV with cable probe was used in this study to measure water velocity. The ADV can simultaneously measure three-component water velocity in the streamwise, spanwise, and vertical directions. The probe head of the ADV contains one transmitter and four receivers (Figure 3-8). The ADV measures water velocity using the pulse-coherent processing. Based on this technique, the ADV sends out acoustic pulse pairs from the transmitter; the reflection is recorded by the four receivers. The reflections are recorded from a defined sampling volume. The water velocity is estimated by measuring the phase shift between two subsequent pulses based on the Doppler shift. The main assumption is that the measured velocity of scattering particles is similar to the water velocity. The sampling volume of the ADV is a hypothetical cylinder of water with diameter of 6 mm similar to the transmitter diameter, and with an adjustable height from 1 mm to 30 mm. The sampling volume is comprised of number of cells with a selectable thickness from 1 mm to 4 mm (Nortek, 2013). In order to provide undisturbed measurements, the center of the sampling volume is located 50 mm from the transmitter, at the focus point of the receivers. The ADV can measure the flow velocity in the selectable range of ±0.1 m/s to a maximum of ±3 m/s, at a frequency ranging from 1 to 100 Hz.

Figure 3-8: Down-looking ADV with cable probe.

The ADV was mounted on a computer-controlled traversing mechanism; hence, it could be automatically moved in the vertical and lateral direction at sub-millimeter spatial resolution. In addition, the traversing mechanism held the ADV with minimal vibration. The entire traversing mechanism and ADV had to be positioned manually along the streamwise direction. The probe head of the ADV was attached to a solid rod which was screwed into a rectangular plate of the traversing mechanism (Figure 3-9). Two point gauges, one in the head tank and another at the downstream end of the flume were used to monitor the water level during the experiments.

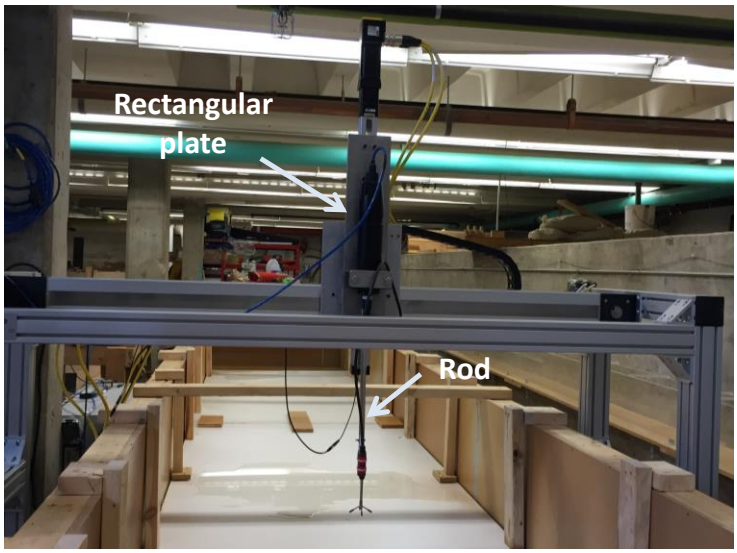

Figure 3-9: ADV mounted to the traversing mechanism.

3.5 Data Collection

Once the ice jam was installed in the flume, the flume was run and water flowed into the flume. The flow rate was set using an ultrasonic flow meter. To determine an accurate value of the flow rate in the flume, volumetric tests were conducted before the initiation of each test. When the discharge and the water elevation were constant, the water level was raised on top of the cover by raising the downstream gate. Since a down-looking ADV was used, and the entire probe needed to be submerged in order to take measurements, the upper-most sampling location would be several centimeters beneath the ice cover. To facilitate measurements closer to the underside of the ice, once the ice cover elevation was fixed the entire ice cover was submerged by approximately 5 cm. Several wooden baffles covered the upper surface of the ice to ensure that this submergence would not add to the channel conveyance.

At the measurement locations, the traversing mechanism was aligned using a level and square, and then the ADV probe was lined up using a small level. When one hole was used for measurement, the rest of the holes were plugged with the HDO stoppers in order to prevent water from exiting. When the hole was open water near the top cover tended to flow in the upwards direction instead of following the ice cover geometry. To create a stable boundary condition in the measuring location, acrylic boxes were fabricated (Figure 3-10); for the UTR, LTR, EQR and DIS. Hence, for each measurement location, the appropriate box was used. The difference in water surface condition above a measurement hole with and without an isolation box is shown in Figure 3-11. Figure 3-12 shows what the top surface of the ice cover looked like in a typical experiment.

To measure the flow velocity profile near the boundaries (within 20% of the flow depth), the center cell of measured points were spaced 8 mm apart from each other in the vertical direction. For the remainder of the water column, a distance of 1 cm was selected.

As described before, the ADV sends out acoustic pulses to the water and the scattering particles in the water reflect the pulses to the receivers. Therefore there should be enough scattering particles, or seeding material, in the water to obtain reliable data. A signal to noise ratio (SNR) criterion was used to check the amount of the seeding material in the water; if the recorded SNR was low, the seeding material should have been added. The seeding material was used for this study was glass beads with 10 µm diameter. For this material, it was confirmed that the fall velocity and the relaxation time were small in comparison with typical velocity and time scale of the flow. Hence, the added seeding material tracked the flow correctly.

a) b)

Figure 3-10: Acrylic boxes a) in the downstream transition of the jam and b) in the flat parts of the jam.

a) b

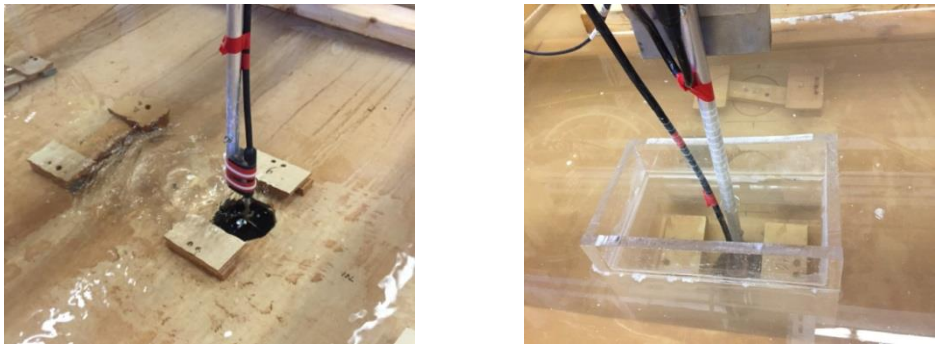

Figure 3-11: Flow condition above the measuring hole a) without using a box and b) with using a box.

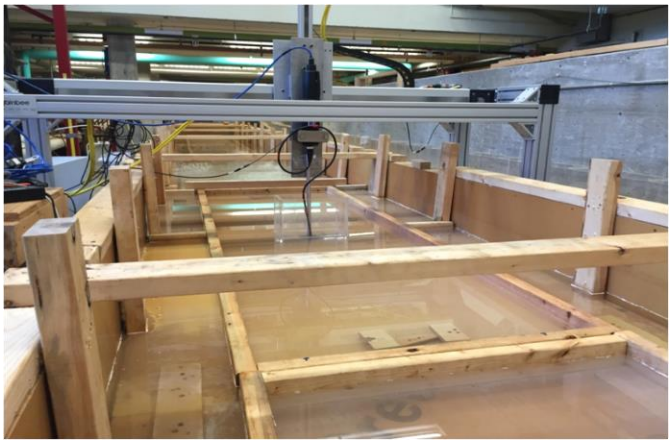

Figure 3-12: Data collection condition.

3.6 Post-Processing of Collected Data

A post-processing code in Matlab was utilized to eliminate or replace poor quality data to present more reliable and accurate results. This code was divided into three steps including: 1) identify and remove bad cells; 2) despiking and noise removal; and 3) compiling results. In step one, data quality criteria containing correlation value and signal to noise ratio value (SNR) were used to estimate the quality of the recorded data. Also, weak spots were identified in this step. The ADV pulse coherent technique can lead to the existence of weak spots that occur when measuring near boundaries (Nortek, 2013). A weak spot happens when the reflection of the first pulse from a boundary interferes with the second pulse in the sampling volume. The correlation value which is a value between 0% and 100% indicates how well a return pulse correlates with the pulse that was sent out. The minimum applied threshold for the correlation was 30%. If more than 10% of measured data in a cell had correlation below 30%, the cell was removed. The SNR criteria indicated how the return signal is contaminated by noise. The minimum applied threshold for the SNR was 15 dB. If more than 10% of measured data in a cell had an SNR value of less than 15 dB, the cell was removed.

In the second step, the filtered data were entered into the second step of the refinement to despike and remove noise. Outlier points in a velocity time history illustrate spikes in the velocity time history. Among different methods to despike and remove the outlier points from the velocity time history, the Goring and Nikora method (2002) was selected for this study. Inherently, there are errors in the ADV's measurements due to instrument noise. The noise influences measured turbulence intensities and turbulent kinetic energy but, there is minimal effect on mean velocity, Reynolds shear stresses and third momentum turbulence

statistics. The noise was removed from the turbulence intensities and turbulent kinetic energy using the Hurther and Lemmin method (2001) demonstrated in Durand (2014). In the last step, all the processed data were combined and saved as a Matlab and Excel file.

3.7 Preliminary Tests

Prior to conducting the experiments with a simulated ice cover, initial experiments under open channel conditions were undertaken. Initial convergence tests were conducted to determine the appropriate ADV sampling duration. Velocity measurements were collected at a frequency of 100 Hz near the flume bed and in the free stream for 30 minutes. The highest frequency was selected for the ADV to measure turbulence intensity with high accuracy as well as to get as much data as quickly as possible. Mean velocities and turbulence intensities were plotted against the sampling time (the number of samples) to determine the suitable number of samples with an acceptable level of error (Figure 3-13). A total of 18,000 samples (3 minutes duration) was found to have an uncertainty less than 5% for the mean 3D velocities and less than 8% for the turbulent statistics (except for Reynolds stress ($-\overline{uv}$)) near the flume bed. Also, in the free stream, the mean 3D velocities and the turbulent statistics had an uncertainty less than 0.25% and 2% after 3 minutes, respectively. The error associated with the ADV is ±0.5% of the measured value ±1 mm/s (Nortek, 2013).

a) b)

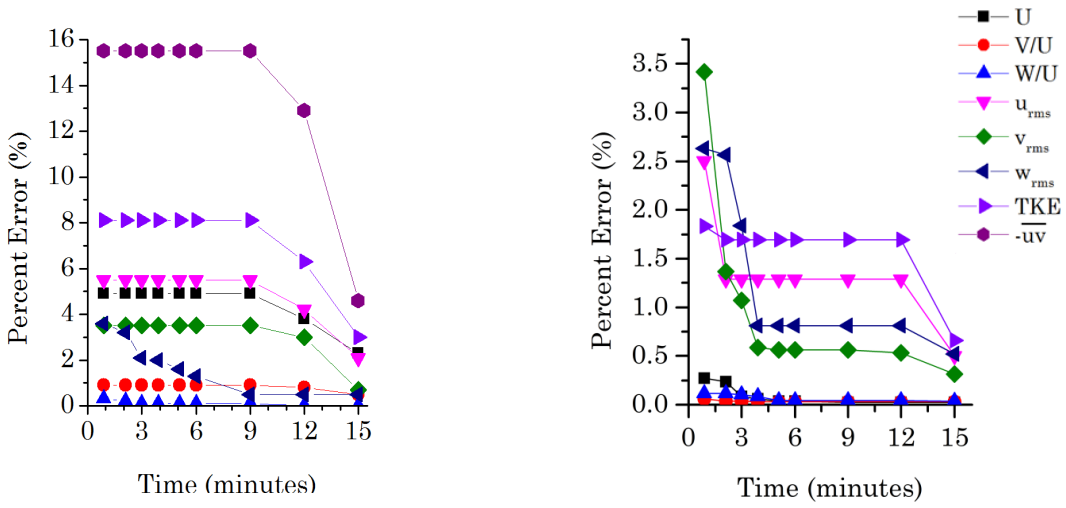

Figure 3-13: Convergence test of mean 3D velocities and turbulent statistics a) near the flume bed and b) in free stream (Peters, 2015).

Although the Vectrino Profiler has the ability to measure 30 cells of 1 mm height simultaneously; only the central 7 cells were used in this study (Figure 3-14b). These cells were selected to obtain more reliable data and a correct velocity profile.

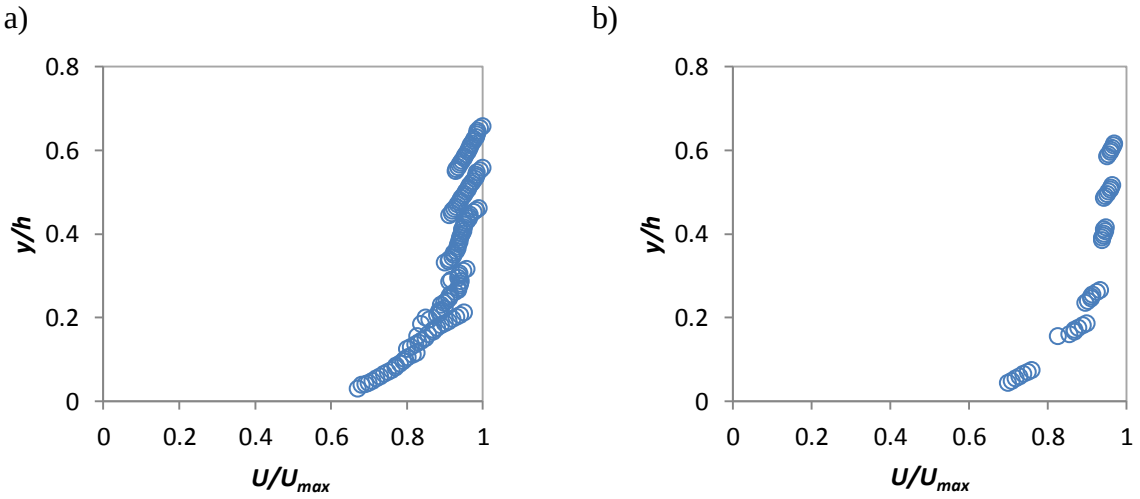

Figure 3-14: Comparison of streamwise velocity profiles with various cell numbers.

Two experiments were conducted in open flow condition to determine the development length of the flow. The mean streamwise velocity profile was measured along the centerline of the flume at locations 1, 2, 4, and 8 m from the flume inlet. Comparison of the velocity profiles showed the profiles were self-similar for 2, 4, and 8 m, demonstrating that the flow became fully developed by 2 m from the flume inlet (Figure 3-15).

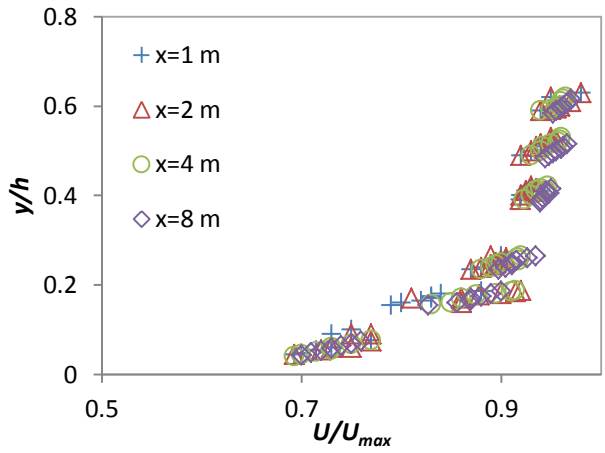

Figure 3-15: Dimensionless streamwise velocity profiles in the developing flow length.

Two experiments were implemented in open flow and fully covered flow condition to examine whether the flow was symmetric relative to the flume centerline. The measurements were performed in a full cross section of the flume, located 8 m from the inlet. To do measurements, in addition to the down-looking ADV, a Nortek Vectrino+ side-looking ADV with a cable probe that can measure flow velocity at a single cell was used (Figure 3-16). The cable probe of the ADVs allowed the ADV probe to be located in different orientations. Hence, the probe of the side-looking ADV was turned 90º at upward direction and used for collecting data near the underside of the upper cover.

Figure 3-16: Side-looking ADV.

The side-looking ADV recorded data at a frequency of 200 Hz with a sampling height of 2.5 mm and a sampling duration of 3 minutes. The down-looking ADV was set in downward and sideward direction to measure as much of the flow as possible. For the fully covered flow condition, the entire flume was covered using the HDO sheets. There was only a small gap between the covers at the measurement location. The symmetry experiment setup for the fully covered channel is shown in Figure 3-17.

In the open flow condition, mean 3D velocities and turbulent statistics of half of the cross section was compared to each other. The results indicated the flow was also symmetric in open flow condition (Peters, 2015). In addition, measurements confirmed that the flow was approximately symmetric across the flume centerline in the fully covered condition. The mean velocity and turbulence intensity profiles in the streamwise, vertical, and spanwise directions are presented in Appendix A.

a)

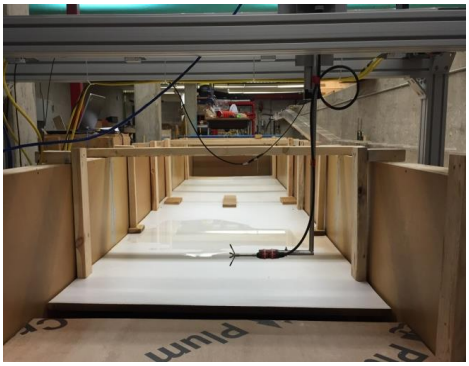

b)

c)

Figure 3-17: Symmetry experiment condition for fully covered channel using a) down-looking ADV in side direction, b) down-looking ADV in down direction, and c) side-looking ADV in up direction.

3.8 Experimental Conditions

The experiments for the modeled ice jam were undertaken in one set of tests for scenario 1 (Figure 3-7a) and three series of tests for scenario 2 (Figure 3-7b). For scenario 1, the ice jam and bed were smooth. For scenario 2, different roughness ratios of the bed to ice jam were considered including smooth bed and smooth ice jam, smooth bed and rough ice jam, and rough bed and rough ice jam hereafter referred to as Tests SB&SJ, SB&RJ, and RB&RJ, respectively (Figure 3-18).

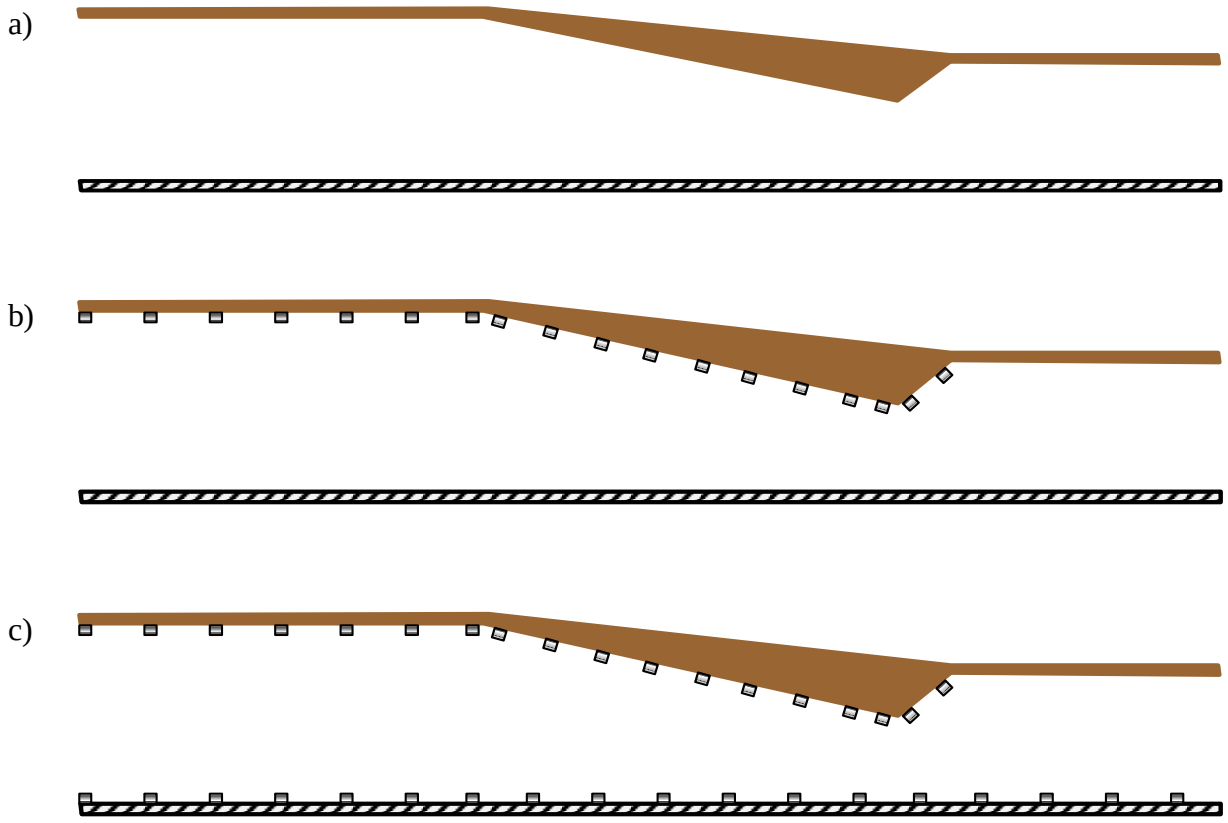

Figure 3-18: Schematic side view of boundary roughness condition for scenario 2: a) SB&SJ, b) SB&RJ, and c) RB&RJ.

For scenario 1, the flow measurements were performed at fifteen different locations along the centerline of the ice jam. Based on the comparison of the flow measurements, ten locations among the fifteen locations were identified to be meaningfully different in terms of flow characteristics. Therefore, 15 vertical profiles were measured for scenario 1 while a total of 10 vertical profiles per test were undertaken for scenario 2. The locations and relevant flow depth as well as distance from the entrance of the flume for each scenario are summarised in Table 3-1.

Table 3-1: Streamwise measurement locations and local flow depth for scenario1and 2.

	Scenario 1		Scenario 2	
Location	Distance from the inlet (m)	Local flow depth (m)	Distance from the inlet (m)	Local flow depth (m)
L1	2.601	0.260		
L2	3.660	0.260	3.660	0.300
L3	4.719	0.260	4.719	0.300
L4	5.041	0.246		
L5	5.341	0.220	5.338	0.248
L6	5.641	0.194		
L7	5.941	0.168	5.935	0.185
L8	6.241	0.142		
L9	6.531	0.116	6.522	0.122
L10	6.85	0.145	6.846	0.149
L11	7.003	0.181	6.993	0.183
L12	7.140	0.217	7.139	0.216
L13	7.506	0.26	7.479	0.250
L14	8.150	0.26		
L15	8.690	0.26	8.663	0.250

A constant discharge of 92±2 l/s and 88±2 l/s were used for scenario 1 and scenario 2, respectively. The Froude number and Reynolds number were calculated at the equilibrium region (EQR) of the ice jam using the following equations.

$$Fr = \frac{V_{avg}}{\sqrt{gh}} \quad , \quad Re = \frac{V_{avg} D_H}{\nu} \qquad \text{Equation 3-1}$$

where, D_H is the hydraulic diameter of flow in a pipe and it is defined as $4R$. Based on the calculations, the Froude number at the equilibrium region was obtained 0.18 and 0.14 for scenario 1 and 2, respectively. The Reynolds number at the equilibrium region was 125,965 and 115,200 for scenario 1 and 2, respectively.

Chapter 4: RESULTS AND DISCUSSION

This chapter discusses the effects of the ice jam on the turbulent flow characteristics in the channel for scenario 1 and scenario 2. For scenario 2, the effects of the boundary roughness on the flow features are also investigated. These findings are presented and elaborated in this chapter.

4.1 Scenario 1

4.1.1 Mean Streamwise Velocity Profiles

The dimensionless mean streamwise velocity profiles (U/U_{max}) versus normalized flow depth (y/h) under the simulated ice jam are presented in Figure 4-1 and Figure 4-2. Hereafter, U is the mean streamwise velocity at a particular vertical location, U_{max} is the local maximum streamwise velocity, y is the vertical distance from the bed, and h is the local flow depth. In the

EQR, self-similarity of the velocity profiles for L2 and L3 demonstrated that the flow became fully developed by position L2 (Figure 4-1). It should be noted the roughness of all boundaries was the same and the flow depth was nearly constant at 26 cm. Consequently, the velocity profiles had a parabolic shape with a maximum velocity at the mid-depth (Zufelt and Ettema, 1997).

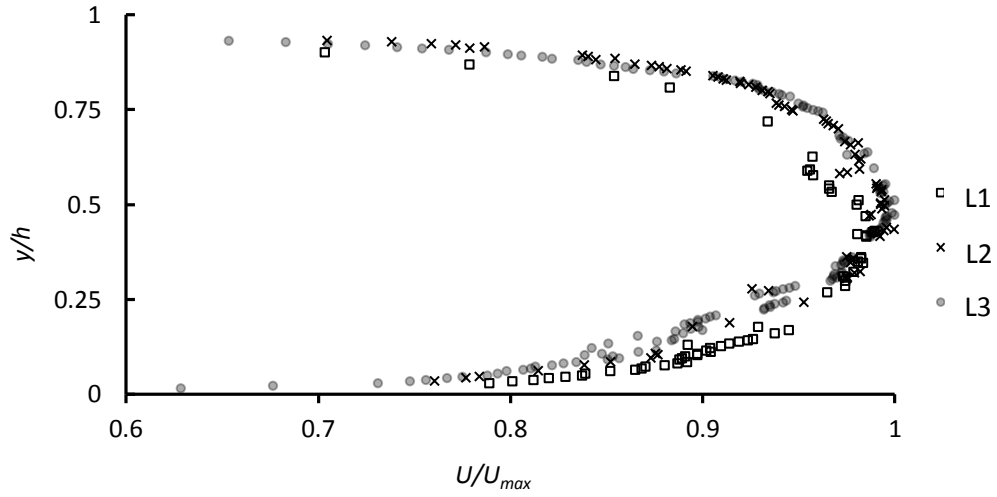

Figure 4-1: Dimensionless streamwise velocity profiles in the equilibrium region.

The development of the mean streamwise velocity profiles in the UTR, LTR, and DIS are shown in Figure 4-2. In the UTR (Figure 4-2 (a) and (b)), as the flow contracted, the down-sloping ice surface caused the flow area to reduce and flow to accelerate. Thereby, the streamlines moved more in the downwards direction and the average cross sectional velocity increased compared to the EQR.

In the LTR (Figure 4-2 (c)), flow expanded because of the increasing cross sectional area. In this region the velocity profiles have a distinct S-shape with a zone of low velocity near the upper boundary. This was due to the effects of flow separation, and diminished as the flow developed and reattached to the upper boundary. As the water decelerated due to the expansion, the average velocity decreased.

Under the DIS (Figure 4-2 (d)), the flow reattached to the upper boundary. The velocity profile in L13 differs from L14 while there is a small difference between the profile for L14 and L15. In L13, the velocity gradient near the bed is higher than in L14, however, the velocity gradient in the top quarter of the flow depth of L13 is smaller than in L14, but becomes greater in the next lower quarter. Following L15, if the flow condition was the same as the EQR and the length of the downstream cover had been sufficient, then the flow would have tended to redevelop and return to that of the velocity distribution in the EQR. A summary of all streamwise velocity profiles beneath the ice jam at different locations is presented in Figure 4-3, where the dashed vertical lines correspond to the axis $U = 0$, for each respective velocity profile.

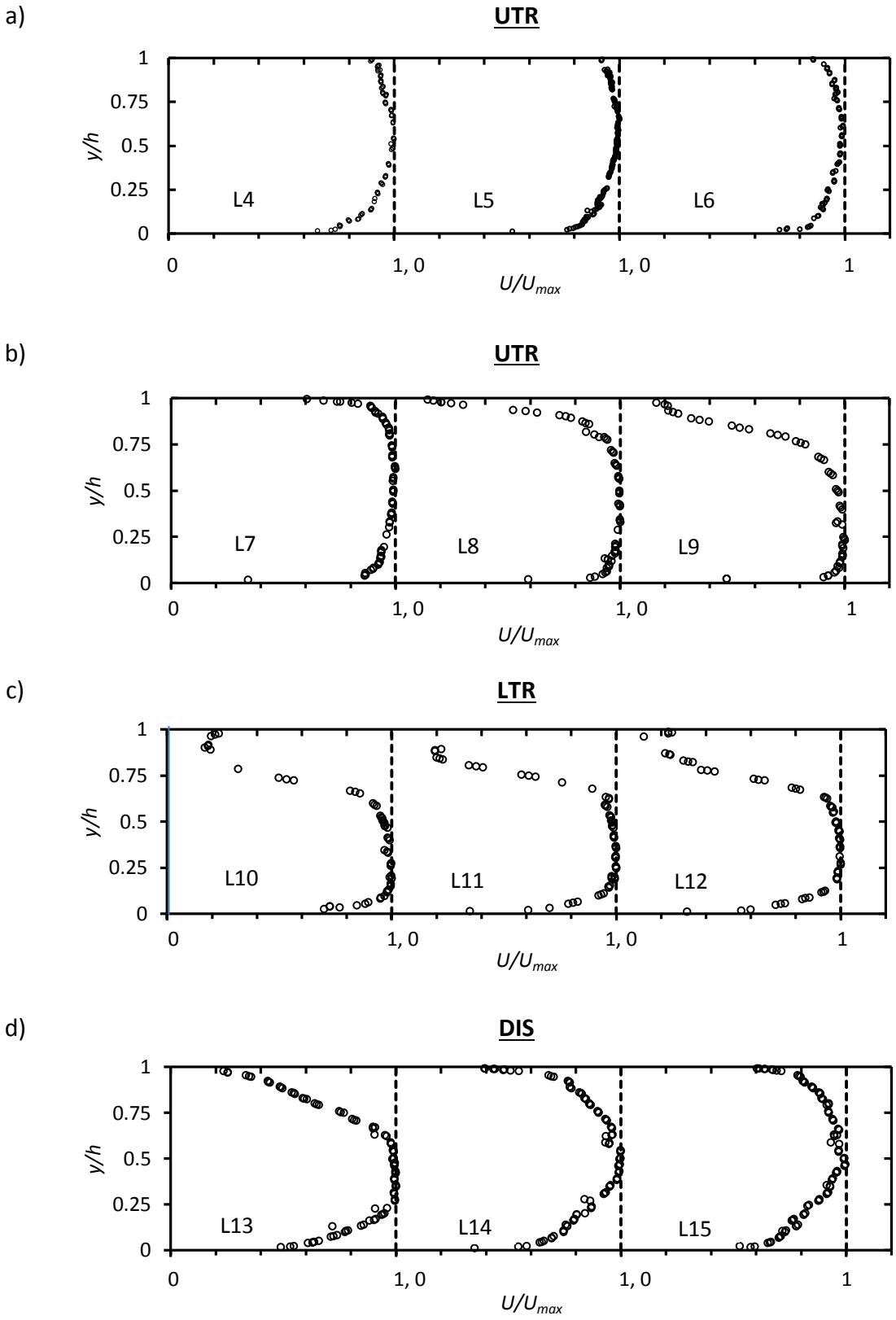

Figure 4-2: Dimensionless streamwise velocities in the (a) and (b) UTR, (c) LTR, (d) DIS.

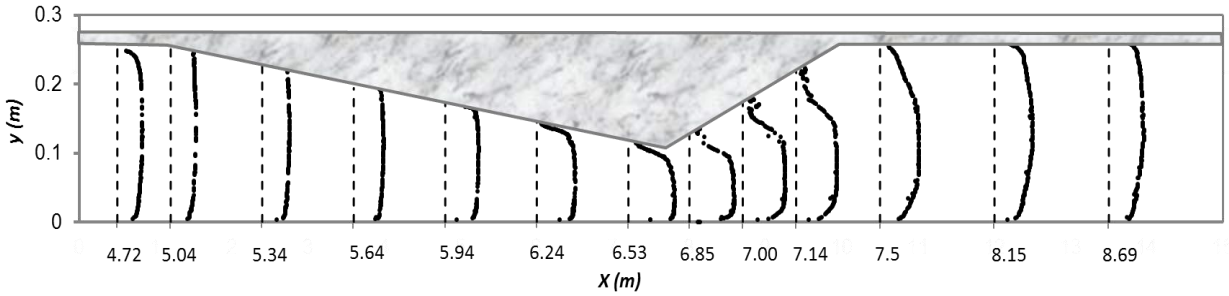

Figure 4-3: Centerline streamwise velocity profiles at different locations beneath the ice jam.

4.1.2 Maximum streamwise velocity location and magnitude

The position of the local maximum streamwise velocity beneath the simulated ice jam is shown in Figure 4-4, along with the local mid-flow depth. It can be seen that the maximum velocity in the EQR occurred near the middle of the flow depth. When the uniform flow developed in the EQR reached the UTR, its momentum caused the location of maximum velocity to be above the mid flow depth. As the effects of the angled upstream boundary were felt by the flow, it began to develop and the location of maximum velocity approached the mid flow depth. Near the toe of the jam (L8 and L9) the maximum velocity was below the mid flow depth and closest to the bed. The streamlines were contracted more in this area that causes the majority of the discharge to pass near the bed. As the flow developed in the LTR, the location of the maximum velocity began to move upward, but it remained below the mid flow depth. Similar to the UTR, the variation of the maximum velocity location in LTR was affected by the cross section area changes and the associated flow separation zone near the upper boundary. In the DIS, the cross section area was constant and the flow separation zone disappeared, therefore the maximum velocity was observed again near the mid flow depth.

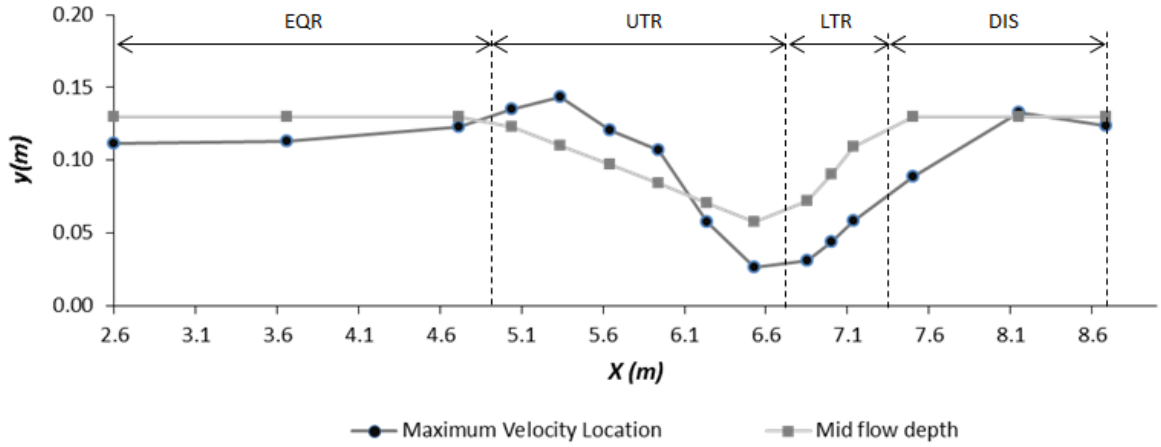

Figure 4-4: Vertical location of the maximum streamwise velocity under the ice jam.

Figure 4-5 shows the magnitude of the maximum velocity at different locations beneath the jam. As expected, the maximum velocity increased through the UTR and the highest maximum velocity was observed near the toe of the jam (L9) at the measurement location with the smallest cross sectional area. Afterward, the value of the maximum velocity decreased until it stabilized at a constant value under the DIS. There is a slight difference between the maximum velocity at L2 and L15 since the flow at L15 was not yet fully developed. The results clearly show that near the toe of the jam the potential for bed scour would be greatest due to the largest maximum velocity being located nearest to the channel bed, causing a local bed shear stress that is approximately four times that of the EQR. These results correspond to the findings of Wuebben (1988) who observed scour potential near the toe of a jam was much larger than other locations under an ice jam.

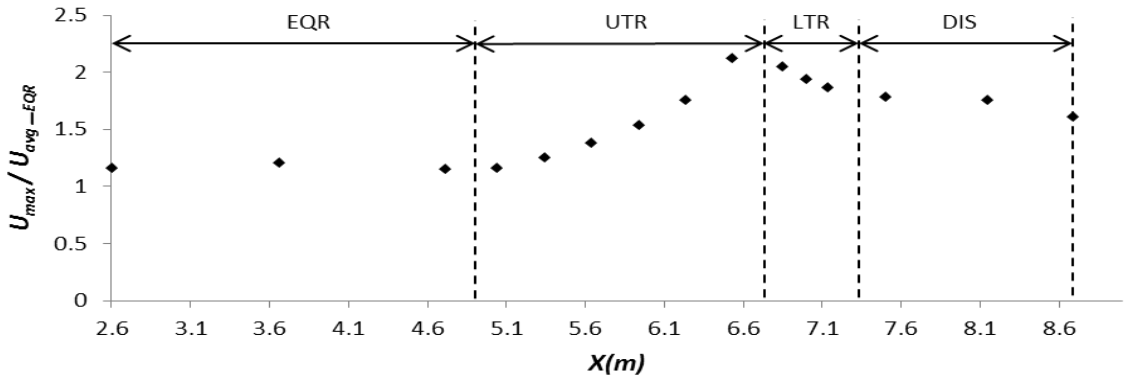

Figure 4-5: Magnitude of the maximum streamwise velocity under the ice jam.

4.1.3 Streamwise turbulence intensity profiles

The mean streamwise turbulence intensity (u_{rms}) is defined as the root-mean-square of the instantaneous streamwise velocity fluctuations. The normalized streamwise turbulence intensity (u_{rms}/U_{max}) results for each of the measurement locations are shown in Figure 4-6. In the EQR (Figure 4-6 (a)), the turbulence intensity is greatest near the upper boundary and has a minimum near the mid water depth. Conversely, in the open flow condition, turbulence intensity has its minimum value near the water surface as explained in Chapter 2. The results in the EQR are similar to the findings of Robert and Tran (2012) who presented streamwise turbulence intensity under a simulated rough cover and rough bed. In addition, the results agree with the findings of Parthasarathy and Muste (1994) who presented streamwise turbulence intensity under a simulated smooth cover and rough bed. The turbulence intensities from L2 and L3 have obtained self-similarity.

As flow developed in the UTR (Figure 4-6 (b) and (c)), the turbulence intensity increased close to the upper boundary and the peak value of u_{rms}/U_{max} moved farther away from the top due to accelerating and contracting flow; while, the decelerating and expanding flow in the

LTR (Figure 4-6 (d)) caused the peak value to be located near the upper wall. The highest peak value of u_{rms}/U_{max} occurred at L10 near the toe of the jam, thus, potential for the undersurface erosion of the jam in this area could be high. Downstream of the jam (Figure 4-6 (e)) , since the geometric shape of the upper boundary was the same as the EQR, the turbulence intensity distribution tended to change to that of the EQR.

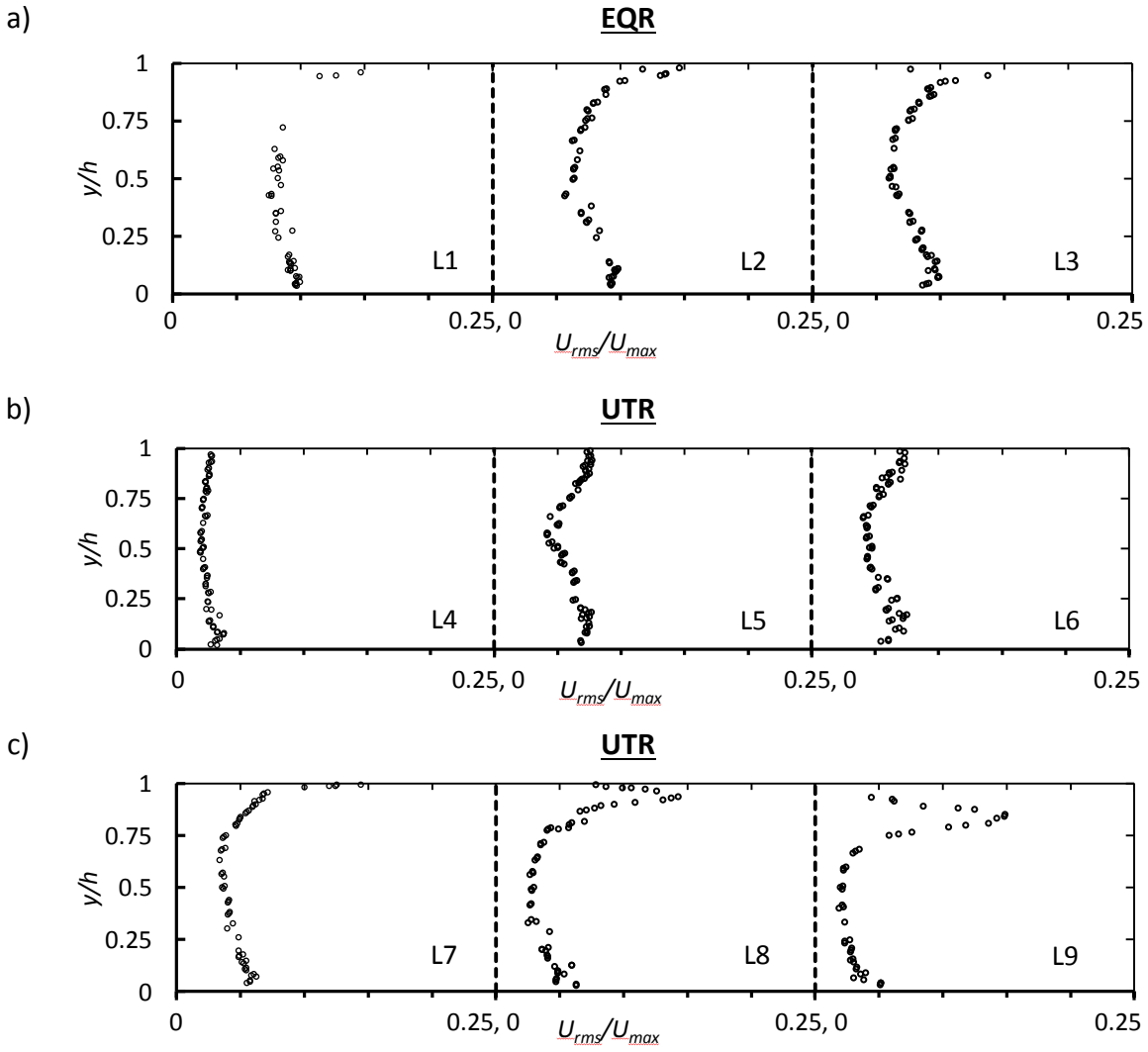

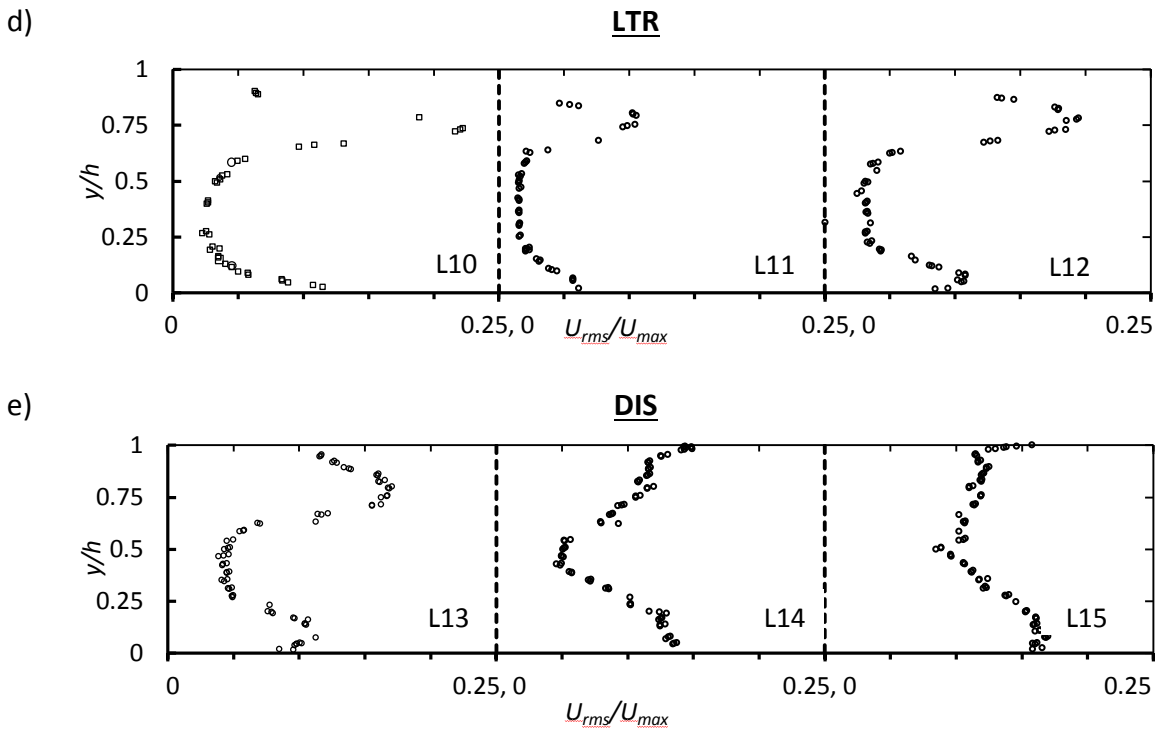

Figure 4-6: Dimensionless streamwise turbulence intensity in the (a) EQR, (b) and (c) UTR, (d) LTR, (e) DIS.

4.2 Scenario 2

4.2.1 Smooth Bed and Smooth Ice Jam

4.2.4.1 *Mean Streamwise Velocity Profiles*

The dimensionless mean streamwise velocity profiles under the simulated ice jam are presented in Figure 4-7 and Figure 4-8. The velocity profiles in the EQR (L2 and L3) are shown in Figure 4-7, where it is clear that the profiles for L2 and L3 are self-similar, demonstrating that the flow became fully developed by position L2. Of note is the fact that the roughness of the top and bottom were identical, and that the flow depth was nearly constant at

30 cm. The velocity profiles therefore showed the expected parabolic shape with a maximum velocity at the mid-depth (Zufelt and Ettema, 1997).

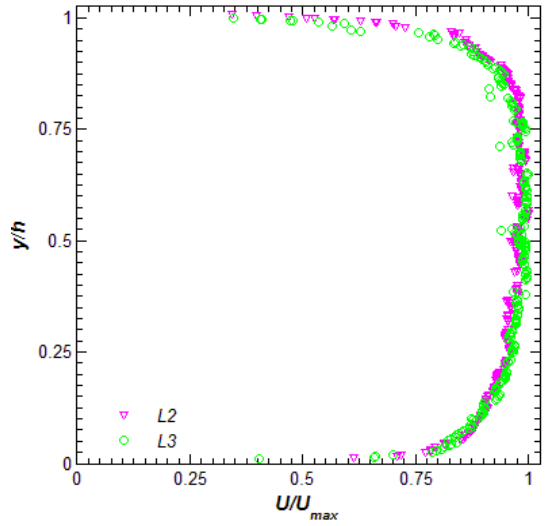

Figure 4-7: Dimensionless streamwise velocity profiles in the EQR- SB&SJ.

The development of the mean streamwise velocity profiles in the UTR, LTR, and DIS are shown in Figure 4-8. As the flow developed in the UTR, the flow area decreased due to the down-sloping ice surface and the streamlines moved more in the downwards direction. So, the streamwise magnitude of the flow velocity as well as the velocity gradient near the upper boundary decreased as the flow contracted. In contrast, close to the lower boundary, the flow velocity and the velocity gradient increased. In addition, the velocity profile of the each location indicated that the velocity gradient near the lower boundary was higher than that of near the upper boundary. It should be noted that the down-sloping geometry causes the velocity distribution to become asymmetric, even though the boundary roughnesses are equal. In this part of the jam, the mean velocity increased compared to the EQR due to the flow area reduction and flow acceleration.

As the flow developed in the LTR, the up-sloping ice surface caused the flow cross sectional area to increase and the streamlines moved more in the upwards direction. In the LTR, the rapid flow deceleration substantially slowed the flow close to the boundaries. Hence, the velocity rapidly decreased near the upper boundary as well as the velocity gradient compared to the UTR due to the flow expansion. Also, the velocity gradient near the lower boundary decreased as the flow developed and reattached to the upper boundary. The velocity gradient near the upper boundary was smaller than that of the lower boundary for each of the measurement locations in the LTR. Again, even though the boundary roughnesses were equal, the up-sloping geometry of the ice surface caused the velocity distribution in the LTR to be asymmetric. It can be seen that as the flow decelerated due to the expansion, discrepancy between the velocity profiles in the LTR and UTR progressively increased. In the LTR, the average velocity decreased due to the flow area increment and flow deceleration.

As the flow developed downstream of the jam (DIS), the flow tendency was to attach to the upper boundary, so the velocity in the upper layer increased, while it decreased in the lower region. In L13, the velocity gradient near the bed was higher than in L15; however, the velocity gradient near the upper boundary of L13 was smaller than in L15. Following L15, if the length of the downstream cover was sufficient, then the flow will tend to redevelop and then the velocity distribution will become symmetric.

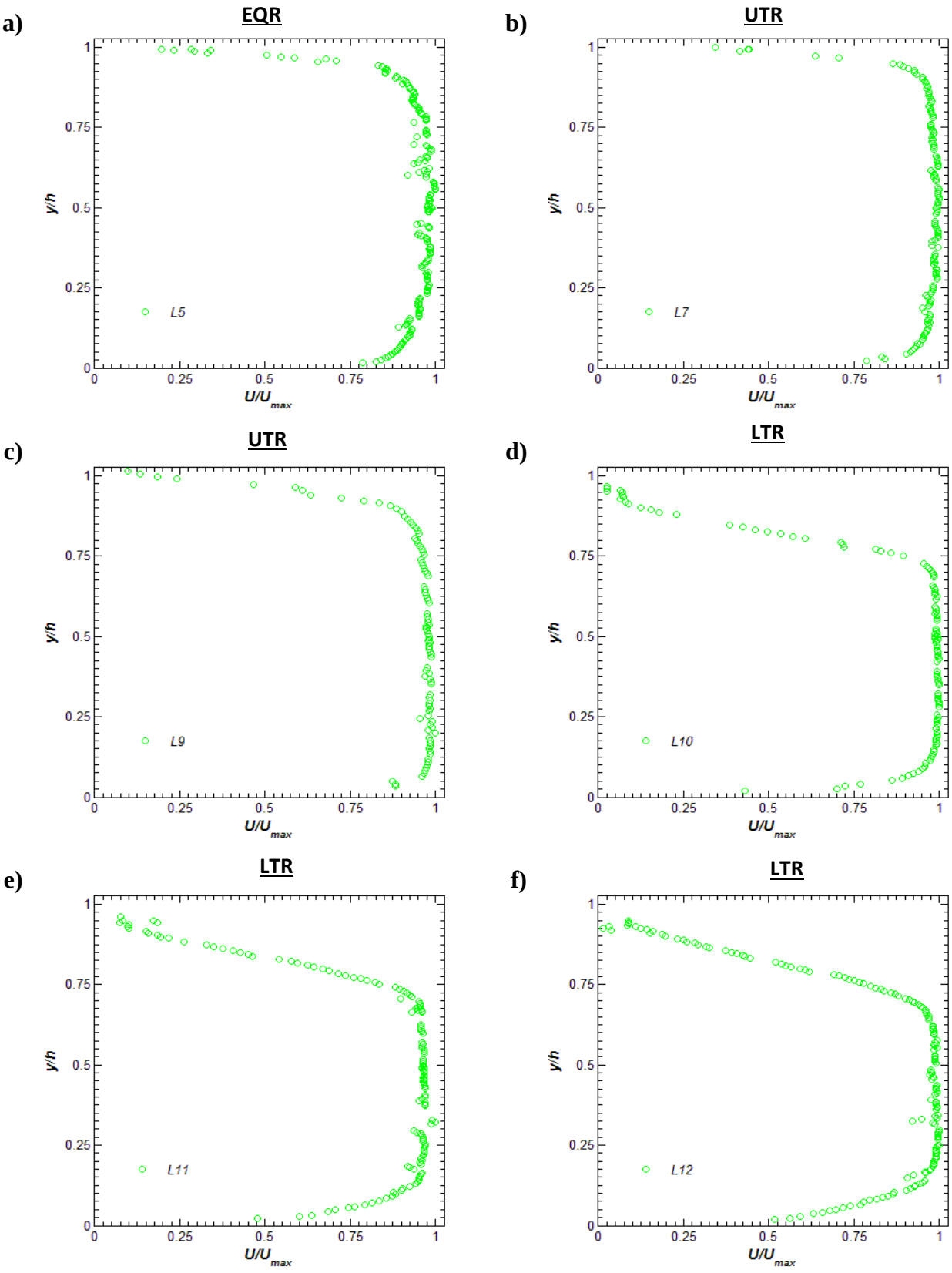
a)
EQR
L5
b)
UTR
L7
c)
UTR
L9
d)
LTR
L10
e)
LTR
L11
f)
LTR
L12
y/h
U/U max
0
0.25
0.5
0.75
1

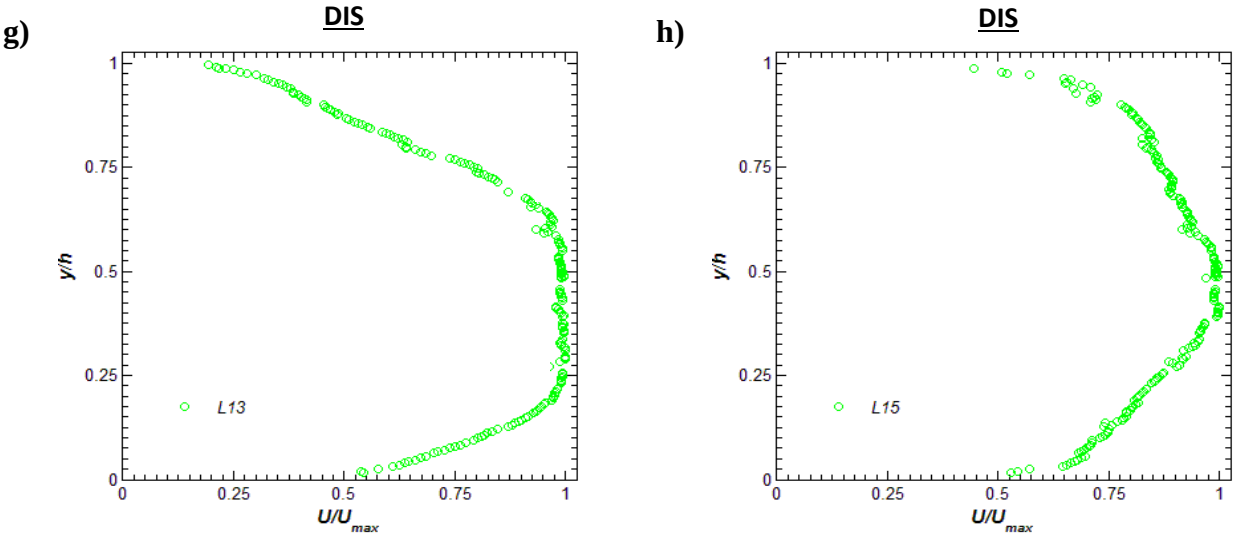

Figure 4-8: Dimensionless streamwise velocity profiles in the UTR (a, b, and c), LTR (d, e, and f), and DIS (g and h) - SB&SJ.

A summary of all the streamwise velocity profiles beneath the ice jam at different locations is exhibited in Figure 4-9.

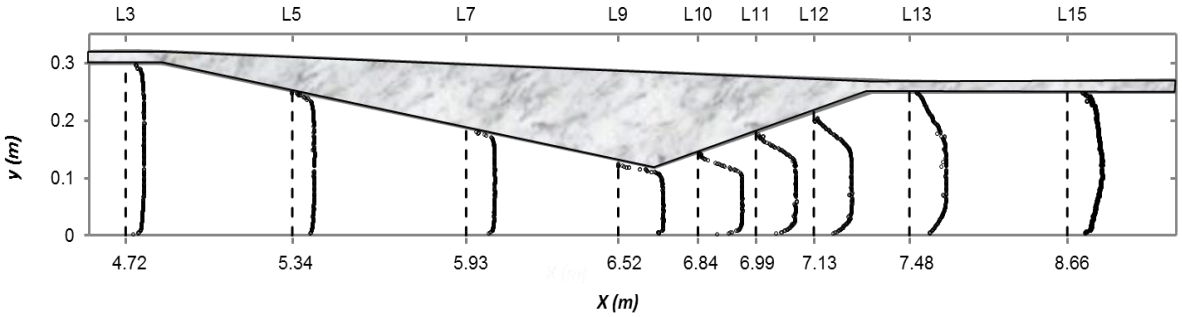

Figure 4-9: Centerline streamwise velocity profiles at various locations under the ice jam- SB&SJ.

4.2.4.2 ***Streamwise Turbulence Intensity Distributions***

The normalized mean streamwise turbulence intensities (u_{rms}/U_{max}) are plotted against the dimensionless flow depth (y/h) for each of the velocity measurement locations in Figure 4-10. In the EQR, the turbulence intensity adjacent to the upper and lower boundary increased and then decreased away from the boundaries.

In the UTR, as the flow developed downstream, the effect of the upper boundary on the turbulence intensity distribution increased. The peak value of (u_{rms}/U_{max}) occurred close to the upper boundary and decreased rapidly away from the boundary. The high turbulence intensity near the ice cover would increase turbulent mixing and heat transfer which could promote melting of the underside of the cover, thereby decreasing the jam roughness. In this region, the overall average of the turbulence intensity is less than the EQR due to the flow acceleration. Although the near-bed velocities and bed shear stresses have been both shown to increase near the jam toe – thereby promoting bed erosion - the average streamwise turbulence intensities in this region are actually less than in the EQR. The average of the normalized turbulence intensity at L9 decreased by 51% compared to L3 located in the EQR.

In the LTR, the peak value at L10 was much larger than the peak value at L9 and it moved farther from the upper boundary in comparison with L9. Thus, there could be a greater potential for surface erosion in this area compared to L9. As the flow developed in this region, the peak value moved towards the upper boundary due to the decelerating and expanding flow.

In the DIS, the effect of the upper boundary on the turbulence intensity distribution decreased as far as it changed to resemble that of the EQR upstream. The average of the normalized turbulence intensity in this region was higher than the other locations along the jam.

a)

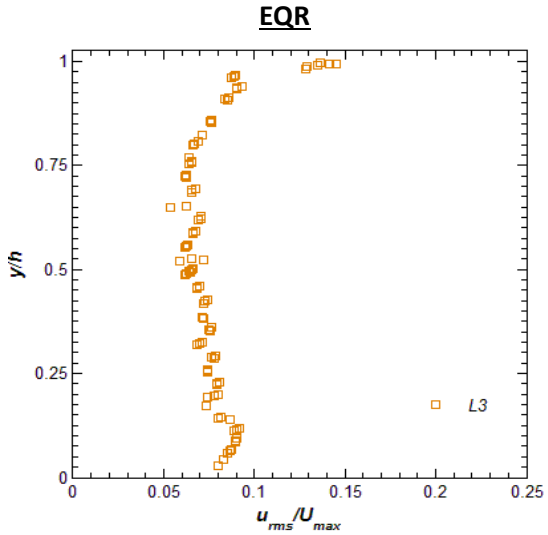
EQR
y/h
u_{rms}/U_{max}
L3

b)

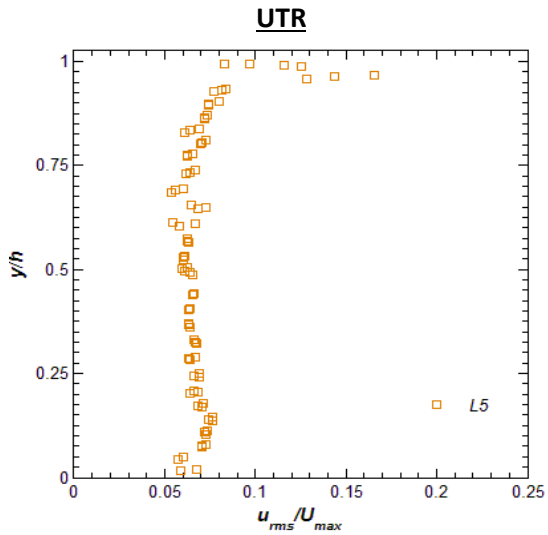
UTR
y/h
u_{rms}/U_{max}
L5

c)

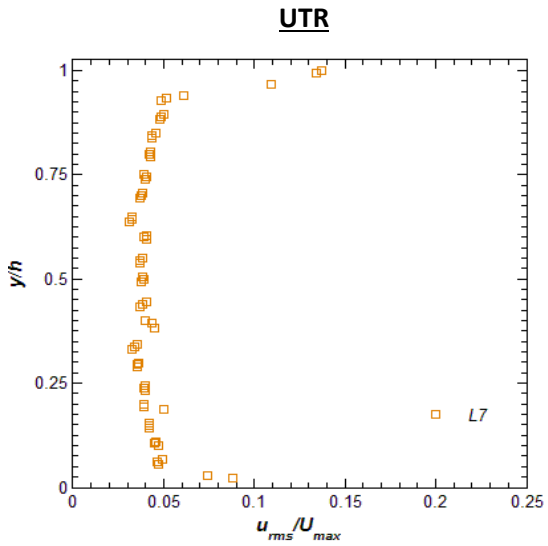
UTR
y/h
u_{rms}/U_{max}
L7

d)

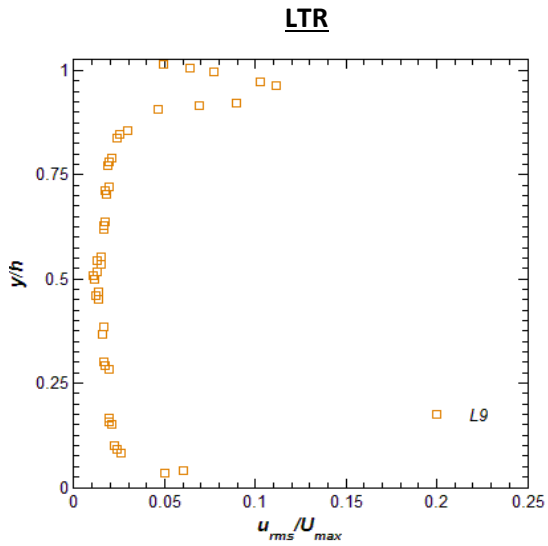
LTR
y/h
u_{rms}/U_{max}
L9

e)

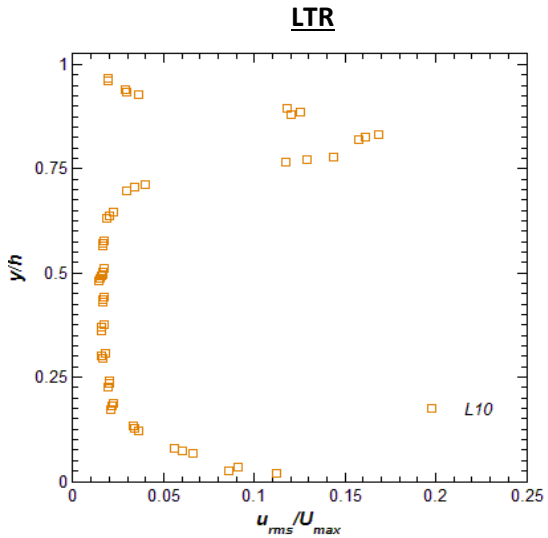
LTR
y/h
u_{rms}/U_{max}
L10

f)

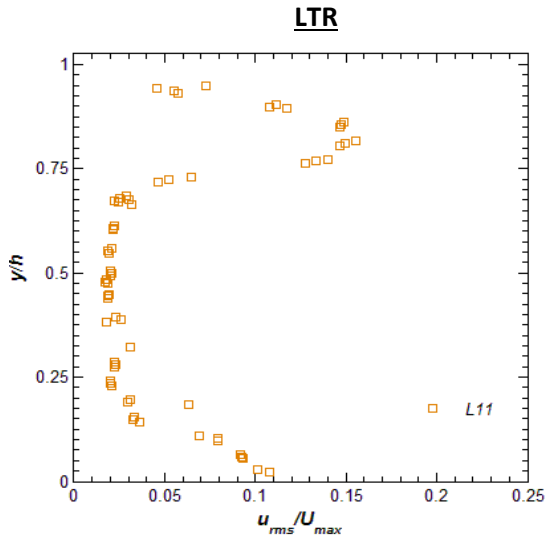
LTR
y/h
u_{rms}/U_{max}
L11

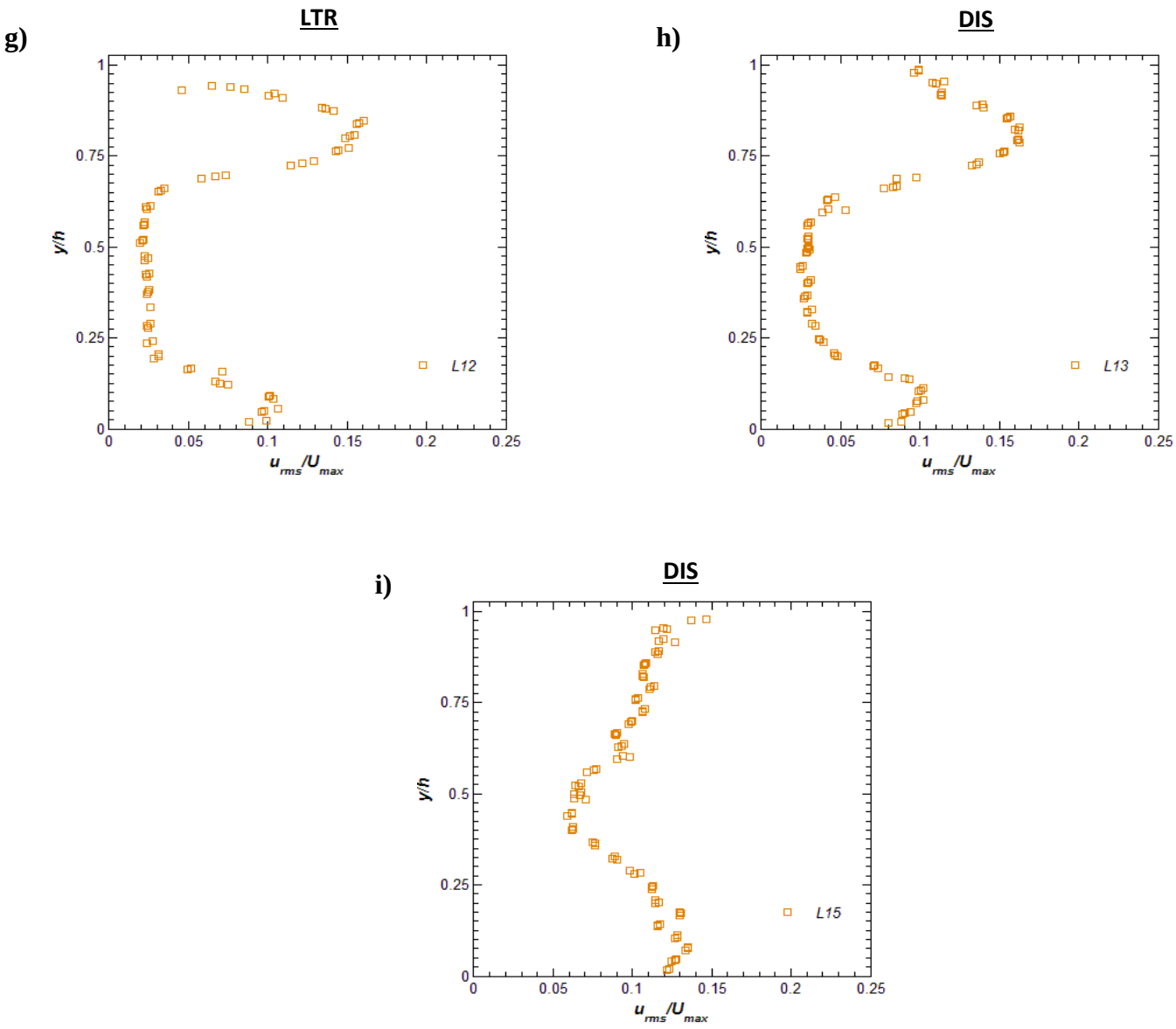

Figure 4-10: Turbulence intensity distributions in the EQR (a), UTR (b, c, and d), LTR (e, f, and g), and DIS (h and i) - SB&SJ.

4.2.2 Smooth Bed and Rough Ice Jam

4.2.2.1 Mean Streamwise Velocity Profiles

The normalized mean streamwise velocity (U/U_{max}) profiles under condition of the rough ice jam and the smooth bed are presented in Figure 4-11 and Figure 4-12. As Figure 4-11 indicates, in the EQR the flow became fully developed by position L2 because the velocity profiles of L2 and L3 are equal. Since the boundary roughnesses were not equal and the top boundary was rougher than the bottom, the velocity profiles were not symmetric and the maximum streamwise velocity occurred near the smooth boundary (Tatinclaux and Gogus, 1983) which was the bed in this case. Also, it is clear from Figure 4-11 that the existence of the rough ice jam caused the streamwise velocity magnitude to rapidly decrease near the upper boundary.

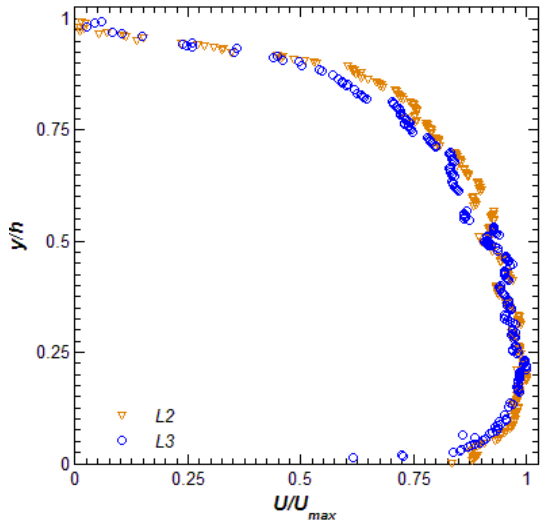

Figure 4-11: Dimensionless streamwise velocity profiles in the EQR- SB&RJ.

As the flow contracted in the UTR, the effects of both the roughness and geometry of the top boundary caused the streamlines to move much in the downwards direction compared to the smooth top boundary in Test SB&SJ. Thus, the velocity gradient in the approximately top quarter of the flow depth decreased extremely. For L9, the velocity has a distinct-S shape near the upper boundary with a zone of low velocity due to the presence of the rough jam; however, the velocity gradient near the bed increased in the UTR. Similar to Test SB&SJ, the mean velocity in the UTR was higher than that in the EQR.

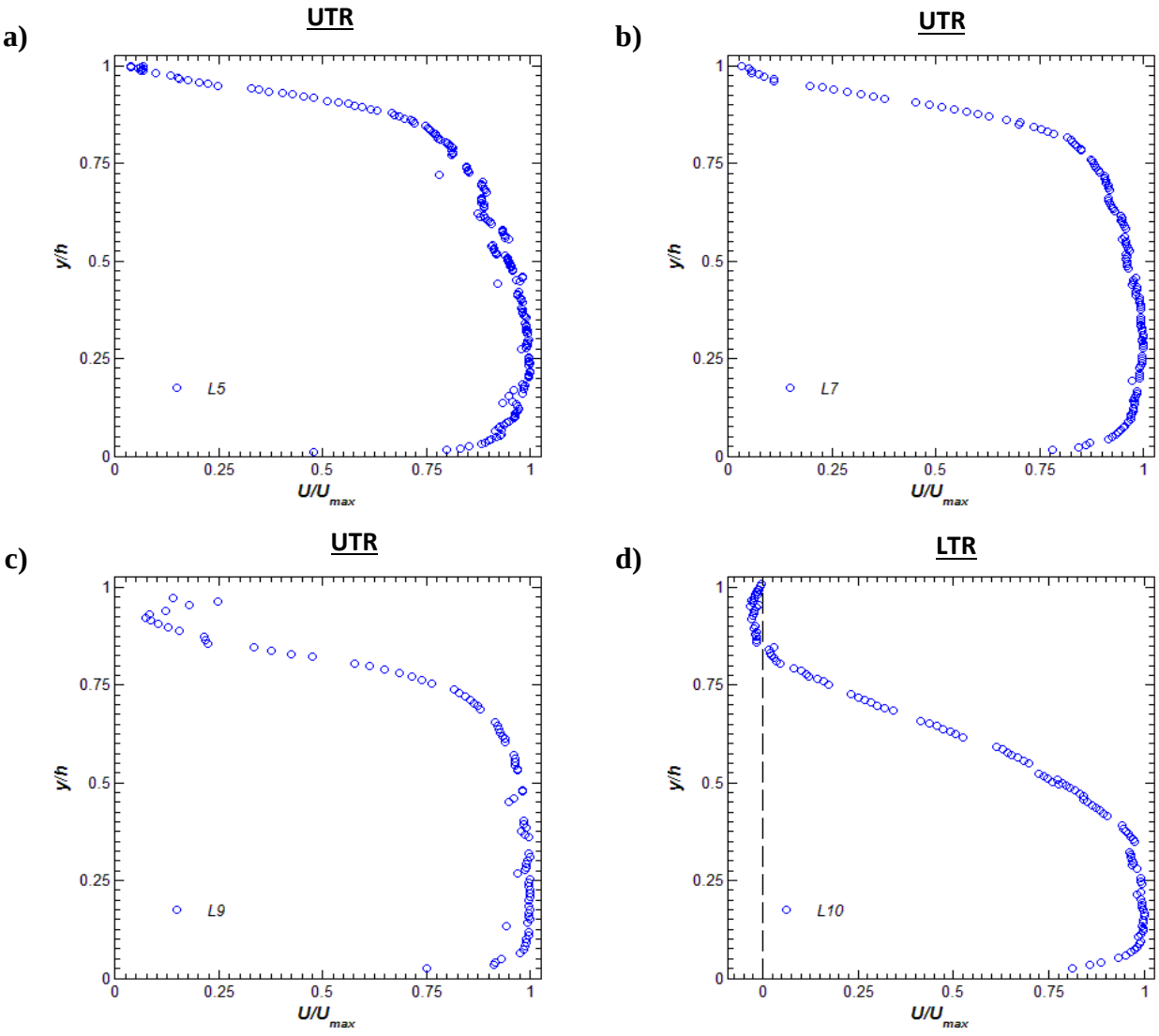

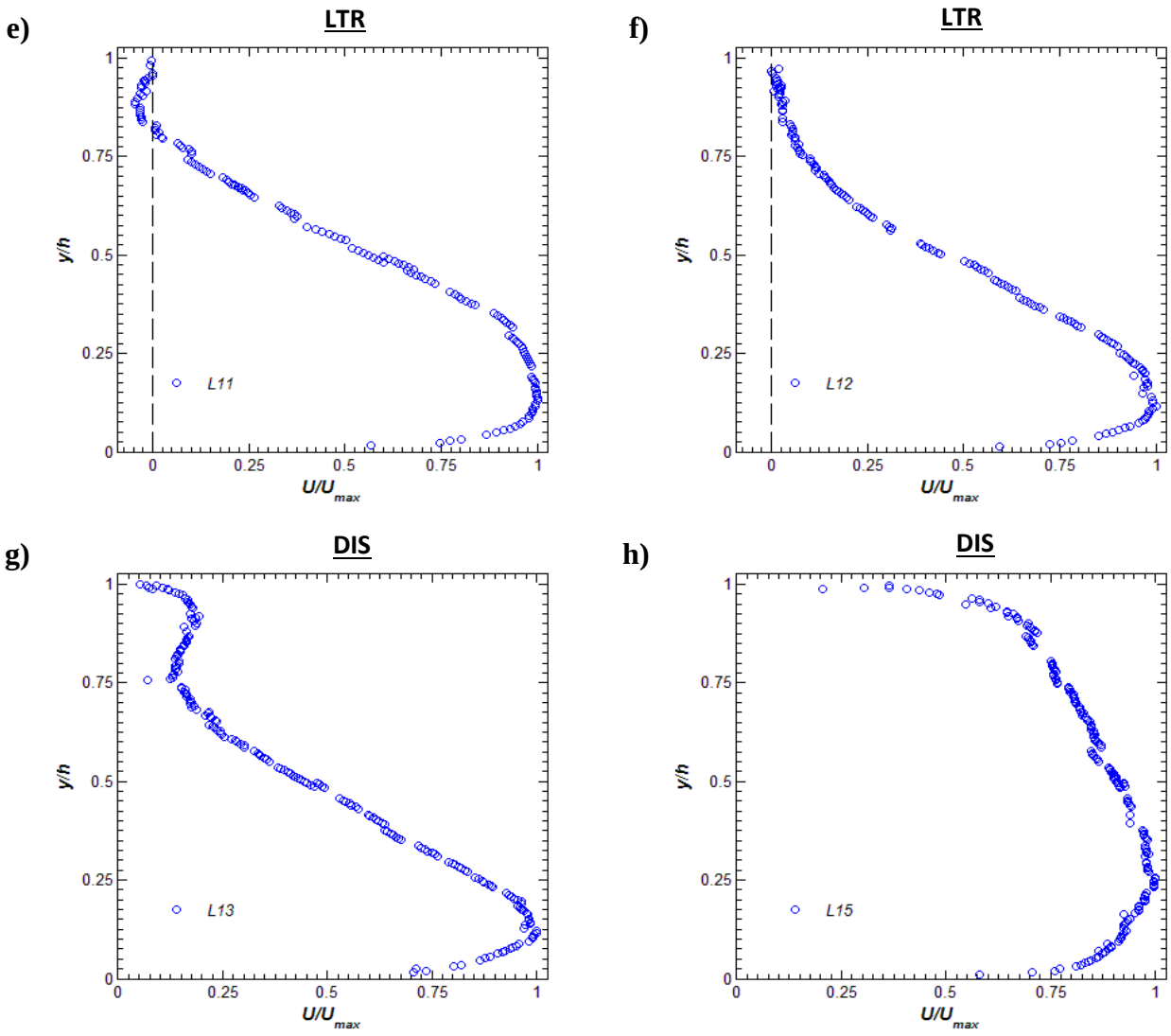

Figure 4-12: Dimensionless streamwise velocity profiles in the UTR (a, b, and c), LTR (d, e, and f), and DIS (g and h) - SB&RJ.

In the LTR, as expected, flow expanded because of the increasing cross sectional area. In this region, significant variation was observed in the velocity profiles close to the top boundary. As Figure 4-12 (d), (e), and (f) indicated, the magnitude of streamwise velocity reduced in the upper layer due to the presence of the rough elements undersurface of the ice jam. Negative velocities near the upper boundary were observed for L10, L11, and L12,

indicating a flow separation zone due to the rough jam. In general, in the flow separation zone, fluid recirculates and moves both in the downstream direction and in the opposite direction, which is often referred to as a separation bubble. The flow separation zone is a region between the start point of flow separation and the end point where the flow reattaches onto the boundary (Kiya and Sasaki, 1983). For L12, the streamwise velocity was zero near the upper boundary, indicating the profile was at the end of the recirculation zone. As the flow expanded in the LTR, the maximum backflow was approximately 0.05 U_{max} and almost covered 18% of the flow depth, near the upper boundary. Also, the average velocity decreased as the water decelerated in the LTR.

As the flow developed downstream of the jam, in the DIS, the velocity profile changed significantly due to the variation of the roughness and the slope of the upper boundary. Of note that in the DIS, the roughness and geometry of the upper boundary were the same as the bed, smooth and parallel with the bed. Hence, the velocity in the upper layer increased rapidly from L13 to L15 to attach to the smooth upper boundary, while it decreased in the lower layer. For L13, there was an unexpected variation of velocity profile in the top quarter of the flow depth so that the velocity initially increased and then decreased. Since L13 was almost located immediately at the end of the LTR, the flow was affected by the recirculation zone that happened after L12. Consequently, the flow accelerated near the top boundary and the velocity increased in this region. Following L15, if the length of the downstream cover was sufficient, then the flow will tend to redevelop and the velocity profile will be symmetric due to an equal roughness of the upper and lower boundary. A summary of all the streamwise velocity profiles beneath the ice jam at different locations is presented in Figure 4-13.

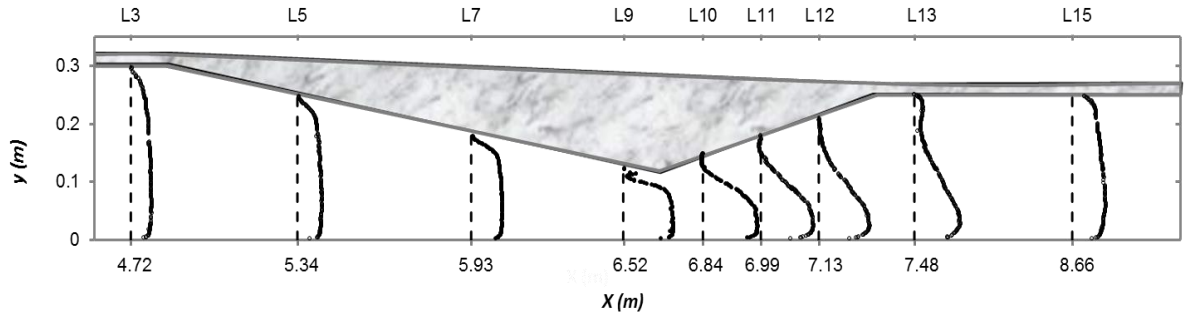

Figure 4-13: Streamwise velocity profiles at various locations under the ice jam-SB&RJ.

4.2.2.2 Streamwise Turbulence Intensity Distributions

The effect of the rough ice jam on the streamwise turbulence intensities is shown in Figure 4-14. The rough ice jam had a significant effect on the turbulence intensity in the upper layer. For each of the measurement locations in the EQR and UTR, the turbulence intensity gradually decreased with increasing flow depth and then substantially increased until reaching its maximum value near the top boundary. As the flow accelerated in the UTR, the maximum value of the normalized streamwise turbulence intensity, $(u_{rms}/U_{max})_{max}$, increased so that the peak value of u_{rms}/U_{max} at L9 enhanced by 36% compared to L3 which was located in the EQR. As the flow decelerated in the LTR, the peak value of u_{rms}/U_{max} moved farther from the upper boundary in comparison with the UTR. The reason may be attributed to the presence of stronger vortices near the upper boundary in the LTR compared to the UTR. As the flow redeveloped in the smooth intact ice sheet downstream of the ice jam, these relatively large vortices will be broken into smaller vortices near the upper boundary. If the length of the downstream cover is sufficient, the turbulence intensity distributions will tend to return to that in the EQR of Test SB&SJ.

a)

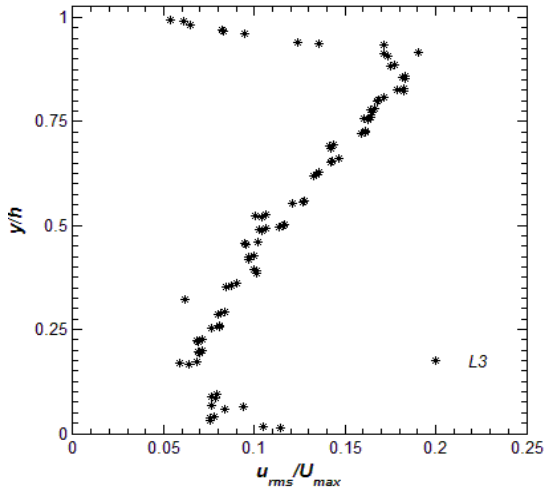
EQR
y/h
u_{rms}/U_{max}
L3

b)

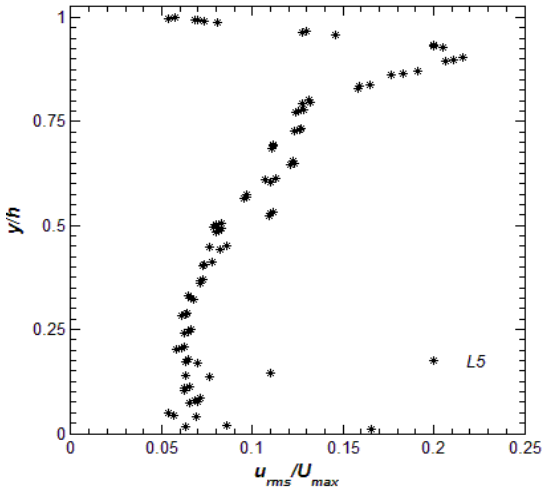
UTR
y/h
u_{rms}/U_{max}
L5

c)

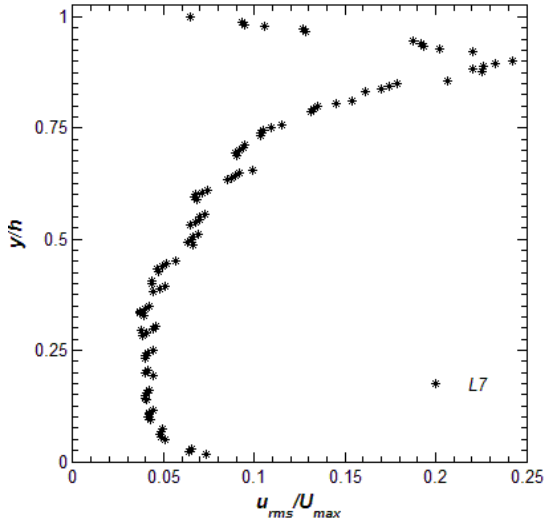
UTR
y/h
u_{rms}/U_{max}
L7

d)

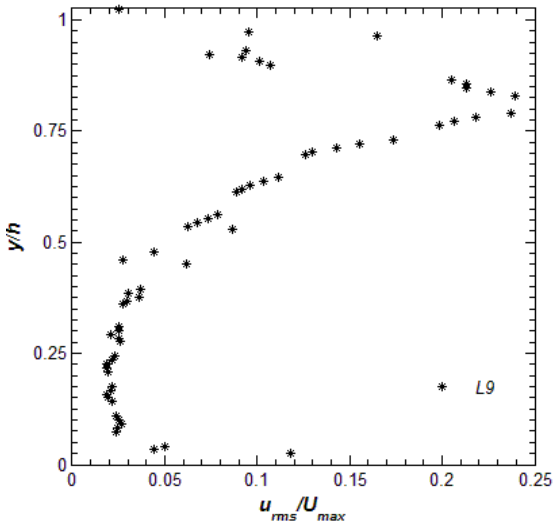
UTR
y/h
u_{rms}/U_{max}
L9

e)

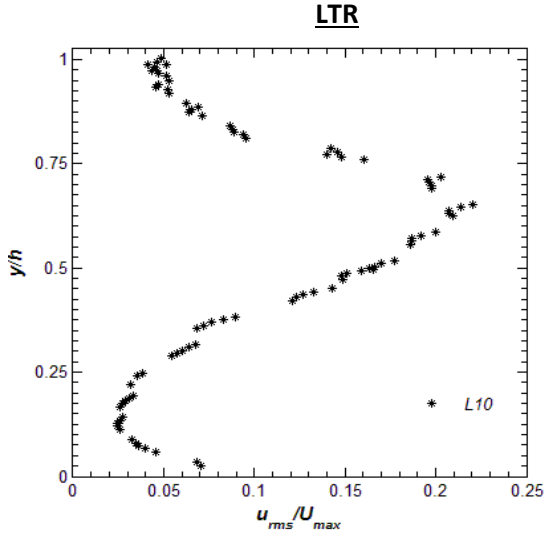
LTR
y/h
u_{rms}/U_{max}
L10

f)

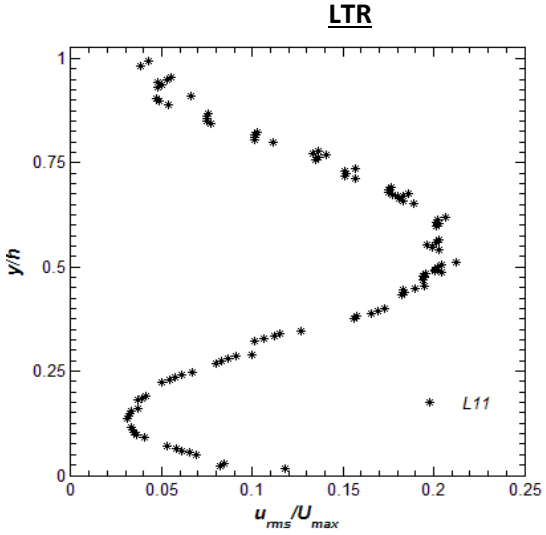
LTR
y/h
u_{rms}/U_{max}
L11

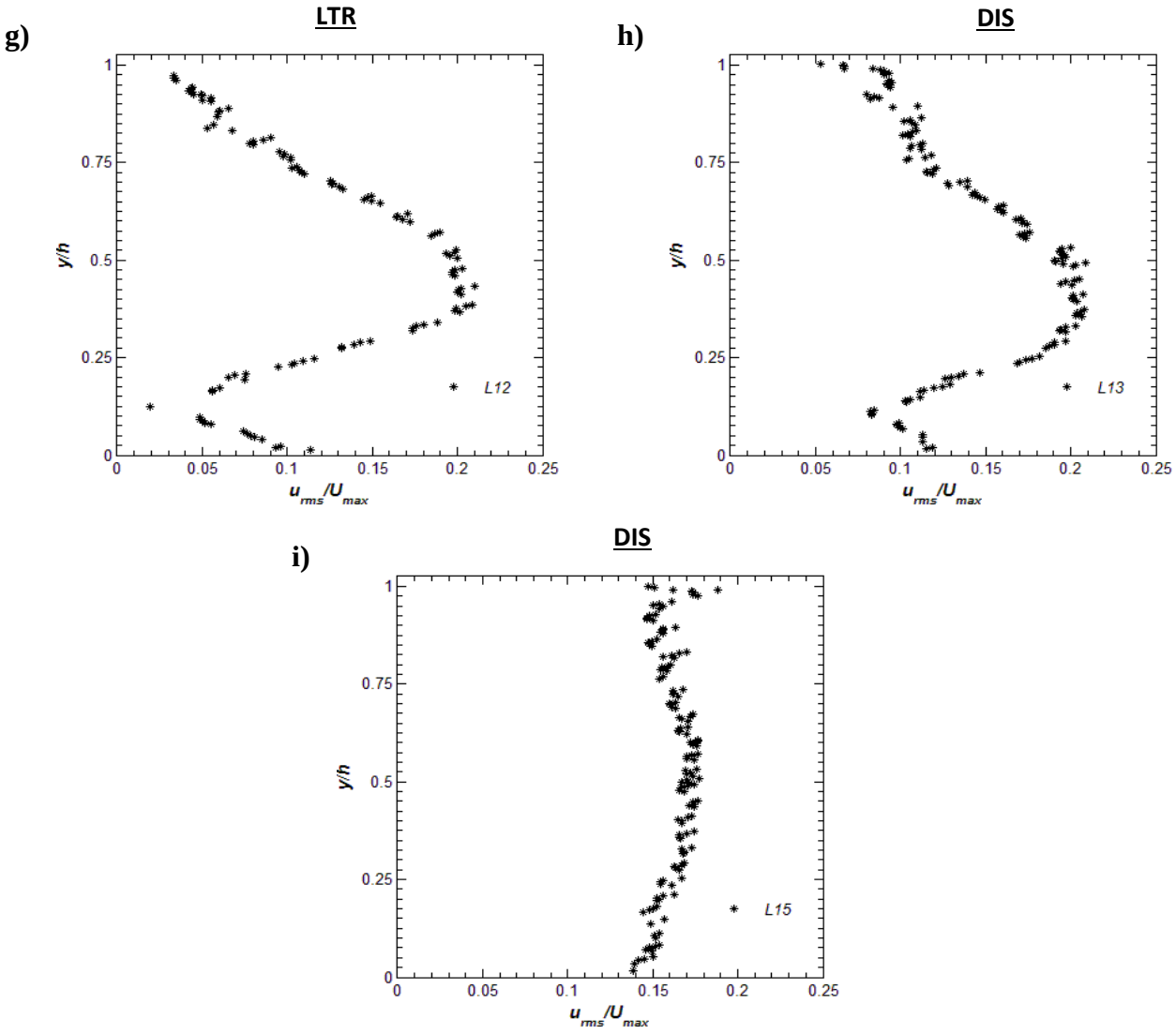

Figure 4-14: Turbulence intensity distributions in the EQR (a), UTR (b, c, and d), LTR (e, f, and g), and DIS (h and i) - SB&RJ.

4.2.3 Rough Bed and Rough Ice Jam

4.2.3.1 Mean Streamwise Velocity Profiles

Figure 4-15 and Figure 4-16 exhibit the dimensionless profiles of the mean streamwise velocity under condition of the rough ice jam and the rough bed. Figure 4-15 shows that the velocity profiles of L2 and L3 remained unchanged, indicating the flow became fully developed by position L2. In the fully developed region of the EQR, the velocity profiles were symmetric because the roughness of the top boundary was the same as the bottom boundary (Parthasarathy and Muste, 1994).

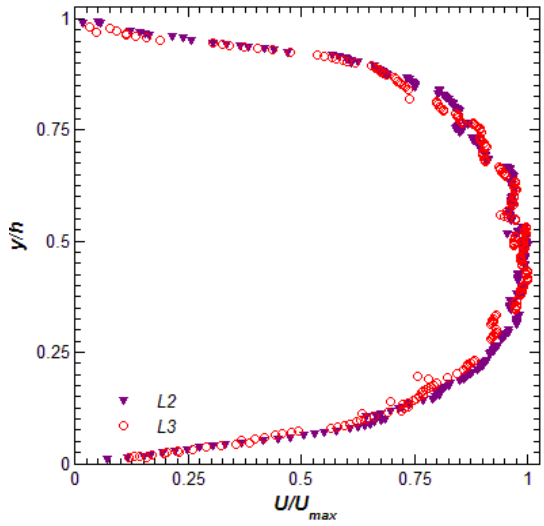

Figure 4-15: Dimensionless streamwise velocity profiles in the EQR- RB&RJ.

As the flow contracted in the UTR, the rough top boundary and the additional boundary roughness; the rough bed, caused the majority of the flow to be forced away from the rough top and rough bottom boundary towards the central portion of the channel. So, the velocity gradient near the upper boundary greatly decreased as well as near the lower boundary.

In the LTR, it is clear from the velocity profiles that the flow separated near the upper boundary where negative streamwise velocities were observed, indicating the presence of a small recirculation region. There was an exception near the jam toe (L9, L10, L11, and L12), where the increased shear stresses on the flume bed actually caused the roughness elements on the bed to become detached. This is why the rough bed flow velocities near the bed at these locations are similar to the corresponding smooth case. Unfortunately this was not detected until well after all experiments were completed and disassembled.

As the flow developed in the DIS, the velocity gradient increased in the lower layer and the velocity magnitude increased in the upper layer to attach to the upper boundary. In L13, the flow accelerated near the top boundary similar to Test SB&RJ but with lower effect compared to the SB&RJ because of the larger recirculation zone. Following L13, if the flow depth was constant and the length of the downstream cover was sufficient, then the flow would tend to redevelop.

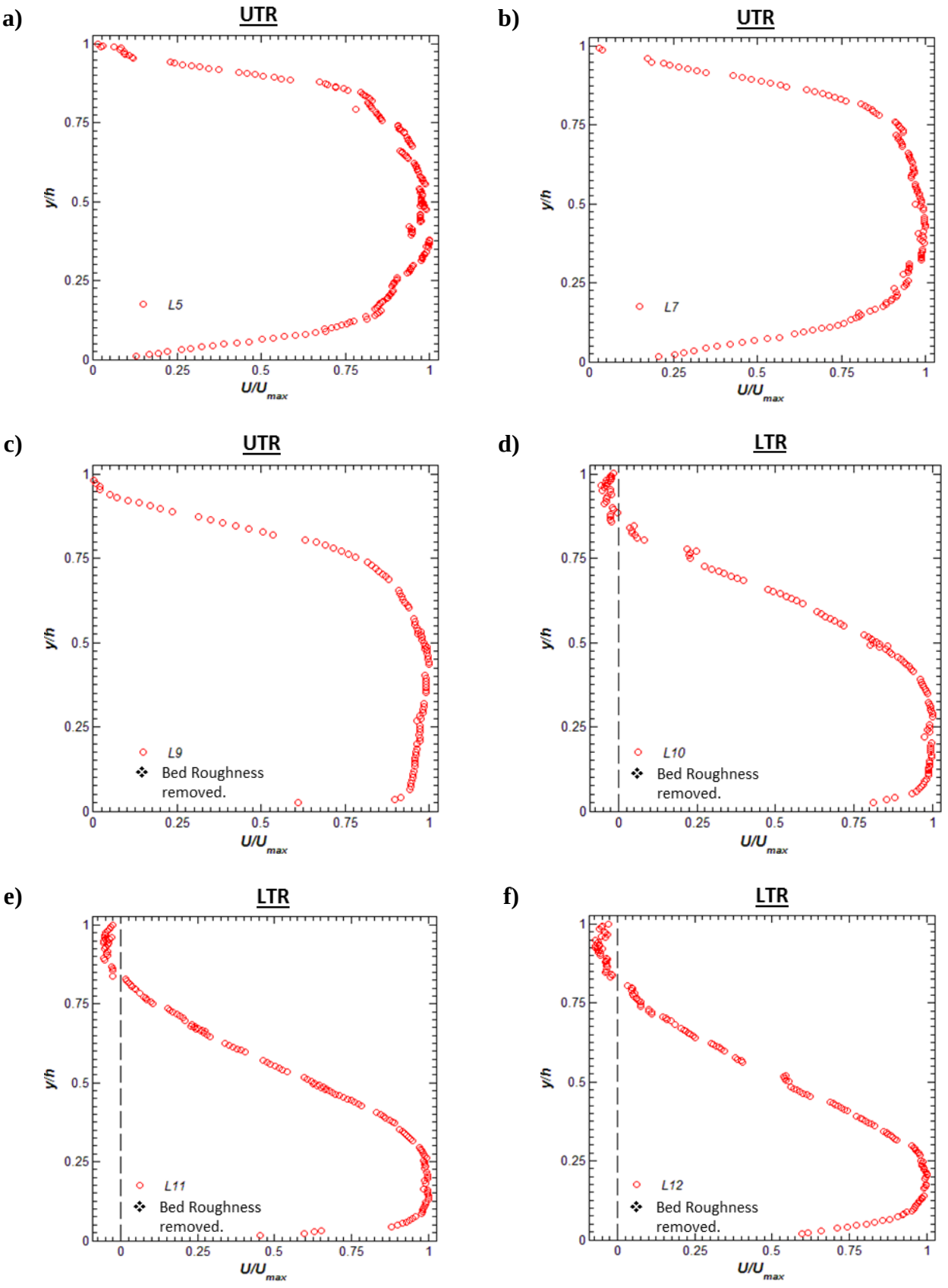
a)
UTR
y/h
U/U max
L5
b)
UTR
y/h
U/U max
L7
c)
UTR
y/h
U/U max
L9
❖ Bed Roughness removed.
d)
LTR
y/h
U/U max
L10
❖ Bed Roughness removed.
e)
LTR
y/h
U/U max
L11
❖ Bed Roughness removed.
f)
LTR
y/h
U/U max
L12
❖ Bed Roughness removed.

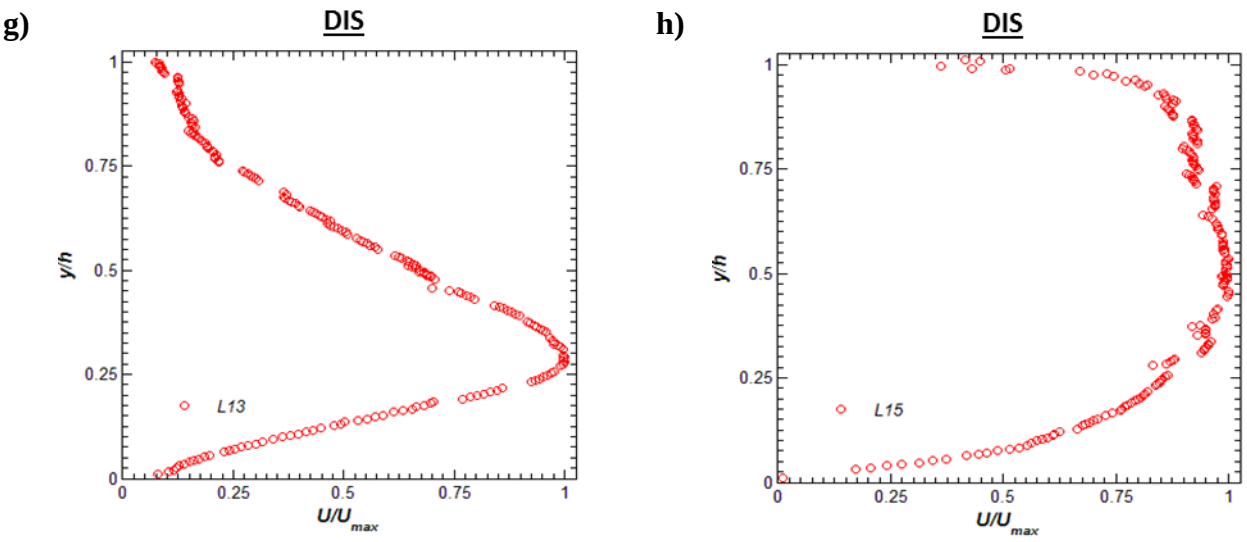

Figure 4-16: Dimensionless streamwise velocity profiles in the UTR (a, b, and c), LTR (d, e, and f), and DIS (g and h) - RB&RJ.

A summary of all streamwise velocity profiles beneath the ice jam at different locations is presented in Figure 4-17.

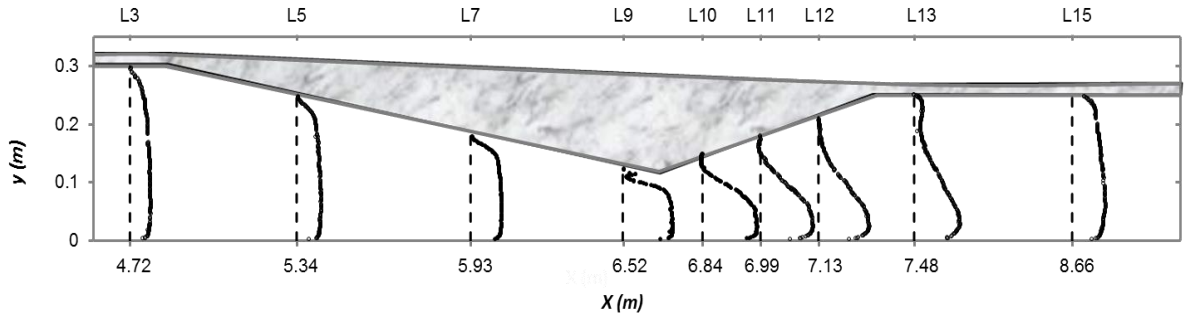

Figure 4-17: Streamwise velocity profiles at various locations under the ice jam-RB&RJ.

4.2.3.2 Streamwise Turbulence Intensity Distributions

The streamwise turbulence intensities for the rough bed and rough ice jam are plotted in Figure 4-18. In the EQR, the maximum turbulence intensity occurred near the rough top and

rough bottom boundary, while the relative minimum value was observed at mid-depth. Since the boundaries roughness was identical, the turbulence intensity profile was symmetric in the EQR.

As the flow developed in the UTR, the turbulence intensity increased near the boundary; the enhancement was more near the top boundary than the bottom boundary. The peak value of u_{rms}/U_{max} happened at L9 near the rough upper boundary. As mentioned earlier, some of the rough elements were removed from the bed near the jam toe (L9, L10, L11, and L12), thereby the effect of rough bed on the turbulence intensity in these locations cannot be seen in the related profiles. So, the turbulence intensities in these locations had the same distribution as those of in Test SB&RJ.

In the DIS, the average of the turbulence intensity increased near the rough bottom boundary and decreased near the smooth boundary. In L13, the turbulence intensity distribution had a quasi-zigzag shape with two peak values in the lower and upper layers. Due to the high velocity gradient near the bed, the first peak value of the u_{rms}/U_{max} occurred near the bed while the second one occurred due to the high velocity gradient in the upper layer. However, the minimum value of the turbulence intensity was observed far away from the bed and upper boundary due to the zero velocity gradient.

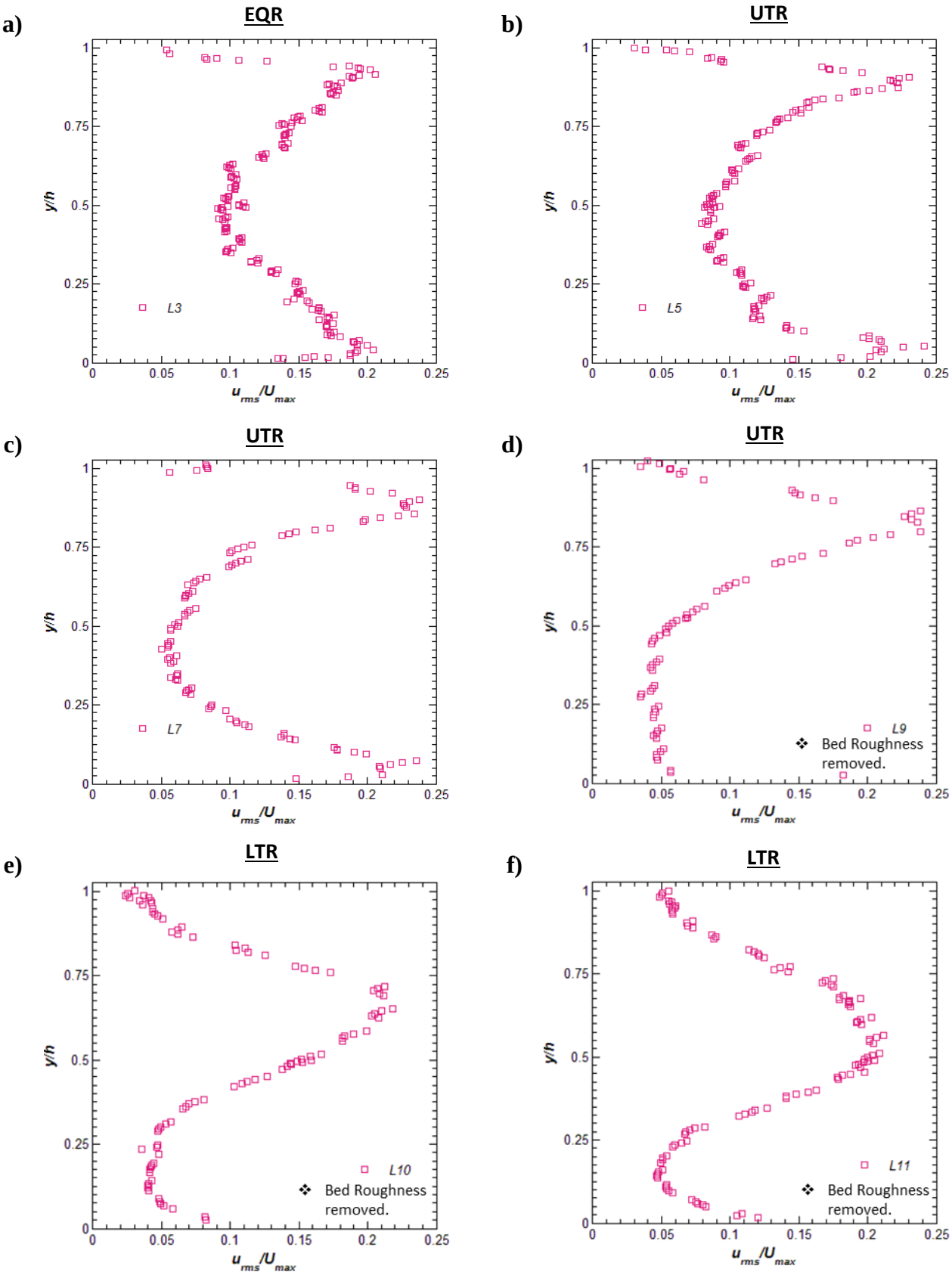
a)
EQR
y/h
u_{rms}/U_{max}
L3
b)
UTR
L5
c)
UTR
L7
d)
UTR
L9
Bed Roughness removed.
e)
LTR
L10
Bed Roughness removed.
f)
LTR
L11
Bed Roughness removed.

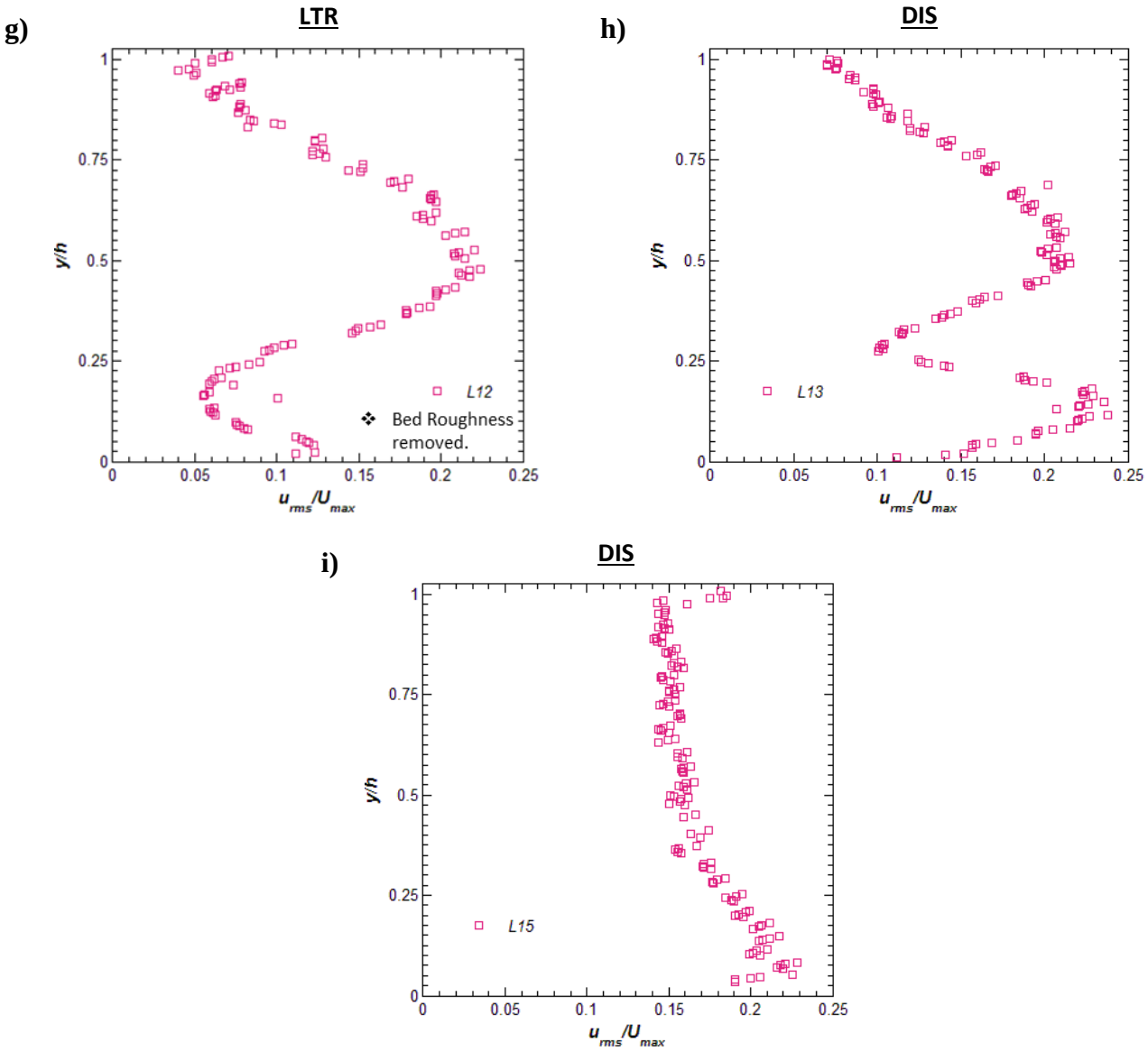

Figure 4-18: Turbulence intensity distributions in the EQR (a), UTR (b, c, and d), LTR (e, f, and g), and DIS (h and i) - RB&RJ.

4.2.4 Comparison of Results

In this section, only the results of scenario 2 for various boundary roughness ratios were compared together, because as mentioned earlier, scenario 2 was an extension of scenario 1. For scenario 2, the ice jam setup was more similar to a real ice jam compared to scenario 1. Also, the acrylic boxes were used at the measured locations for scenario 2 but, not for scenario 1, caused the measured velocity and turbulence intensity near the undersurface of the ice jam to be affected by open flow condition at the measured locations in scenario 1. Hence, the results of scenario 1 were not compared to scenario 2.

4.2.4.1 Mean Streamwise Velocity Profiles

Figure 4-19 shows a comparison of the normalized streamwise velocity profiles under three different roughness ratios of the bed to ice jam at various streamwise locations under the simulated jam. The comparison indicated that the presence of the rough ice jam caused the velocity to decrease greatly in the upper layer with respect to the smooth ice jam; the reduction was more considerable when the flow was expanded. Negative velocities can be seen in the expanded region due to the introduction of the rough ice jam. This indicted recirculation zones near the top rough boundary, whereas there were no recirculation zones near the smooth top boundary. The maximum backflow for L10 and L11 was approximately 3.3% and 4.7% of the local maximum velocity, respectively. Note that the ADV's probe was located at middle space between the ribs, undersurface of the rough jam in the LTR. Similar to the rough ice jam, the rough bed caused the velocity to be reduced in the bed-affected region compared to the smooth bed however; there was an exception near the toe of the jam where the bed roughness elements were removed. It would be anticipated that if the roughness elements had not been removed from the bed near the toe of the jam, the velocity

near the rough bed would be considerably decrease in comparison with the smooth bed. However, the maximum backflow would increase and the recirculation zone would be stronger compared to the smooth bed. Also, the maximum velocity would be located farther from the rough bed compared to the smooth bed.

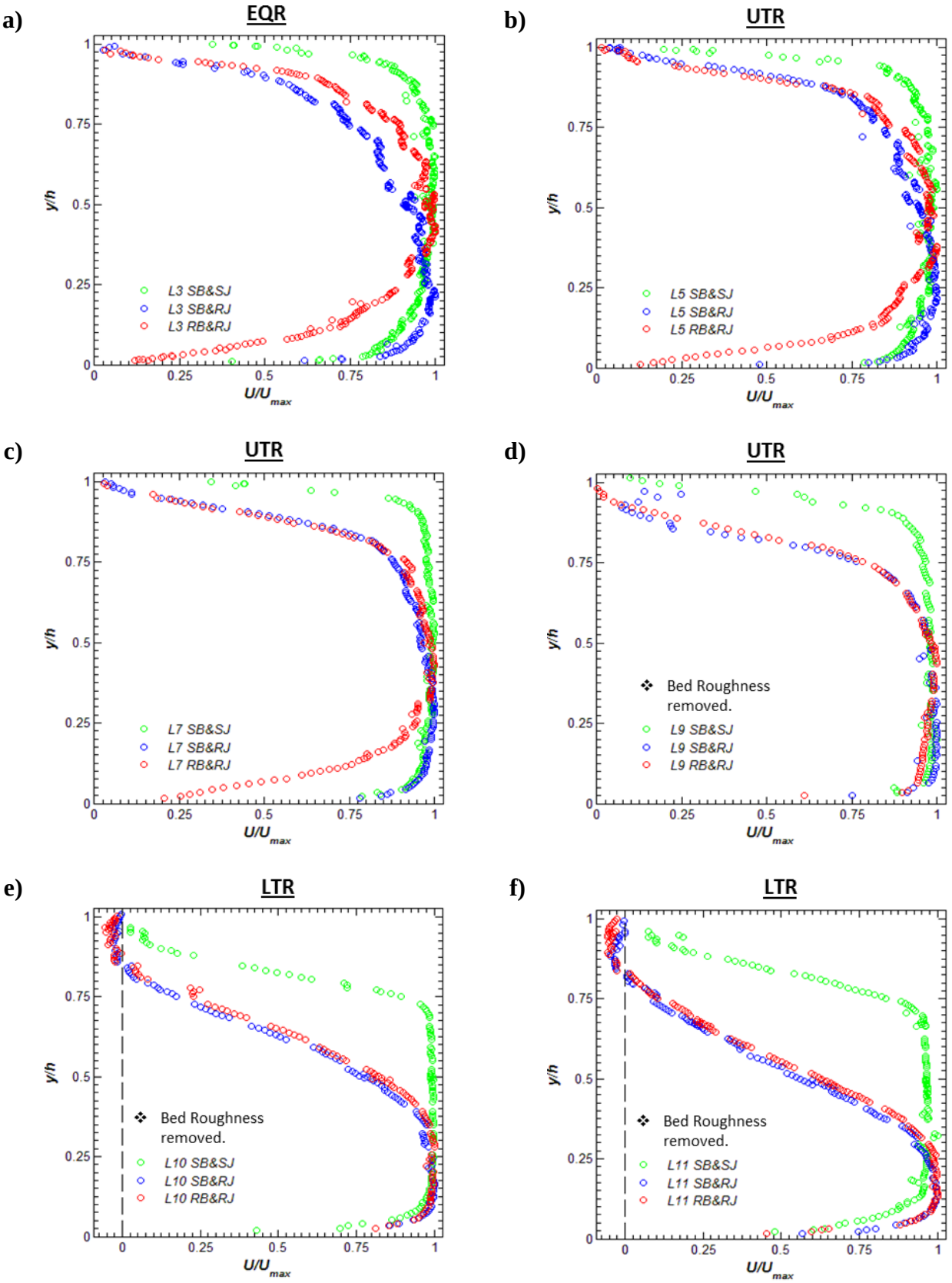
a)
EQR
y/h
U/U max
L3 SB&SJ
L3 SB&RJ
L3 RB&RJ
b)
UTR
L5 SB&SJ
L5 SB&RJ
L5 RB&RJ
c)
UTR
L7 SB&SJ
L7 SB&RJ
L7 RB&RJ
d)
UTR
Bed Roughness removed.
L9 SB&SJ
L9 SB&RJ
L9 RB&RJ
e)
LTR
Bed Roughness removed.
L10 SB&SJ
L10 SB&RJ
L10 RB&RJ
f)
LTR
Bed Roughness removed.
L11 SB&SJ
L11 SB&RJ
L11 RB&RJ

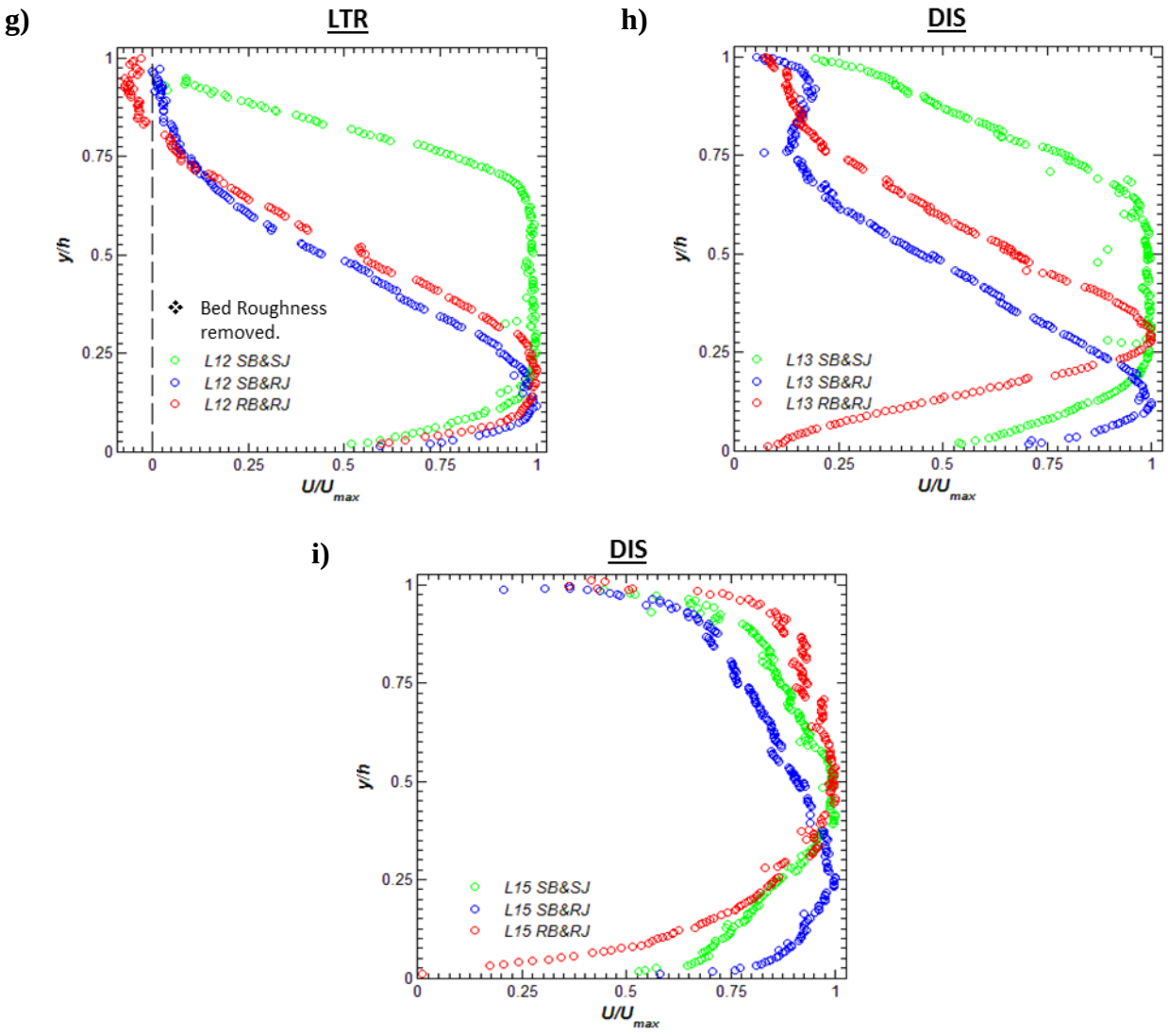

Figure 4-19: Comparison of streamwise velocity profiles for varying bed and ice jam roughness in the EQR (a), UTR (b, c, and d), LTR (e, f, and g), and DIS (h and i).

4.2.4.2 Vector Plots

The flow velocity vectors beneath the ice jam at the measurement locations are plotted in Figure 4-20 for the various boundary roughness ratios. The magnitude variation of the velocity vectors indicated the flow velocity was high near the jam toe. The downwards direction of the velocity vectors in the UTR showed the flow was convergent, while the

upwards direction of the velocity vectors in the LTR indicated the flow was divergent. Near the undersurface of the rough ice jam, in the LTR, the small magnitudes of the velocity vectors with reverse directions indicated that a recirculation zone was present in this region.

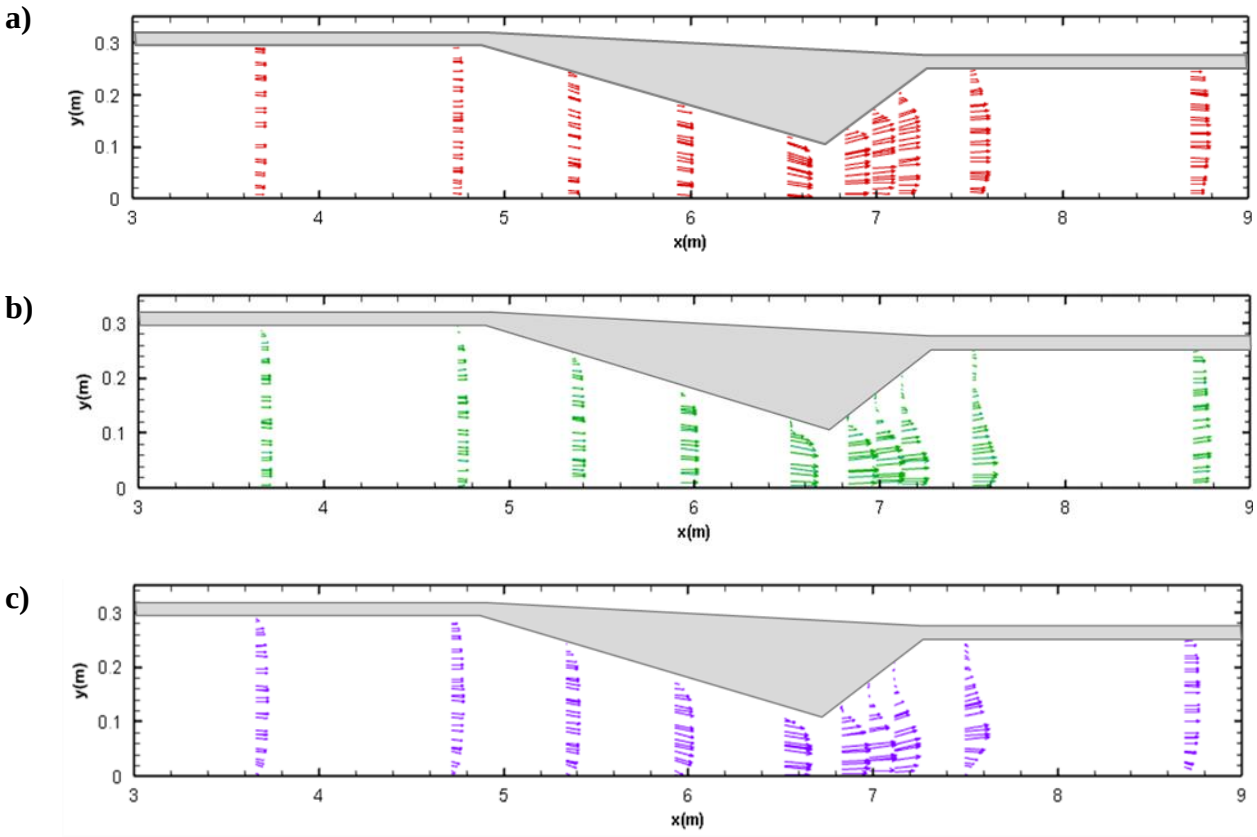

Figure 4-20: Vector velocity profiles beneath the ice jam a) SB&SJ, b) SB&RJ, and c) RB&RJ.

4.2.4.3 *Maximum Mean Streamwise Velocity Magnitude*

The magnitude of the local maximum streamwise velocities at different measurement locations beneath the ice jam for all the three test series are plotted in Figure 4-21. Regardless of the boundary roughness, the maximum velocity increased through the UTR and the highest maximum velocity was observed near the toe of the jam, then the value of the maximum

velocity decreased as the flow developed in the downstream of the jam. For the smooth boundaries, the flow velocity had the highest magnitude near the jam toe at L9 in the UTR. When the jam was rougher than the bed, the local maximum velocity greatened respect to the corresponding values of the smooth boundaries; the enhancement was dominant in the LTR and the maximum velocity happened at L10. In the case of both rough boundaries, the local maximum velocities were higher than those of other tests. Near the rough jam toe, if the bed roughness elements were not removed from the bed, the magnitude of the maximum velocity would extremely increase compared to the other tests. Downstream of the jam at L15 the difference between the maximum velocity value for Test SB&SJ and Test SB&RJ was small. In this location, for Test RB&RJ, where the bed was rougher than the jam, the maximum velocity value was smaller than the values of the other test.

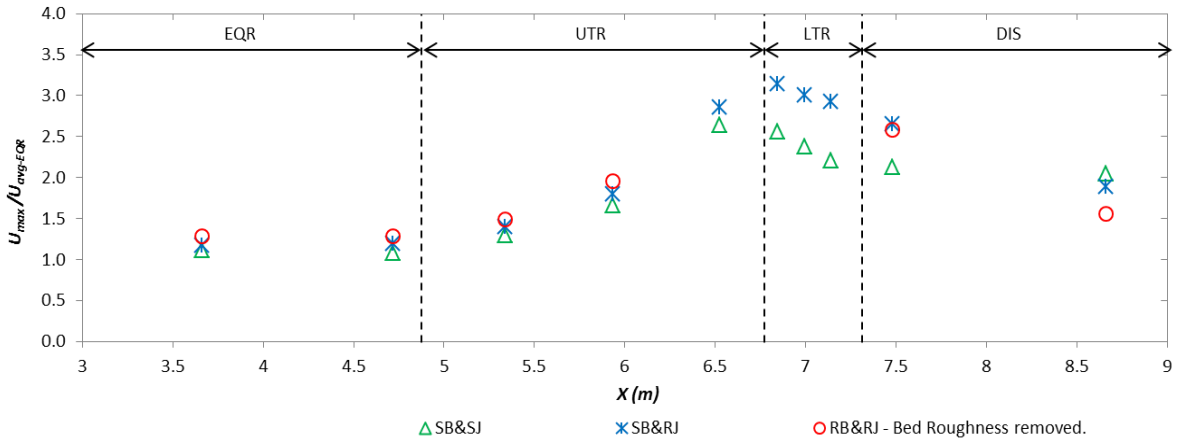

Figure 4-21: Comparison of magnitude of the maximum streamwise velocity under the ice jam with varying boundary roughness.

4.2.4.4 *Contour Plots of Streamwise Velocity*

The contours of the mean streamwise velocity beneath the ice jam for three boundary roughness ratios were plotted in Figure 4-22. The plots indicated the maximum velocity happened near the jam toe for all the three tests. When the boundaries were rough, the maximum velocity was higher compared to the smooth boundaries. The rough boundaries caused the velocity damping much adjacent to the top and bottom boundary in comparison with the smooth boundaries. When the top boundary was rougher than the bottom boundary, the maximum velocity was located near the smooth bottom boundary.

a)

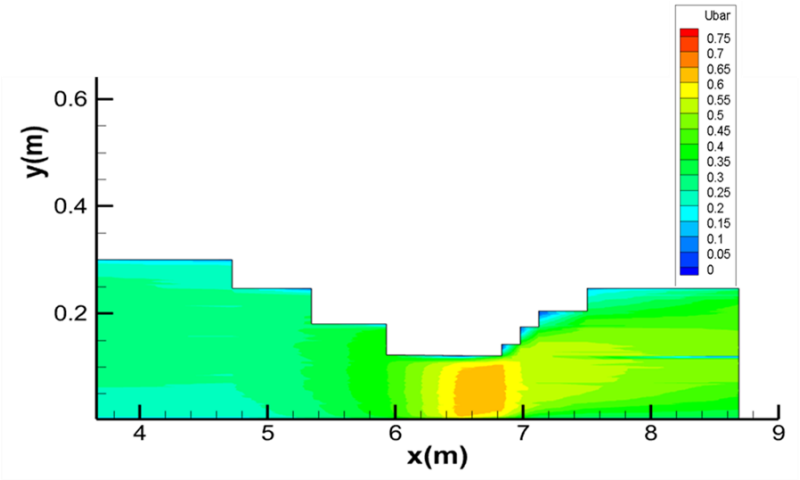

b)

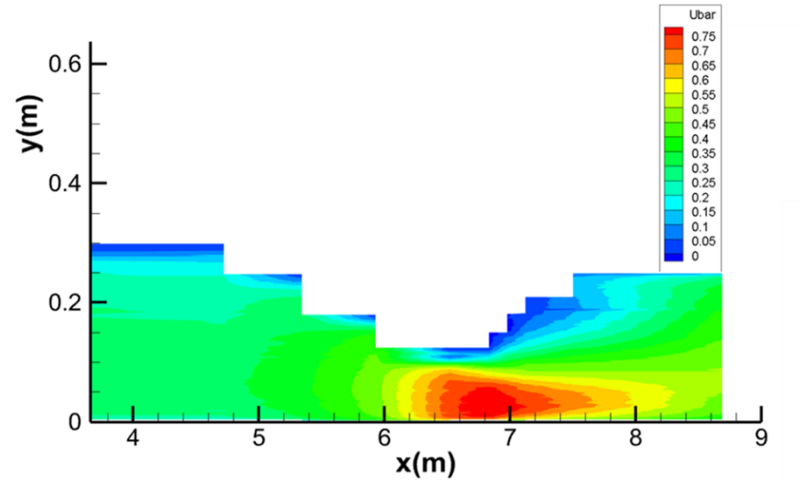

c)

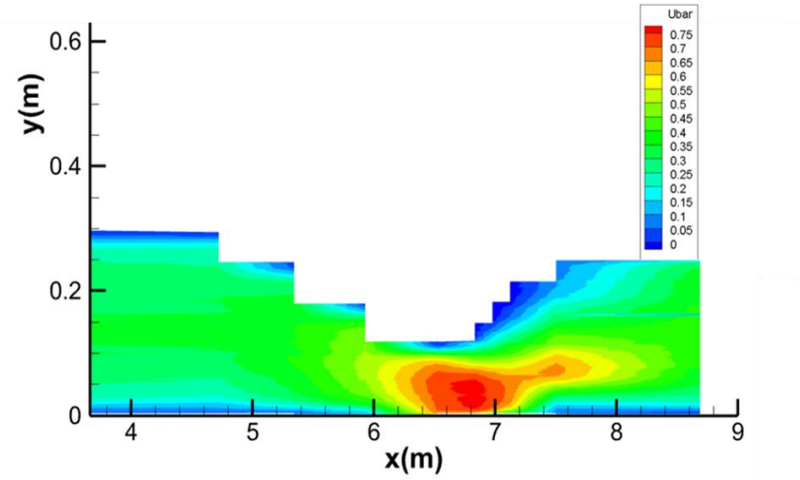

Figure 4-22: Contour plots of the streamwsie velocity for tests a) SB&SJ, b) SB&RJ, and c) RB&RJ.

4.2.4.5 ***Shear Stress Distribution***

The presence of an ice jam can influence the channel morphology and sediment transport. The bed shear stress is an essential parameter to estimate the sediment transport rate in channels. By knowing the sediment transport rate, it is possible to evaluate erosion and deposition of channel beds as well as suspended sediment rate in water. Thus, it is beneficial to know how ice jam affects the bed shear stress distribution.

Accurate estimation of the friction velocity is necessary for the determination of the bed shear stress distribution. In this study, the friction velocity was determined by fitting the measured mean velocity to the logarithmic law, using the Clauser plotting technique (Shah and Tachie, 2008). To apply the method, first, each of the measured mean streamwise velocity profiles were divided by the location of maximum velocity into two regions: the bed-affected and ice-affected region. Second, a MATLAB code was written to fit the measured velocity in the bed-affected region to the logarithmic law by changing the friction velocity until a best fit was obtained based on minimum root mean square error (RMS) of the theoretical data from the measured data. Then, the local bed shear stress for each of the measured locations was calculated using Equation 2-16 ($\tau_b = \rho u_*^2$).

For Tests SB&SJ and SB&RJ where the channel bed was smooth, the classical logarithmic law (Equation 2-5) was used to determine the friction velocity. In the case of rough bed channels, for turbulent flow in entirely rough regime, the classical logarithmic law is modified to (Gonzalez et al., 1996):

$$\frac{U}{u_*} = \frac{1}{K}\ln(\frac{30y}{k_s}) \qquad \text{Equation 4-1}$$

where, k_s is the roughness height. Therefore, for Test RB&RJ where the channel bed was rough, the friction velocity was estimated by fitting the measured data to Equation 4-1. In this case, the fitting parameters ($u_* \; and \; k_s$) were changed until a best fit was attained based on the minimum root mean square error (RMSE) of the theoretical data from the measured data.

The validity of the logarithmic law has been observed for mild and moderate adverse pressure gradient (Cutler and Johnston, 1989; Samuel and Joubert, 1974). Any increase in the adverse pressure gradient would lead to increase in the strength of the wake; as a result, the strong adverse pressure gradient causes the logarithmic region to disappear. It is also reported that the logarithmic law is applied to moderate and mild favorable pressure gradient (Fernholz and Warnack, 1998). In this case, the logarithmic law will disappear as the acceleration reaches a strong level (Blackwelder and Kovasznay, 1972). Accordingly, the pressure gradient parameter was calculated at the measured locations beneath the ice jam and the results indicated that the pressure gradient was not severe; therefore, the logarithmic law was applicable for this study. The profiles of the mean streamwsie velocity in inner coordinates are shown in Appendix B.

Variations of the local bed shear stress beneath the ice jam for different boundary roughness ratios of the bed to ice jam are plotted in Figure 4-23. As an overall trend, as the flow developed, the local bed shear stress increased until it reached a maximum magnitude near the toe of the jam, then decreased. In the case of both smooth bed and ice jam, the

maximum bed shear stress occurred near the toe of the jam at L9, as expected. When the ice jam was rougher than the bed (Test SB&RJ), the bed shear stress distribution also revealed a similar trend with maximum shear stress near the toe of the jam at L10. For the rough bed and rough jam, the shear stresses rapidly increased with a considerable difference respect to the other tests.

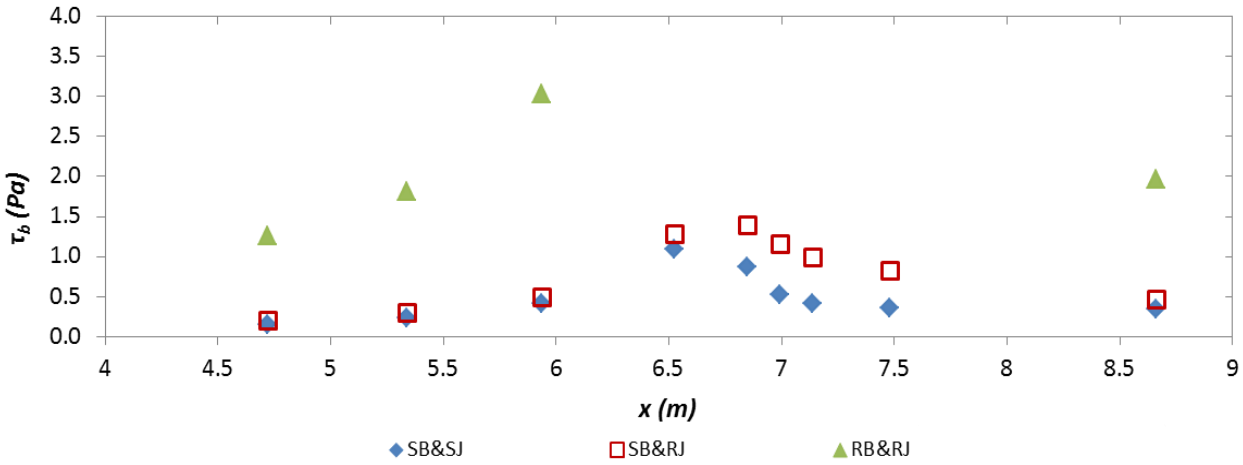

❖ The shear stress was not shown for locations where the bed roughness elements were removed.

Figure 4-23: Local bed shear stress distribution for varying the bed and ice jam roughness.

As mentioned earlier, the roughness elements were removed near the toe of the jam due to the high bed shear stresses, so, the shear stresses in this area were not shown. However, it is hypothesized that in this area the bed shear stress will have the same trend as other tests. For Test RB&RJ, when using Equation 4-1 to calculate the friction velocity for L13, an acceptable fit was not obtained; hence, the shear stress for this location was not reported.

The most sediment transport and bed erosion should be expected to occur near the toe of the ice jam, and the rough jam intensifies the potential for bed scour in that area due to the high local bed shear stresses.

Table 4-1: Summary of the local bed shear stresses beneath the ice jam.

Location	X (m)	SB&SJ τ_b (Pa)	SB&RJ τ_b (Pa)	RB&RJ τ_b (Pa)
L3	4.72	0.15	0.21	1.26
L5	5.34	0.23	0.30	1.81
L7	5.93	0.41	0.50	3.04
L9	6.52	1.09	1.29	-
L10	6.85	0.86	1.40	-
L11	6.99	0.52	1.16	-
L12	7.14	0.41	0.99	-
L13	7.48	0.36	0.83	-
L15	8.66	0.34	0.47	1.96

4.2.4.6 Turbulence Intensity

The dimensionless mean streamwise turbulence intensities are compared for the all three tests at each of the measurement locations in Figure 4-24. It can be seen in Figure 4-23 that the roughness elements have an important effect on the turbulence intensity. In the UTR, the turbulence intensity near the rough top boundary in Tests SB&RJ and RB&RJ was much higher compared to Test SB&SJ, while the turbulence intensity of Tests SB&SJ and SB&RJ followed the same distribution in the lower region (over approximately 32% of the local flow depth) due to equal bed roughness. However, in Test RB&RJ, the turbulence intensity in the lower region was higher than the turbulence intensity in the other tests, except in the toe

region where the roughness elements were detached and removed from the bed by the flow. As the flow redeveloped in the LTR, the peak value of u_{rms}/U_{max} moved farther from the upper boundary in comparison with the UTR. Lastly, as the flow redeveloped in the DIS, the turbulence intensity distributions in all three tests will tend to return to that in the EQR.

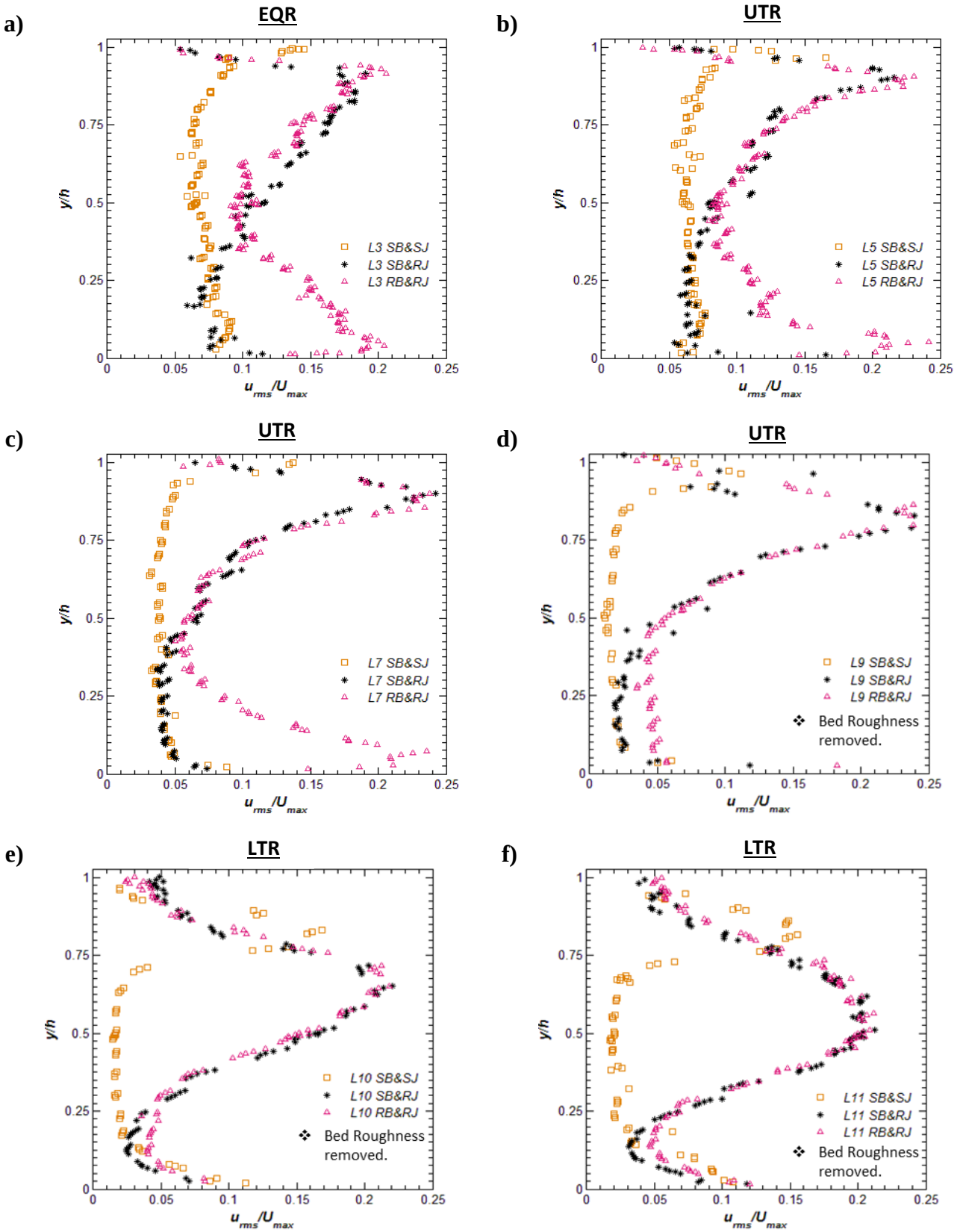
a)
EQR
y/h
u_{rms}/U_{max}
L3 SB&SJ
L3 SB&RJ
L3 RB&RJ
b)
UTR
L5 SB&SJ
L5 SB&RJ
L5 RB&RJ
c)
UTR
L7 SB&SJ
L7 SB&RJ
L7 RB&RJ
d)
UTR
L9 SB&SJ
L9 SB&RJ
L9 RB&RJ
Bed Roughness removed.
e)
LTR
L10 SB&SJ
L10 SB&RJ
L10 RB&RJ
Bed Roughness removed.
f)
LTR
L11 SB&SJ
L11 SB&RJ
L11 RB&RJ
Bed Roughness removed.

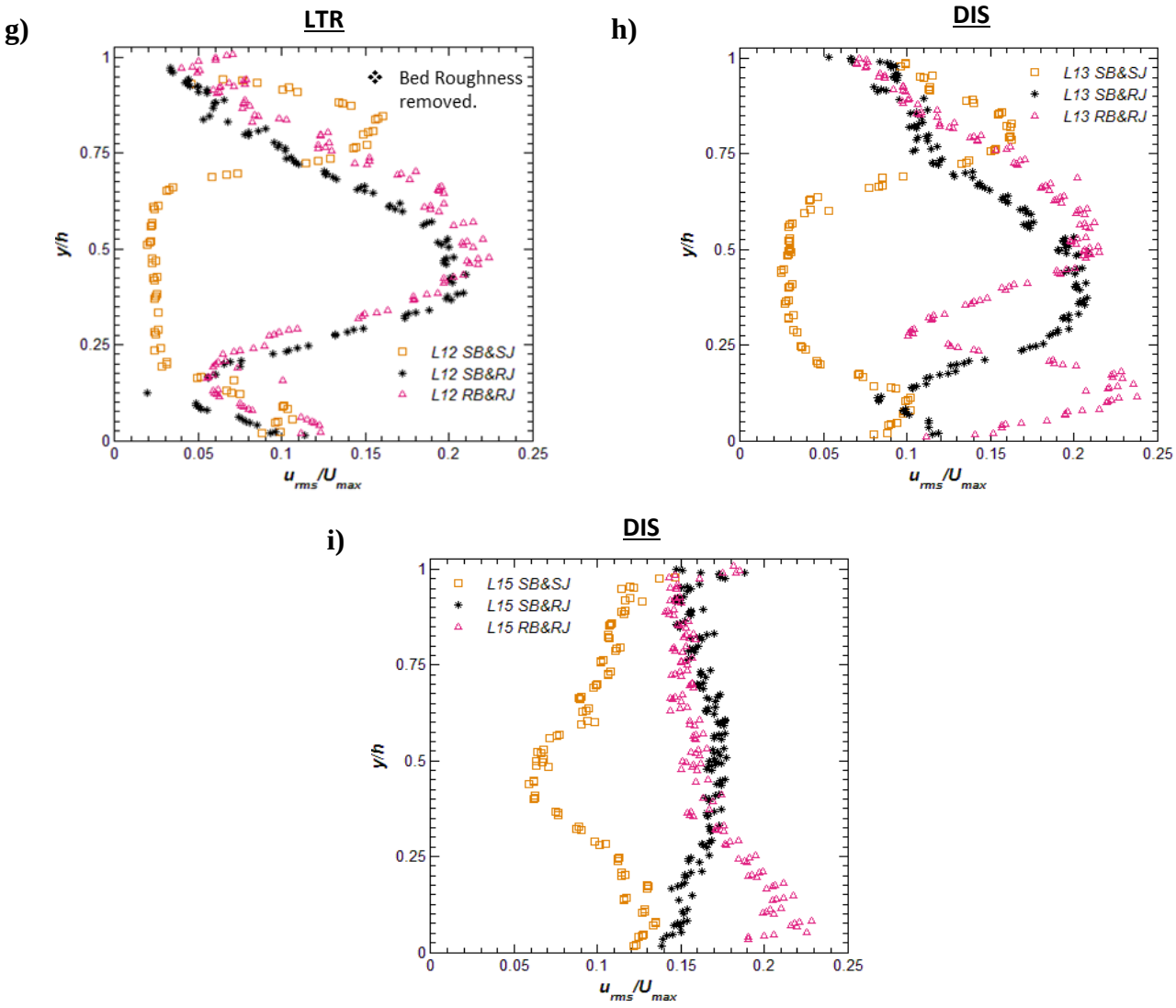

Figure 4-24: Comparison of dimensionless streamwise turbulence intensity for varying bed and ice jam roughness in the EQR (a), UTR (b), (c) and (d), LTR(e), (f) and (g), DIS (h) and (i).

Chapter 5:

CONCLUSIONS AND RECOMMENDATIONS

Ice jams have the potential to alter river hydraulics such as changes to the flow conveyance characteristics. Comprehensive understanding of ice jam effects on the hydraulics of rivers can assist to protect or minimize losses due to ice jams by informing planning and management strategies of ice-covered rivers. The purpose of this research was to investigate the effects of an ice jam on the flow velocity and turbulence intensity in a channel. Experiments were conducted in a fixed-bed, sloped flume in the Hydraulics Research & Testing Facility at the University of Manitoba. The research was conducted in two scenarios:

(1) an ice jam with the same height of the equilibrium region and downstream of the jam; (2) an ice jam with a height difference between the equilibrium region and downstream of the jam. To assess the impact of boundary roughness on the hydraulic characteristics of channels, different roughness ratios of the bed to ice jam were defined for the second scenario. Velocity measurements were taken at various points along the water column, at different locations in the centerline of the channel with an ADV instrument. Through these measurements, the flow velocity profiles, turbulence intensity distributions, and bed shear stress variations were analyzed. The first scenario was a basis to identify and construct a framework to study the flow characteristics underneath an ice jam. Because the second scenario provided a better simulation of an ice jam in nature, conclusions are made upon the second scenario.

5.1 Conclusions

A list of research accomplishments and major findings of the research are summarized as follows:

1. The streamwise velocity profiles for different roughness ratios of the ice jam to bed were compared to each other for the same locations along the ice jam. The flow velocity was significantly affected by the rough boundaries; the velocity much decreased adjacent to either the rough ice jam or the rough channel bed compared to the smooth boundaries. In the lower toe region part of the jam (LTR), negative velocities near the undersurface of the rough jam were evidence of the existence of a recirculation zone in this region.

2. Examination of the local maximum velocity beneath the ice jam demonstrated the maximum velocity was greatest near the jam toe. The rough ice jam caused the magnitude of the local maximum velocity to increase even more than the smooth jam near the jam toe.

3. The boundary roughness influenced the turbulence intensity distribution. The presence of the rough jam significantly enhanced the turbulence intensity near the undersurface of the jam. Near the rough bed, the turbulence intensity was much higher than the smooth bed, which may increase the capacity to transport suspended sediment.

4. Distribution of the bed shear stress at various locations beneath the ice jam indicated that the maximum bed shear stress was near the jam toe where the flow velocity was high. The minimum shear stress was in the equilibrium region where the flow velocity was low. For the rough ice jam and smooth bed, the bed shear stress followed this trend but, the rough jam increased the bed shear stress near the toe of the jam. When the ice jam and bed were rough, the bed shear stress noticeably raised in the equilibrium region, the upstream toe region, and downstream of the jam. It would be expected that the shear stress would exhibit the same trend as the other experiments near the jam toe but with even higher magnitudes. Consequently, the potential of sediment transport and bed erosion would be extreme near the jam toe compared to other parts of the jam due to the high shear stress and the rough boundaries intensified this effect.

5.2 Recommendations

Although this research studied the experimental investigation on the turbulent flow characteristics beneath the ice jam for the first time, there are still many opportunities to improve this study. A list of possible future research is presented as follows:

1. As a real ice jam creates from the accumulation of large amounts of irregular ice pieces, it is suggested to make a physical model of an ice jam using discrete ice pieces with various shapes and sizes. Ideally, it will be better to utilize real ice pieces, providing a laboratory has a cold temperature facility; otherwise, use artificial ice pieces.

2. Measure the effect of different parameters such as trapezoidal shape of the channel cross-section, and variation of the channel slope, on the flow characteristics beneath the ice jam.

3. Quantify the effect of moveable channel bed such as sand on the turbulent flow characteristics.

4. Investigate the roughness effect of channel side walls for various channel aspect ratios on the turbulent flow characteristics.

5. To increase the measurement accuracy of turbulent flow features near the undersurface of the ice jam, it is recommended that data be collected without using any holes at measurement locations.

6. Verify the turbulent flow features over an entire cross-section at different locations along the ice jam. For this purpose, it is recommended to use volumetric velocimetry

such as 3D particle image velocimetry (3D PIV) for flow velocity measurements since the instrument can measure three components of flow velocity in a volume of fluid.

7. Further research is required to estimate wall shear stresses for example determination of the wall shear stresses through direct measurements with a Preston tube.

8. Examine effect of the upstream transition part of an ice jam, as discussed in Chapter 2 (Figure 2-1), on the turbulent flow features.

9. The results of this study can be used to validate numerical models related to river ice studies.

REFERENCES

Ashton, G.D. River Lake Ice Engineering. Colorado, USA: Water Resources Publications, LLC, 1986.

Balachandar, R., K. Hagel, and D. Blakely. "Velocity distribution in decelerating flow over rough surfaces." *Journal of Civil Engineering*, 2002: 211–221.

Beltaos, S. "Numerical computation of river ice jams." *Canadian Journal of Civil Engineering 20*, no. 1 (1993): 88-99.

Beltaos, S. River Ice Breakup. Highlands Ranch, Colorado, USA: Water Resources Publications, LLC, 2008.

Beltaos, S. River Ice Jams. Highlands Ranch, Colorado, USA: Water Resources Publications, 1995.

Beltaos, S., and B.C. Burrell. "Extreme ice jam floods along the Saint John River, New Brunswick, Canada." *IAHS PUBLICATION* (2002): 9-14.

Beltaos, S., and W. J. Moody. "Measurements of the configuration of a breakup jam." Hydraulics Division, National Water Research Institute, Canada Centre for Inland Waters, 1986.

Beltaos, S., B. Burrell, and S. Ismail. "1991 ice jamming along the Saint John River: a case study." *Canadian Journal of Civil Engineering* 23, no. 2 (1996): 381-394.

Blackwelder, R. F., and L. S. G. Kovasznay. "Large-scale motion of a turbulent boundary layer during Relaminarization." *Journal of Fluid Mechanics* 53, no. 1 (1972): 61-83.

Calkins, D.J., D. Deck, and C. Martinson. "Analysis of Velocity Profiles under Ice In Sahllow Streams." *In Proceedings of workshop on Hydrauliic Resistance of River Ice. Burlington, Ontarrio: National Water Research Institute*, 1980.

Carson, R., S. Beltaos, J. Groeneveld, D. Healy, Y. She, J. Malenchak, M. Morris, J. Saucet, T. Kolerski, and H. T. Shen. "Comparative testing of numerical models of river ice jams." *Canadian Journal of Civil Engineering* 38, no. 6 (2011): 669-678.

Cheng, N.S. "Power-law index for velocity profiles in open channel flows." *Advances in Water Resources* 30, no. 8 (2007): 1775–1784.

Chow, V.T. Open-Channel Hydraulics. New York, USA: McGraw-Hill Book Company, 1959.

Coles, D. "The law of the wake in the turbulent boundary layer." *Journal of Fluid Mechanics* 1, no. 2 (1956): 191-226.

Cutler, A. D., and J. P. Johnston. "The relaxation of a turbulent boundary layer in an adverse pressure gradient." *Journal of Fluid Mechanics* 200 (1989): 367-387.

Dolgopolova, E. N. "Investigation of turbulent underice flows." In Proceedings of IAHR Ice Symposium. Trondheim, Norway, 1994: 79-83.

Dolgopolova, E. N. "Velocity distribution in ice-covered flow." In *Ice in Surface Waters*, Rotterdam: Balkerma, 1998: 123-129 .

Durand, Z. "Experimental Study of Tailwater Level and Asymmetry Ratio Effects on Three-Dimensional Offset Jets." University of Manitoba, 2014.

Ettema, R., and S. F. Daly. Sediment transport under ice. No. ERDC/CRREL TR-04-20. Engineer Research and Development Center Hanover NH Cold Regions Research and Engineering Lab, 2004.

French, R.H. Open-Channel Hydraulics. New York, USA: McGraw-Hill Publishing Company, 1985.

Fernholz, H. H., and D. Warnack. "The effects of a favorable pressure gradient and of the Reynolds number on an incompressible asymmetric turbulent boundary layer. Part 1. The turbulent boundary layer." *Journal of Fluid Mechanics* 359 (1998): 329-356.

Gerard, R. "Flow in ice covered channels: Some fundamentals." *In Proceedings of Workshop on Hydraulic Resistance of River Ice: Canada Centre for Inland Waters, Burlington, Ontario*, 1980.

Ghosh, S. N., and N. Roy. "Boundary shear distribution in open channel flow." *J. Hydraul. Div.*, ASCE 96, no. 4 (1970): 967-994.

Gogus, M., and J. C Tatinclaux. "Mean characteristics of asymmetric flows: Application to flow below ice jams." *Canadian Journal of Civil Engineering* 8, no. 3 (1981): 342-350.

Gonzalez, J. A., S. M. Charles, and K. A. Oberg. "Analysis of open-channel velocity measurements collected with an acoustic Doppler current profiler." In *Proc., RiverTech96,* vol. 2, 1996: 838-845.

Goring, D. G., and V. I. Nikora. "Despiking Acoustic Doppler Velocimeter Data." *Journal of Hydraulic Engineering* 128, no. 1 (2002): 117–126.

Hanjalic, K., and B. E. Launder. "Fully developed asymmetric flows in a plane channel." *Journal of Fluid Mechanics* 51, no 2 (1972): 301-335.

Healy, D., and F. E. Hicks. "Experimental study of ice jam formation dynamics." *Journal of Cold Regions Engineering* 20, no. 4 (2006): 117-139.

Healy, D., F. Hicks, and M. Loewen. "Unsteady velocity profiles under a floating cover." In *Ice in the Environment: Proceedings of the 16th IAHR International Symposium on Ice,* Dunedin, New Zealand, 2002: 2-6.

Henderson, F.M. Open Channel Flow. New Yor, USA: Macmillan Publishing Company, Inc., 1966.

Hicks, F.E., and C. Bonneville. "Modelling ice jam evolution processes." Ice in Surface Waters, Balkema, Rotterdam, 1998: 93-99.

Kawai, T., F. Hara, S. Masaki, A. Nishihata, and H. Saeki. "Experimental study on the process of ice jam development." In *Proc. 9th Workshop on River Ice,* CGU-HS CRIPE, 1997: 245-256.

Keulegan, G.H. "Laws of Turbulent Flow in Open Channels." *Journal of Research of the National Bureau of Standards,* 1938: 707-741.

Khodashenas, S.R., K. E. K. Abderrezzak, and A. Paquier. "Boundary shear stress in open channel flow: A comparison among six methods." *Journal of Hydraulic Research* 46, no. 5 (2008): 598–609.

Kirkgoz, M.S. "Turbulent velocity profiles for smooth and rough open channel flows." *Journal of Hydraulic Engineering* 115, no. 11 (1989): 1543-1561.

Kiya, M., and K. Sasaki. "Structure of a turbulent separation bubble." *Journal of fluid Mechanics* 137 (1983): 83-113.

Knight, D. W., J. D. Demetriou, and M. E. Hamed. "Boundary shear in smooth rectangular channels." *Journal of Hydraulic Engineering* 110, no. 4 (1984): 405–422.

Kolerski, T., F. Huang, and H. T. Shen. "Development of ice jam toe configurations." In *Proceedings of the 23rd IAHR International Symposium on Ice*, Michigan, USA, 2016.

Kowalczyk, T., and F. Hicks. "Observations of dynamic ice jam release on the Athabasca River at Fort McMurray, AB." *In Proc. 12th Workshop on River Ice, Edmonton,* 2003.

Lau, Y.L. "Velocity distributions under floating covers." *Canadian Journal of Civil Engineering* 9, no. 1 (1982): 76-83.

Leonardi, S., P. Orlandi, R. J. Smalley, L. Djenidi, and R. A. Antonia. "Direct numerical simulations of turbulent channel flow with transverse square bars on one wall." *Journal of Fluid Mechanics* 491(2003): 229–238.

Leutheusser, H.J. "Turbulent flow in rectangular ducts." *J. Hydraul. Div., Am. Soc. Civ Eng.,HY* (1963): 1-19.

Mercer, A. G., and R. H. Cooper. "River bed scour related to the growth of a major ice jam." In *Proceedings of the 3rd Canadian Hydrotechnical Conference*, Que, 1977: 30-31.

Nezu, I., H. Nakagawa. Turbulence in Open-Channel Flows. Rotterdam, Netherlands: A.A. Balkema, 1993.

Nortek. "Comprehensive manual for acoustic Doppler velocimeter.", 2013.

Pariset, E., and R. Hauser. "Formation and evolution of ice covers on rivers." (1961): 41-49.

Parthasarathy, R. N., and M. Muste. "Velocity measurements in asymmetric turbulent channel flows." *Journal of Hydraulic Engineering* 120, no. 9 (1994): 1000-1020.

Peters, M. "An Experimental Study of the Hydraulic Characteristics beneath a Partial Ice Cover." University of Manitoba, 2015.

Pritchard, P. J. *Fluid Mechanics.* USA: John Wiley and Sons, Inc, 2011.

Prowse, Terry D. "Ice jam characteristics, Liard-Mackenzie rivers confluence." *Canadian Journal of Civil Engineering* 13, no. 6 (1986): 653-665.

Robert, A., and T. Tran. "Mean and turbulent flow fields in a simulated ice-covered channel with a gravel bed: some laboratory observations." *Earth surface Processes and Landforms* 37, no. 9 (2012): 951–956.

Shah, M. K., and M. F. Tachie. "PIV study of turbulent flow in asymmetric converging and diverging channels." *Journal of Fluids Engineering* 130, no. 1 (2008): 011204.

Samuel, A.E. and P. N. Joubert. "A Boundary Layer Developing in an Increasingly Adverse Pressure Gradient." *Journal of Fluids Engineering* 66, no. 03 (1974): 481-505.

She, Y., R. Andrishak, F. Hicks, B. Morse, E. Stander, C. Krath, D. Keller et al. "Athabasca River ice jam formation and release events in 2006 and 2007." *Cold regions science and technology* 55, no. 2 (2009): 249-261.

Shen, H. T. "Development of a comprehensive river ice simulation system." *In Proceedings of the 16th. IAHR International Symposium on Ice, Dunedin. New Zealand*, vol. 1, pp. 142-148. 2002.

Sturm, T.W. Open Channel Hydraulics. New York, USA: McGraw-Hill Companies, Inc, 2001.

Sui, J., J. Wang, Y. He, and F. Krol. "Velocity profiles and incipient motion of frazil particles under ice cover." *International Journal of Sediment Research* 25, no. 1 (2010): 39-51.

Sukhodolov, A., M. Thiele, H. Bungartz, and C. Engelhardt. "Turbulence structure in an ice-covered, sand-bed river." *Water Resources Research* 35, no. 3 (1999): 889–894.

Tatinclaux, J.C., and C. L. Lee. "Initiation of ice jams- a laboratory study." *Canadian Journal of Civil Engineering* 5, no. 2 (1978): 202-212.

Tatinclaux, J.C., and M. Gogus. "Asymmetric Plane flow with Application to ice jams." *Journal of Hydraulic Engineering* 109, no. 11 (1983): 1540-1554.

Teal, M. J., R. Ettema, and J. F. Walker. "Estimation of mean flow velocity in ice-covered channels." *Journal of Hydraulic Engineering* 120, no. 12 (1994): 1385-1400.

Tsai, W., and R. Ettema. "Modified Eddy Viscosity Model in Fully Developed Asymmetric Channel Flows." *Journal of Engineering Mechanics* 120, no. 4 (1994): 720-732.

Tsai, W.F., and R. A. Ettema. "Study of ice-covered flow in an alluvial bend." IIHR Technical Report No. 376, Iowa Institute of Hydraulic Research, 1996.

Uzuner, M. "The composite roughness of ice covered streams." *Journal of Hydraulic Research* 13, no. 1 (1975): 79-102.

Urroz, G.E., and R. Ettema. "Application of two-layer hypothesis to fully developed flow in ice-covered curved." *Canadian Journal of Civil Engineering* 21, no. 1 (1994): 101-110.

Urroz, G.E., R. Ettema. "Small-scale experiments on ice-jam initiation in a curved channel." *Canadian Journal of Civil Engineering* 21, no. 5 (1994): 719-727.

Walker, J. F. "Methods for measuring discharge under ice cover." *Journal of Hydraulic Engineering* 120, no. 11 (1994): 1327-1336.

Wuebben, J. L. "A preliminary study of scour under an ice jam." *In Proceedings, 5th Workshop on Hydraulics of River Ice/Ice Jams*, 1988: 177-190.

Yamaguchi, H., and K. Hirayama. "Measurements of flow velocity under the ice cover." *IAHR Ice Symposium*. Espoo, 1990: 1155-1170.

Yang, S. Q., and S. Y. Lim. "Boundary shear stress distributions in trapezoidal channels." *Journal of Hydraulic Research* 43 (2005): 98-102.

Zufelt, E., and R. Ettema. Unsteady Ice Jam Processes. CRREL Report 97-7, U.S. Army Cold Regions Research and Engineering Laboratory, 1997.

Zufelt, J. E., and R. Ettema. Model Ice Properties. No. CRREL-96-1. Cold Regions Research and Engineering Laboratory Hanover NH, 1996.

Zufelt, J., and Z. Sun. "A laboratory study of transverse velocities and ice jamming in a river bend." In *Proceedings of the IAHR Symposium on Ice problems, Sapporo, Japan*, 1988: 23-27.

APPENDIX A: Symmetry Tests

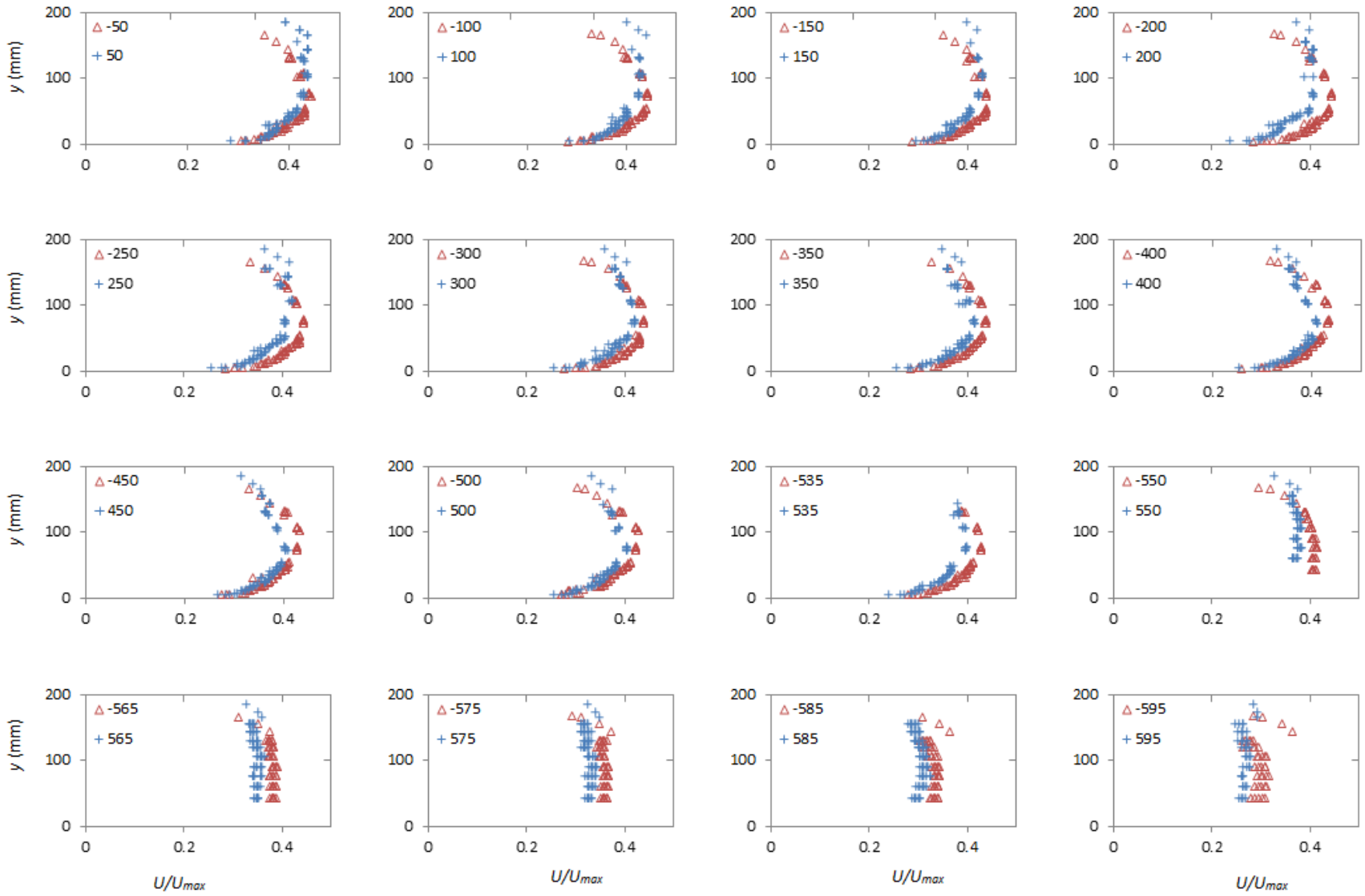

Figure A-1: Symmetry test for full ice covered channel: Streamwise Velocity.

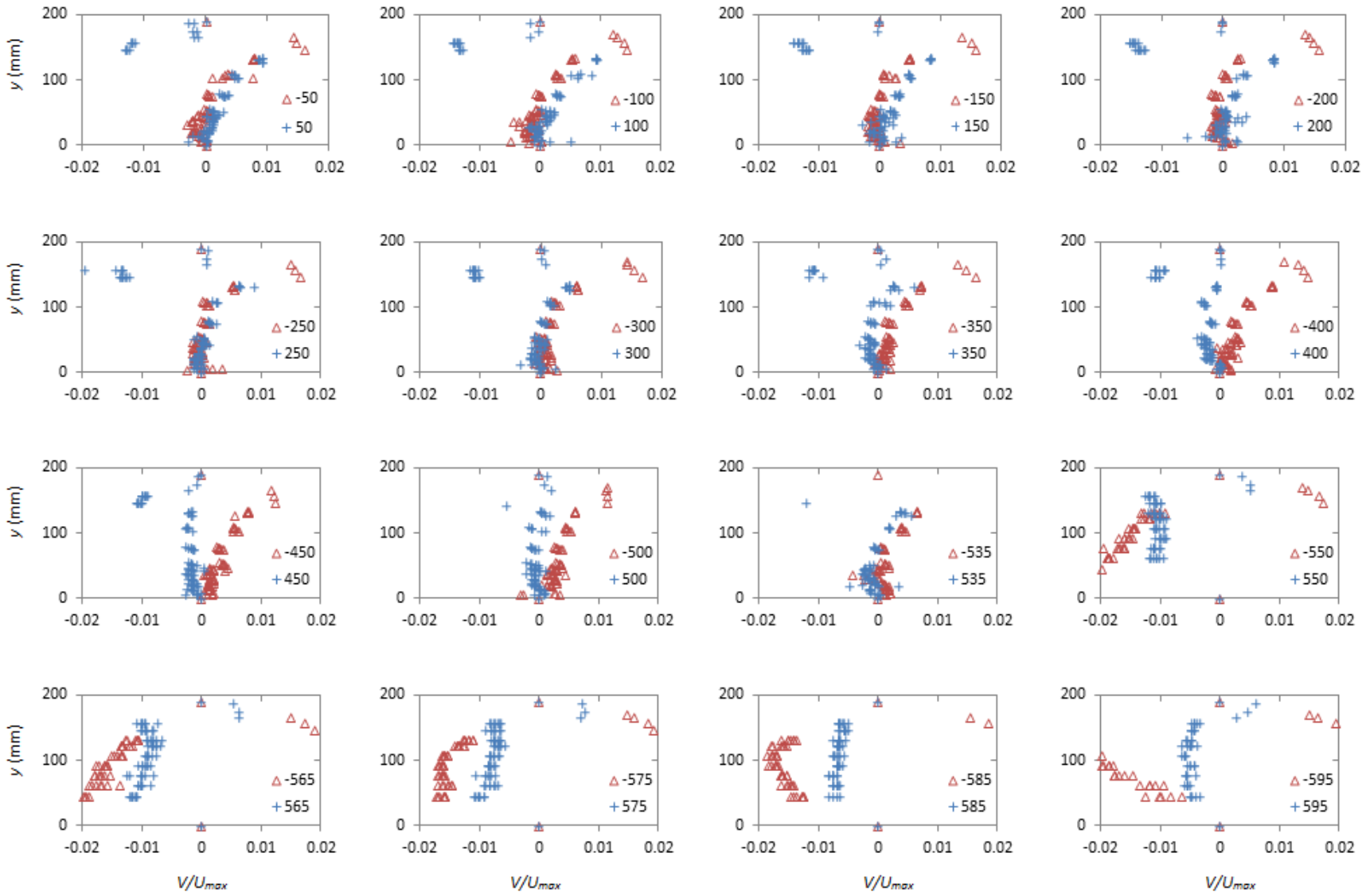

Figure A-2: Symmetry test for full ice covered channel: Vertical Velocity.

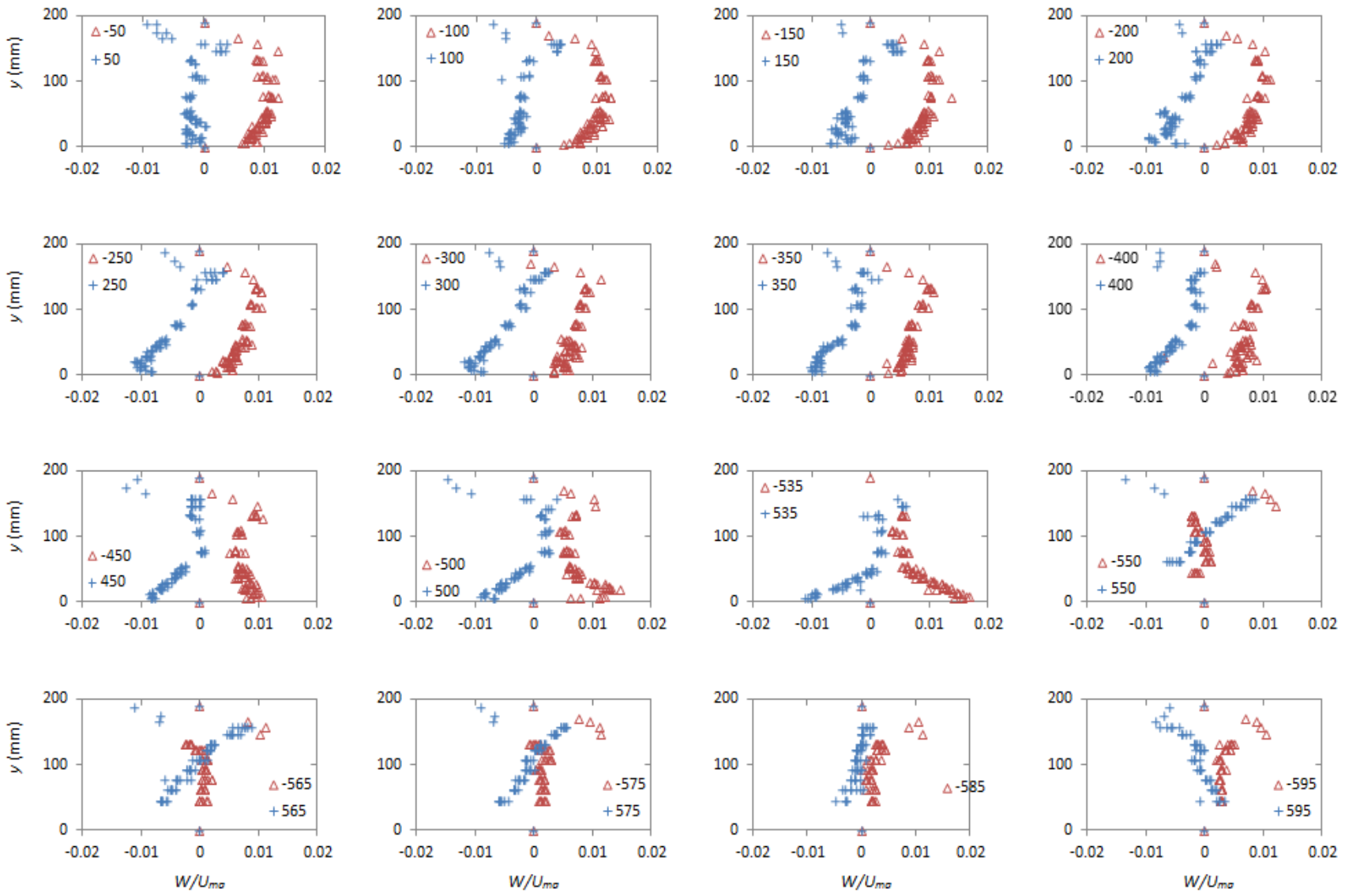

Figure A-3: Symmetry test for full ice covered channel: Spanwise Velocity.

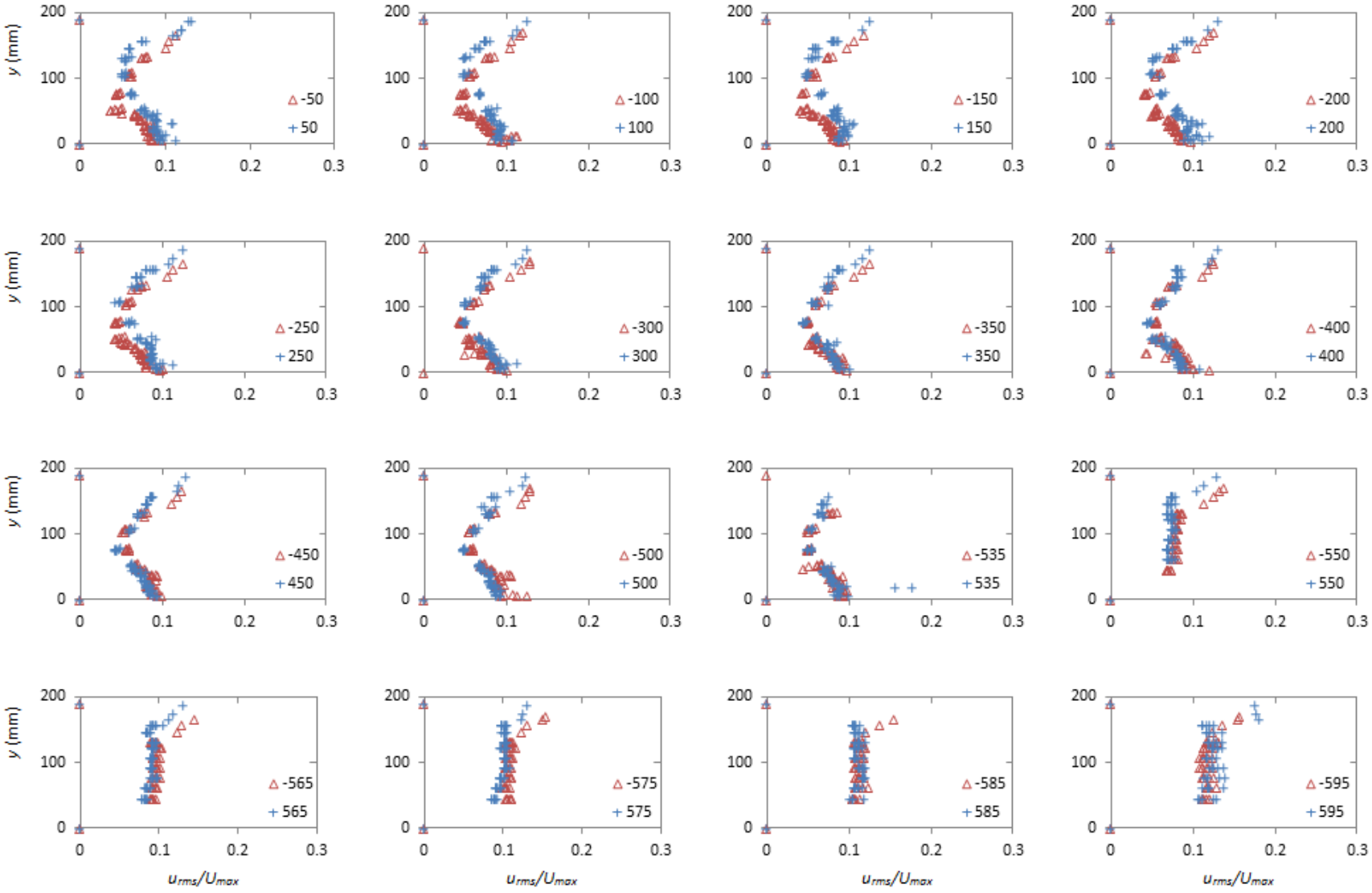

Figure A-4: Symmetry test for full ice covered channel: Streamwise Turbulence Intensity.

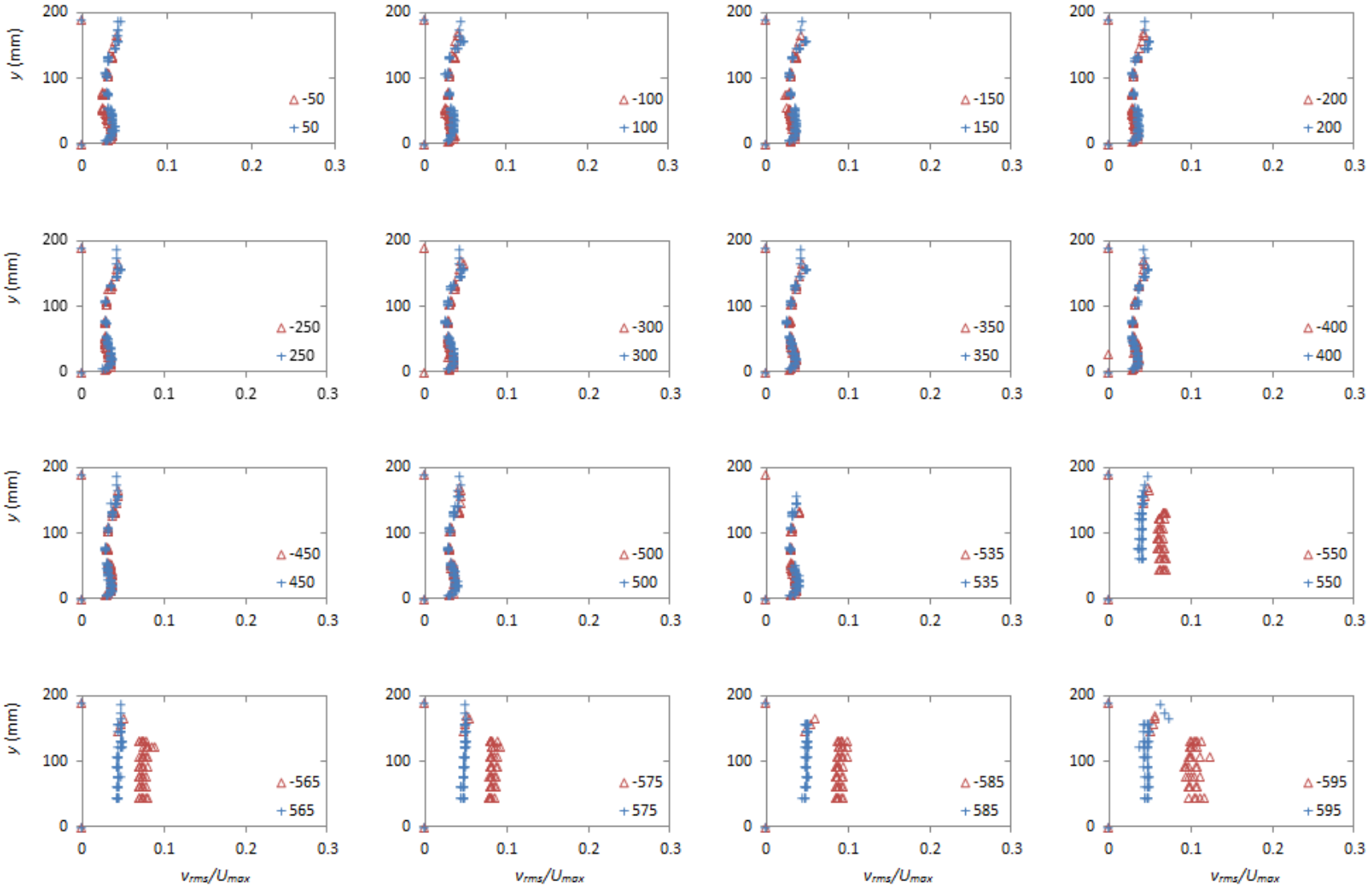

Figure A-5: Symmetry test for full ice covered channel: Vertical Turbulence Intensity.

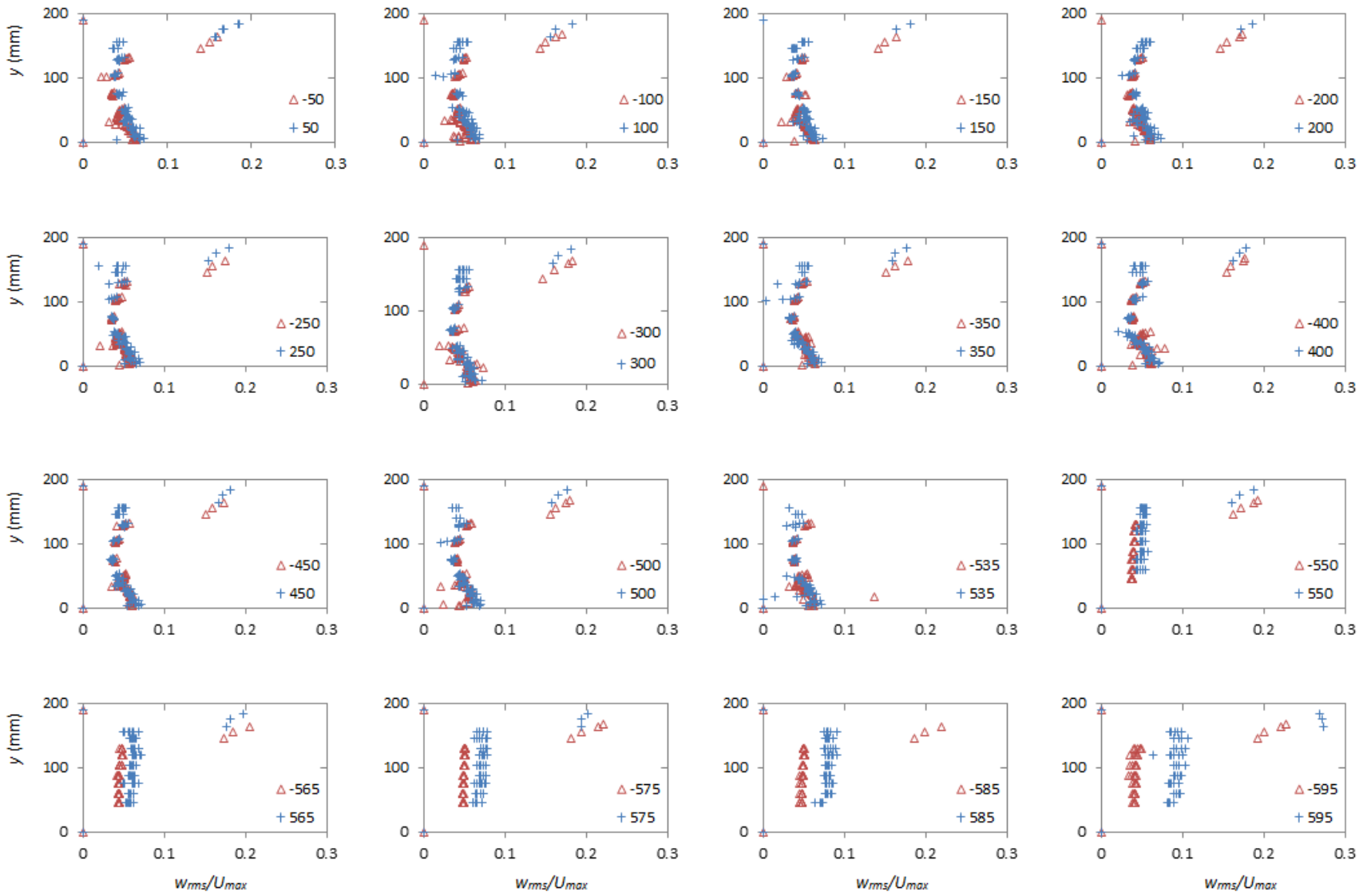

Figure A-6: Symmetry test for full ice covered channel: Spanwise Turbulence Intensity.

APPENDIX B: Velocity Profiles in Inner Coordinates

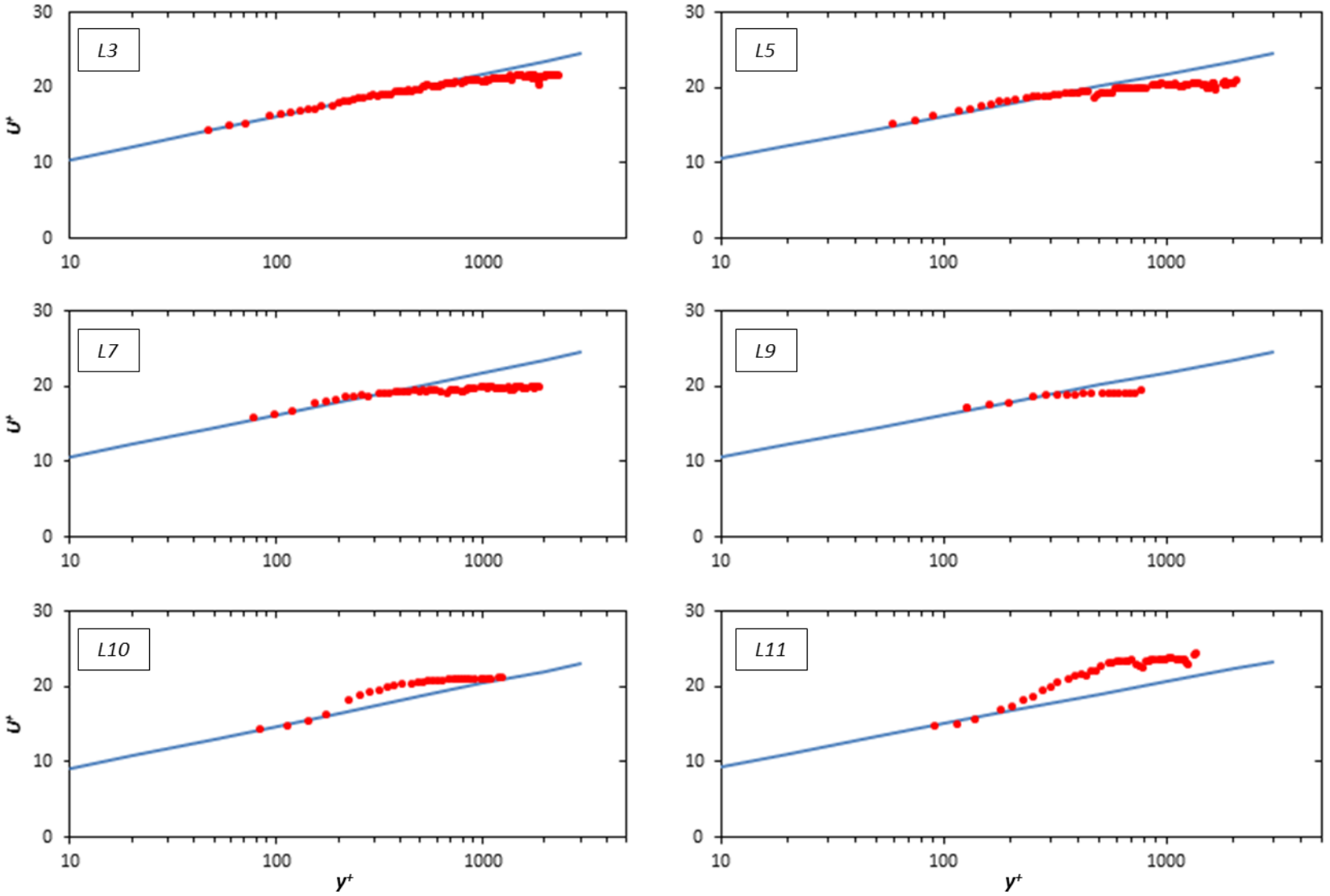
L3
L5
L7
L9
L10
L11
U+
y+
0
10
20
30
10
100
1000

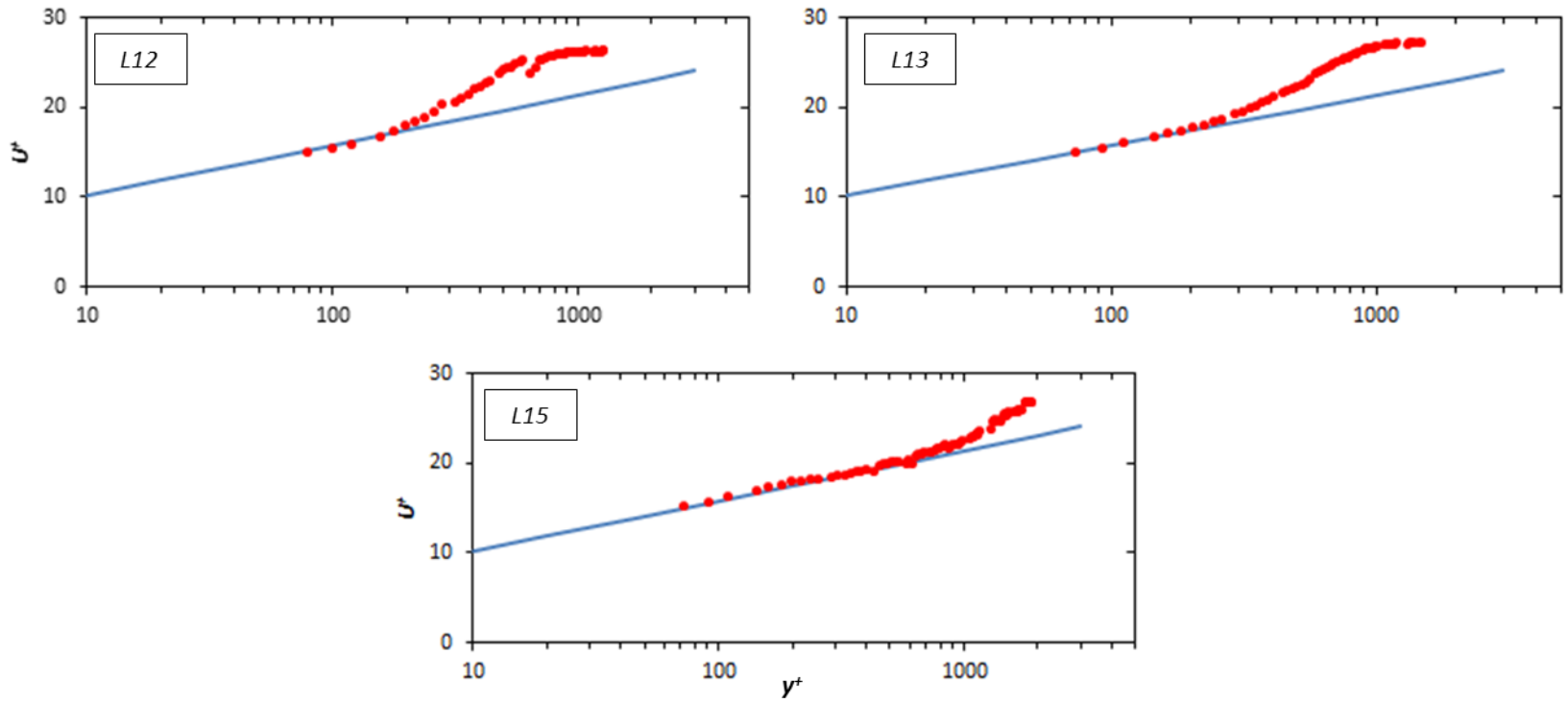

Figure B-1: Mean streamwise velocity profiles in inner coordinates for Test SB&SJ.

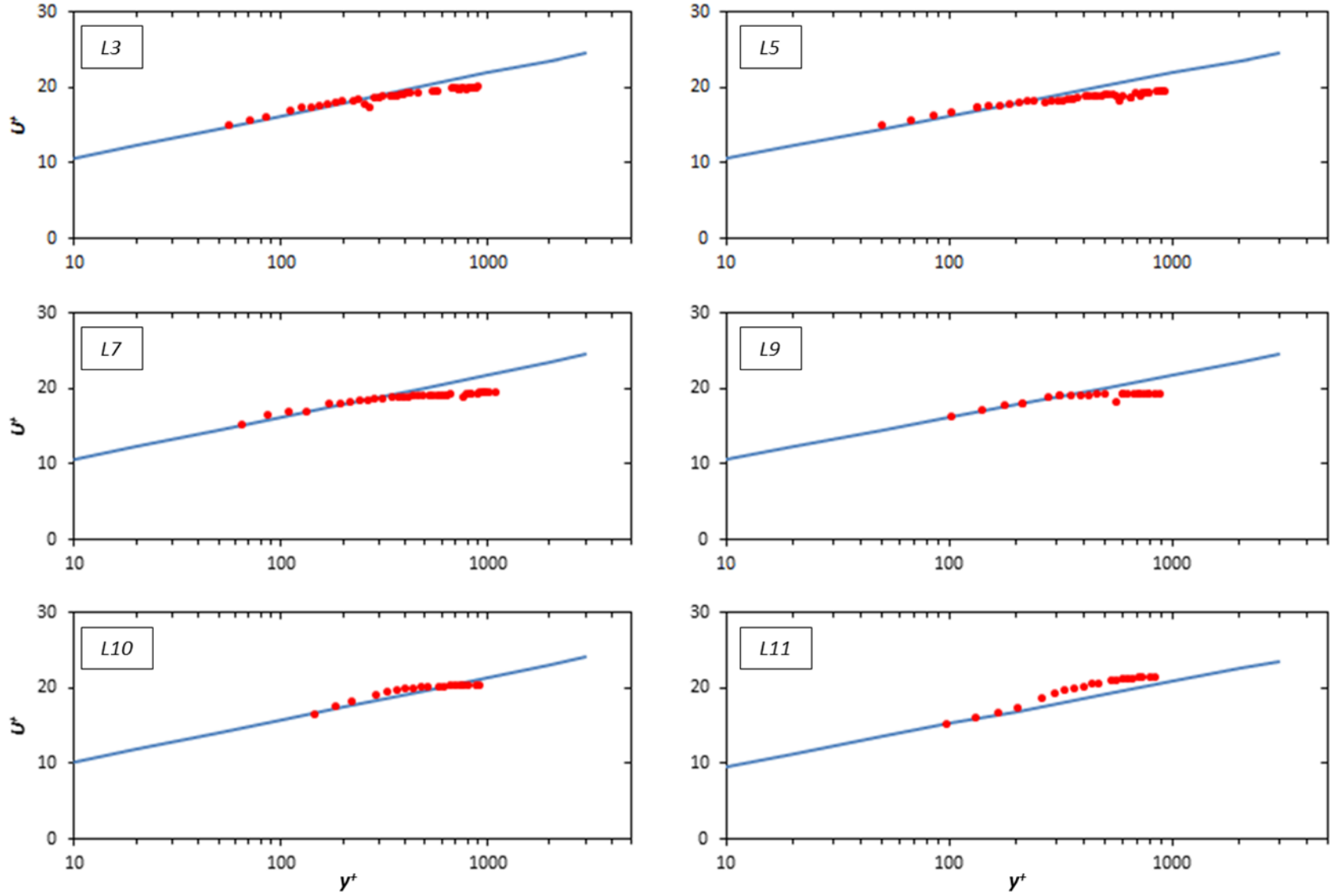
L3
L5
L7
L9
L10
L11
U⁺
y⁺
0
10
20
30
10
100
1000

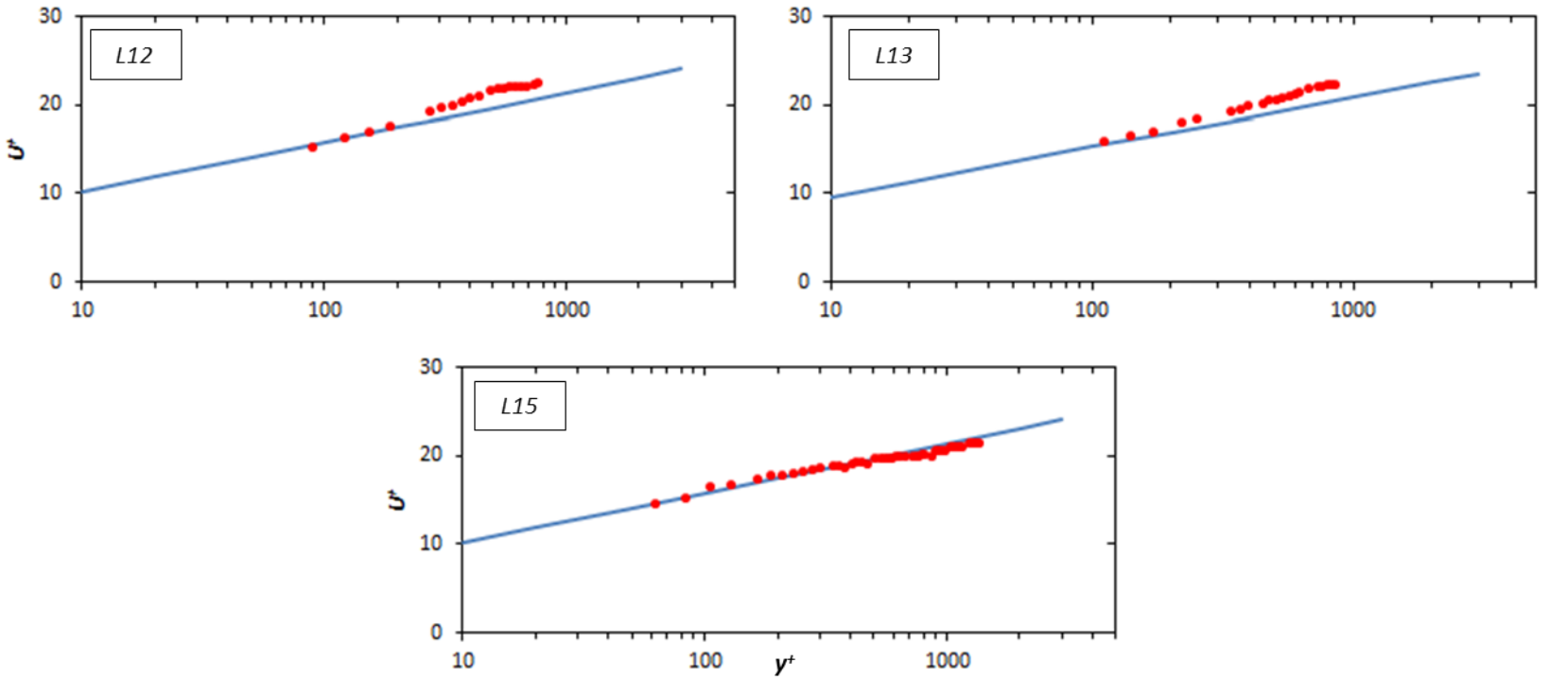

Figure B- 2: Mean streamwise velocity profiles in inner coordinates for Test SB&RJ.

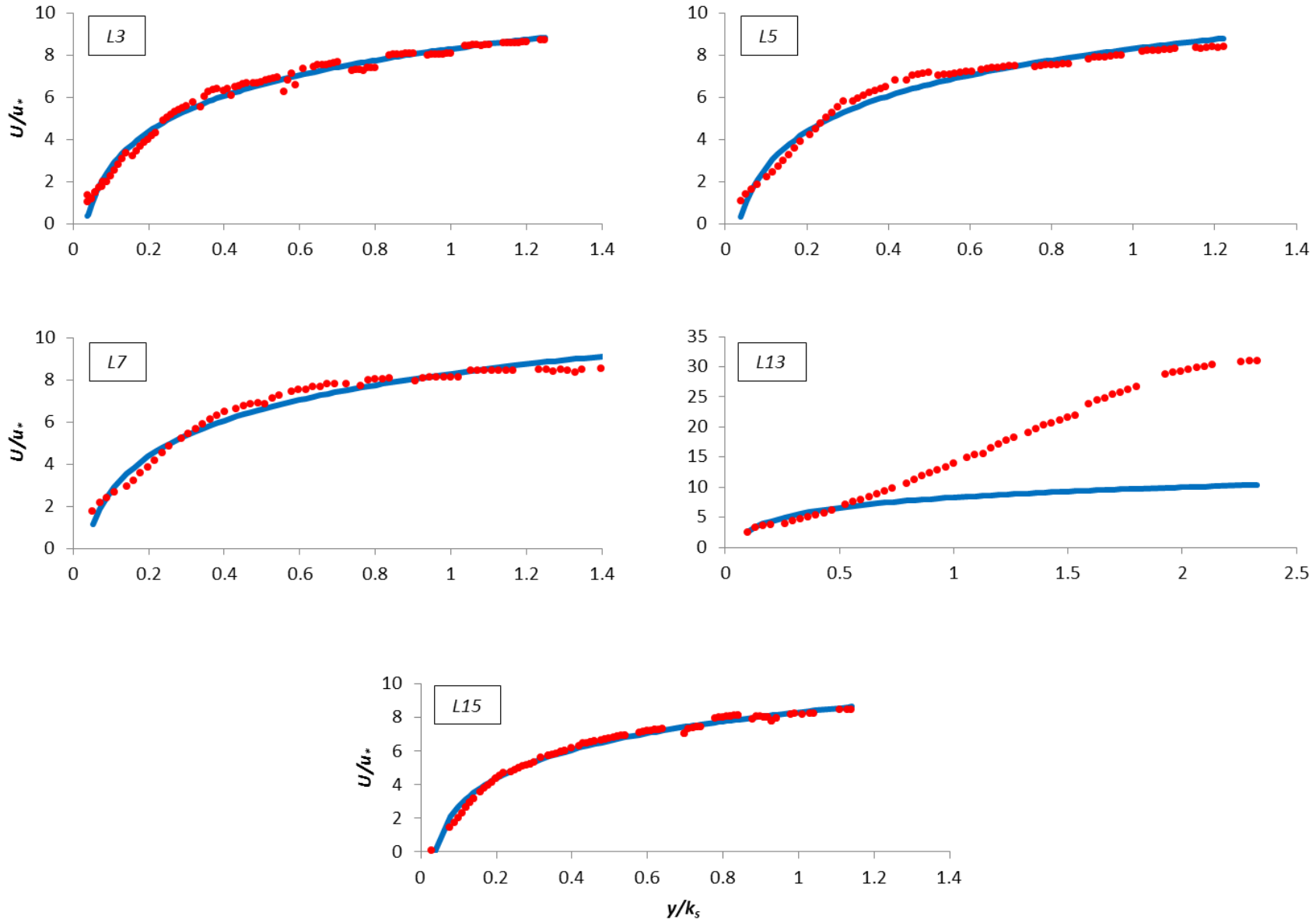

Figure B-3: Mean streamwise velocity profiles in inner coordinates for Test RB&RJ.